Energy and Position Reconstruction in Pixelated CdZnTe Detectors

by

William R. Kaye

A dissertation submitted in partial fulfillment
of the requirements for the degree of
Doctor of Philosophy
(Nuclear Engineering and Radiological Sciences)
in The University of Michigan
2012

Doctoral Committee:

Professor Zhong He, Chair
Professor Timothy E. Chupp
Professor David K. Wehe
Assistant Professor Michael R. Hartman

A day in the life...

For all the people who have taken time to educate me

ACKNOWLEDGEMENTS

First and foremost, I would like to thank my advisor, Prof. Zhong He, for introducing me to the exciting topic of radiation imaging detectors. He has challenged my ideas and techniques in a constructive way for the last five years. Without him, none of this work would be possible. I cannot imagine a better match, with respect to personality and research goals, to my learning style. I would also like to thank the members of my dissertation committee; they have taken the time to understand and critically evaluate my work while questioning my ideas and methods in order to get the best possible work out of me.

Next I have to thank the students, staff, and faculty working on this research with me. Working with Dr. Feng Zhang has been a great opportunity and honor. Early on, as I was learning the ropes, he patiently and, at times, repeatedly explained the core concepts I needed to understand our system in a clear and concise way. Later on in my time at Michigan he was always willing to vet my ideas, providing constructive criticism and steering my research down the correct path when I felt lost. The students ahead of me, especially Yuefeng Zhu and Weiyi Wang were also instrumental in bringing me up to speed on the different aspects of our project and providing feedback on my ideas. The students behind me, especially Andy Boucher, Hao Yang, and Jason Jaworski brought a fresh energy and motivation to the project that definitely pushed me to contribute at a higher level. Chris Wahl, who arrived at Michigan the same year, provided a unique and valuable brand of criticism and was a role model to me with respect to organization and dedication. I especially

appreciate the guidance of Jim Berry, who not only helped me design and create critical experimental equipment, but also taught me a great deal about how electronics work and how to debug them. Also, it was truly a pleasure to work with Dr. Jae Cheon Kim, who I would like to thank for developing a simulation package that was used to validate many of the methods presented in this dissertation.

None of this would be possible without the loving support of my family. My wife, Sonal, motivated me to do a PhD in the first place and was always there to help when I found myself in difficult times. It is her passion for education that drives me to reach the highest level possible in my work. Likewise, my parents provided unwavering support for my decisions and encouraged me throughout my life to pursue my passions and make independent choices.

I would also like to thank my mentor from Pacific Northwest National Lab, Dr. Eric Smith, who originally sparked my interest in radiation detectors and encouraged me to pursue my graduate studies at the University of Michigan.

I would like to thank the Department of Defense Defense Threat Reduction Agency (DTRA) for their support through contract #DTRA 01-02-D-0067 and the Department of Energy Na-22 office through contract # DE-FG52-06NA27499. I would like to thank the Department of Homeland Security Scholarship and Fellowship Program, which paid my tuition and living expenses for the first three years of my PhD work.

TABLE OF CONTENTS

LIST OF FIGURES

Figure

LIST OF ABBREVIATIONS

WPCT weighting potential crosstalk

CAR cathode-to-anode ratio

GMI Gamma-Medica-Ideas

FWHM full width at half maximum

DOI depth of interaction

TAW time amplitude walk

HPGe High purity germanium

BNL Brookhaven National Laboratory

ASIC application specific integrated circuit

ADC analog-to-digital converter

TAC time-to-amplitude converter

ABSTRACT

Energy and Position Reconstruction in Pixelated CdZnTe Detectors

by

William R. Kaye

Chair: Zhong He

Pixelated CdZnTe detectors can achieve 3D position reconstruction, which enables 4π Compton imaging of gamma rays with a single detector and energy resolution better than 1% full width at half maximum (FWHM) at 662 keV. The detector configuration, readout electronics, event reconstruction algorithms, multiple-pixel event performance, depth reconstruction, and complications due to readout electronics are discussed.

In pixelated CdZnTe two dimensions of position sensitivity are determined based on which pixel collects charge. The third dimension comes from the signal ratio of the planar cathode to the pixelated anode, or, from the electron drift time for each pixel that collects charge. This work investigates the depth reconstruction using a collimated fan beam of gamma rays oriented such that counts are restricted to a narrow range of depths in a detector. The depth uncertainty is evaluated by measuring the fluctuation of the reconstructed depths of interaction. The depth accuracy is evaluated by calibrating the beam position and measuring the offset between the true depth of interaction and the reconstructed depth of interaction. Depth uncertainty

and accuracy better than 1 mm FWHM is achieved at 662 keV for both single and multiple interaction events in 15 mm thick CdZnTe detectors.

The energy reconstruction of pixelated CdZnTe is challenging for gamma rays that deposit energy on multiple pixels, due to factors such as signal crosstalk and system nonlinearity. This work details the impact of such factors on multiple pixel event energy resolution and, when possible, uses experimental data to put an upper bound on their effect. A correction is developed for the peak-hold circuitry of the readout electronics, improving the performance of events with at least three pixels that collect charge. The linearity of the system was also studied, especially as a function of the number of pixels that collect charge, resulting in energy resolution of 0.36% FWHM at 2614 keV. Finally, a summary of the detector issues that can cause poor event reconstruction is presented, as well as means to overcome these problems.

CHAPTER I

Introduction

Radiation plays an important role in society; it is used to diagnose disease, fight cancer, generate electricity, study the origins of the universe, treat our food, and develop weapons of mass destruction. This need to use radiation in day-to-day life has given rise to the field of radiation detection. When we encounter or use radiation there is a need for equipment that can perform specific measurements; medical radiation imaging relies on measuring where radiation is emitted or absorbed within the body, nuclear power plants must be monitored to ensure there is no accidental release to the environment, detectors are placed on satellites to study the universe, governments have a strong desire to detect the trafficking and possible detonation of nuclear weapons, and radon levels can be dangerously high in some regions requiring families to test in their homes.

The utility of a detector for a particular application usually comes down to its ability to answer one of three questions. The number of counts can be used to determine how much radiation is present. The energy levels of the radiation can be used to determine what type of radiation is present. Finally, image reconstruction techniques can be applied to determine where the radiation source is. In the case of a radon test in your home, the most important question is how much, as the type is already known and it is a problem regardless of where it is in your house. Attempting

to detect the smuggling of a nuclear weapon puts a high demand on determining what type of radiation is present based on the emitted gamma-ray energies, as there are benign radiation sources that must be ignored. Finally, in the case of a chest X-ray the top priority is to answer the where question. The goal of this work is to develop a radiation detector that can aid society's study of radiation by answering all three questions simultaneously.

1.1 Development of Pixelated Semiconductors

Gamma-ray spectroscopy, the process of identifying a radioactive isotope based on the energies of its emitted gamma rays, is a fundamental driver of radiation detectors. Detectors must have high atomic number and density in order to increase the probability that a gamma ray will deposit all of its energy. Furthermore, the device must be able to accurately reconstruct the amount of energy deposited, a parameter known as the energy resolution. Semiconductors have been the gold standard of gamma spectroscopy since the development of germanium detectors. However, germanium must be cooled well below room temperature to minimize the thermal excitation of electrons from the valence band to the conduction band. Scintillator detectors have long been the room temperature spectrometer of choice: the energy resolution is more than an order of magnitude worse than germanium but scintillators have proven to be affordable and fieldable.

The disparity between scintillators and germanium spurred the need for alternative room temperature semiconductors. Ideally, such a device would have a higher atomic number and density than germanium while achieving similar energy resolution, along with the room temperature operation and low cost of a scintillator. The community has long searched for the appropriate material to meet these requirements, focusing on wide-bandgap compound semiconductors such as HgI_2 (1), CdTe (2), GaAs (3), and later CdZnTe (4) and TlBr (5).

There were two major breakthroughs that enabled compound semiconductors as radiation detectors. The first was the invention of single carrier charge sensing techniques. Generally, the hole mobility in these compounds is more than an order of magnitude less than the electron mobility, thus the induced charge on the electrodes is due primarily to the movement of electrons. The use of the small pixel effect (6), a coplanar grid (7), or a virtual Frisch grid (8) all result in improved energy resolution when compared to a planar electrode configuration. Furthermore, reconstructing the depth of interaction in a device that uses the small pixel effect (9) results in a device capable of three dimensions of position sensitivity. This enables a more accurate correction of charge induction and collection non-uniformities while enabling Compton imaging in a single detector.

The invention of CdZnTe in the 1990s (4) has proven to be the other major breakthrough for compound semiconductors. CdZnTe is challenging to produce and typically has many defects, such as tellurium inclusions. An excellent review of these challenges has been published (10). In spite of these challenges, thicknesses greater than a centimeter have been achieved without polarization (11), the material is stable at room temperature, and energy resolution better than 0.5% FWHM at 662 keV has been demonstrated experimentally by our group.

1.2 Current Challenges

Fabricating a pixelated anode on a CdZnTe crystal has proven to be a useful technique, and has enabled a new class of portable high resolution imaging spectrometers. However, a significant amount of work remains before the optimal performance of these devices can be achieved. Improving the yield and quality of CdZnTe crystals has made the technology more viable, although there is still potential for further improvement, as the cost per gram of large volume crystals is still much higher than for small volume crystals. Likewise, the development of an application specific inte-

grated circuit (ASIC) to readout the signals from each electrode has enabled pixelated CdZnTe and represents an area where further improvements are possible, with respect to electronic noise, power consumption, and the information available for each event.

The energy resolution of single-interaction events within the device is already very close to the theoretical limit, given the noise of the readout electronics and the uncertainty in the number of charge carriers created. However, the energy resolution of multiple-interaction events is always poorer, due to factors such as nonlinearity, weighting potential crosstalk (WPCT), depth reconstruction, additional electronic noise, and charge loss to the grid. These multiple-interaction events are the only valid candidates for Compton imaging and their proper reconstruction is critical to identifying isotopes in different image regions. Thus, understanding and improving the energy reconstruction of multiple-interaction events is of paramount importance.

Another important consideration is improving the spatial resolution of the device. The position uncertainty will dominate the angular uncertainty in a single detector CdZnTe system, as the energy uncertainty is small and the position uncertainty will be large relative to the separation distance. Furthermore, the non-uniform charge induction and collection can only be corrected on a scale as fine as the position resolution of the system. Therefore, improving the position resolution is important for both imaging and spectroscopy.

Finally, the efficiency of the device is paramount. The major value behind room temperature semiconductors is that they are more easily fieldable than germanium. However, this is only true if a reasonable fraction of the interactions can be correctly reconstructed, otherwise, a larger volume of detector material would be required to match the existing technologies. The efficiency is improved by ensuring that all photoelectric events in the device are properly reconstructed. This is challenging for high energy gamma rays as well as events that occur near the pixelated anode surface, near the side surfaces of the crystals, and between two pixels.

1.3 Summary of Reported Progress

This work has focused on understanding and improving the energy resolution of multiple interaction events. A detailed discussion of the factors that degrade multiple interaction events, as well as measurements of the magnitude of each effect, is presented in Chapter IV.

The depth reconstruction of the device is much different between single-interaction events, where the cathode-to-anode ratio (CAR) can be used, and multiple-interaction events, where a drift time measurement is required. The difference in depth resolution between these two techniques has been studied using a collimated fan beam of gamma rays to better understand the possible sources of multiple-interaction event degradation. Chapter V shows measured results of both the depth uncertainty and depth accuracy for CAR reconstruction using a carefully calibrated collimator positioning system. Chapter VI shows the same results for drift time depth reconstruction and shows evidence of WPCT in the timing domain for two different ASICs.

An ASIC system from Gamma-Medica Ideas is studied throughout this work. Chapter VII discusses how a problem with the peak-hold circuit in this ASIC manifests itself as a major source of degradation for the energy resolution of multiple interaction events. A correction technique is developed and significant improvement in three and four pixel events is demonstrated.

Finally, Chapter VIII studies the nonlinearity of the system in detail. A pixelated device has a unique advantage with respect to correcting nonlinearities in the generation and collection of charge, as each gamma-ray interaction can be identified and corrected independently. Techniques for extending the single pixel nonlinearity correction to multiple pixel events are discussed. In particular, the correction of the nonlinearity across the entire dynamic range from 30 keV to 3 MeV is demonstrated.

1.4 Future Work

The most important direction that this work will take in the long term is the application of digital signal processing to the readout of pixelated detectors. Traditionally, an ASIC will sample the amplitude and timing information for each electrode and each event. The next generation of readout electronics, known as the digital ASIC, samples and reads out the preamplifier output pulse waveforms so that amplitude and timing information can be obtained using more advanced digital filters. This technology enables many new capabilities, such as position resolution finer than the pixel pitch (12) and reconstruction of multiple interactions over a single pixel (13). The extent to which this technology can close the gap in energy resolution between single interaction and multiple interaction events is yet to be seen.

When the energy of the gamma ray increases the size of the electron cloud created by photoelectric interactions grows. At some point, typically around 2 MeV, the electron cloud size is similar to the pixel size. The events are challenging to reconstruct for several reasons: they have a high probability of charge sharing between pixels, they induce large negative signals on the neighbor pixels, on the order of 100 keV, and the nonlinearity of each pixel is more challenging to correct because the probability of a single interaction photoelectric event being completely collected by a single pixel decreases as energy increases. Future work is needed to determine the best way to reconstruct these events. The digital ASIC has significant potential to improve these issues, as it samples the preamplifier waveform and can detect small depositions on neighbor pixels even with significant signal cross talk (14).

Another major challenge is to minimize the number of counts in the region between the photopeak centroid and the Compton edge. A low energy energy tail in the photopeak, a low peak-to-Compton ratio, and many counts in the Compton valley are often measured in CdZnTe detectors. For the most part, these issues have been corrected in the results that are presented in this work. However, the peaks are still

asymmetric and the sum of the counts in the Compton valley is about one third of the counts in the photopeak at 662 keV. Understanding the root cause of these events and how to properly reconstruct them is important for reaching the efficiency limit of the device.

CHAPTER II

Detector Overview

2.1 Introduction

The purpose of this work is to develop a 3D, position sensitive, gamma-ray spectrometer with excellent energy and position resolution. The device can then be used to precisely identify and locate isotopes of interest. In this work, the objectives are accomplished through the use of pixelated CdZnTe detectors. This chapter will begin by explaining, from a fundamental physics perspective, how these devices are capable of measuring the energy and position of each gamma-ray interaction. The intended applications of this technology will then be discussed and the chapter will end with a justification of the choice of pixelated CdZnTe for this work over other materials and device configurations.

2.2 Summary of Specific Systems

This work addresses factors that limit the performance of any pixelated room temperature semiconductor detector using any readout scheme. For example, the linearity of the system with regards to the energy deposited, discussed in chapter VIII, must be considered for any combination of detector and electronics. Pixelated detectors provide 3D position information that allow for more advanced techniques

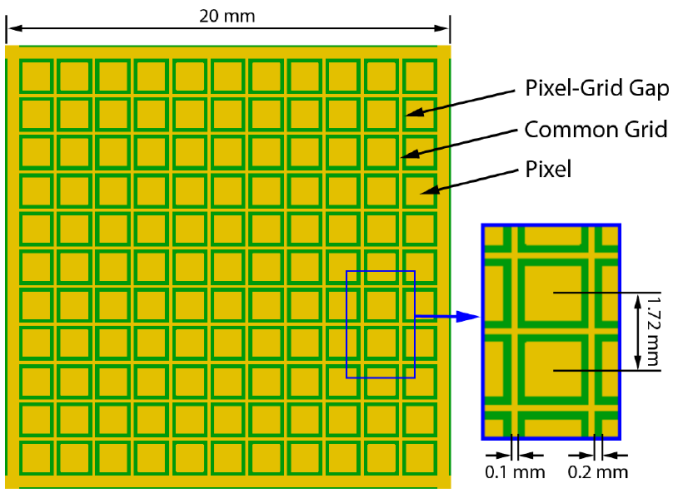

Figure 2.1: The anode electrode geometry for CdZnTe with a steering grid between the pixels. The cathode is a square planar electrode 20mm wide on the opposite side of the device, 15mm away from the anode (not shown).

to correct issues such as system nonlinearity or charge carrier trapping.

In order to illustrate and validate the techniques presented in this work measurements are taken using specific combinations of detectors and readout electronics. The vast majority of the results presented are collected using 15mm thick CdZnTe detectors grown and fabricated by Redlen Technologies (11). The anode pattern for these detectors is shown in Figure 2.1. There is a grid between all of the pixels; a small negative bias, between 30V and 200V, is applied to this grid in order to steer the electrons into the pixels.

With regards to readout electronics, three systems will be discussed in this work: the VAS_UM2.3/TAT4 ASIC from GMI, the H3D ASIC from Brookhaven National Laboratory (BNL), and the latest digital VAD_UM ASIC from GMI will be discussed. From here on they will be referred to as the GMI ASIC, the BNL ASIC, and the digital ASIC, respectively. The details of the readout scheme for each ASIC is discussed in section 3.1. The majority of the measurements are done on the GMI ASIC, the oldest and most readily available of the three. To illustrate certain concepts measurements must be done using the BNL ASIC, as it has lower electronic noise and differs

significantly in its timing pickoff routines. This work does not present experimental results from the digital ASIC, although this system has been studied for several years (14).

Another important consideration is the configuration of multiple CdZnTe crystals in a detector array. Packing multiple crystals into a single detector array improves the overall efficiency of the device. Many of the results presented in this dissertation are collected using an eighteen detector array system consisting of two planes of nine CdZnTe detectors each.

2.3 Detection Mechanism in Pixelated CdZnTe Detectors

2.3.1 Particle Interactions in CdZnTe Detectors

When a radioactive atom decays it may emit a variety of particles. Typically alphas, betas, neutrons, and gamma rays are of the greatest interest with regards to radiation detection. Alphas and betas are not very penetrating; a sheet of paper will stop alphas and a centimeter of aluminum will stop most betas, which makes them undesirable for many detection applications. Neutrons are very penetrating, but they are only emitted passively by the few isotopes that are capable of spontaneous fission. Gamma rays, on the other hand, are ideal in many ways: they are highly penetrating; measuring their energy provides unique information about the source identity; Compton imaging can be performed to localize their origin; and most radioactive atoms have will emit gamma rays when they decay.

While a gamma ray has no charge, it will still interact in CdZnTe through processes such as Compton scattering, photoelectric effect, and pair production. All of these mechanisms result in the transfer of energy from a gamma ray to an electron, positron, or both. These charged particles will directly interact with the atoms in the detector, losing their energy through mechanisms such as ionization, excitation of

atoms, and phonon generation (heat loss). Semiconductor detectors rely on the ionization process to generate electron-hole pairs. These charge carriers will drift through the semiconductor device under an applied electric field and in the process they will induce charge on electrodes fabricated on the semiconductor surface. The electrodes can be instrumented in order to obtain information for each radiation interaction.

This chapter will provide only a basic overview of the process of particle interaction, charge generation, and charge transport within a semiconductor. A book has been written that provides a general discussion of radiation detection principles and semiconductors as radiation detection devices (15). Another book explains the underlying semiconductor physics, such as the factors that effect carrier transport (16). Other publications provide a more detailed discussion, focusing on wide band-gap semiconductors such as CdZnTe (17) (10).

2.3.2 Electron Cloud Generation and Transport

A gamma ray can transfer the majority of its energy to a single electron, which will undergo many ionization interactions in the detector medium to give up this energy. These secondary electron interactions will result in a large number of spatially distributed electron-hole pairs, known as a charge cloud. The size of this charge cloud is important because it will influence device design factors such as pixel size.

A GEANT simulation found the electron range to be about 220 μm at 662 keV, 500 μm at 1.3 MeV, and 1300 μm at 2.6 MeV (18). This work is duplicated using an alternative particle transport code, MCNP5. The cloud diameter was calculated as the greatest distance between any two ionization points. The distribution of electron cloud size is shown in Figure 2.2 and excellent agreement with the GEANT results can be observed. It is important to note that the electron cloud size is not negligible compared to the pixel pitch of 1.72mm, which means there is a significant probability that a charge cloud will be collected by multiple pixels.

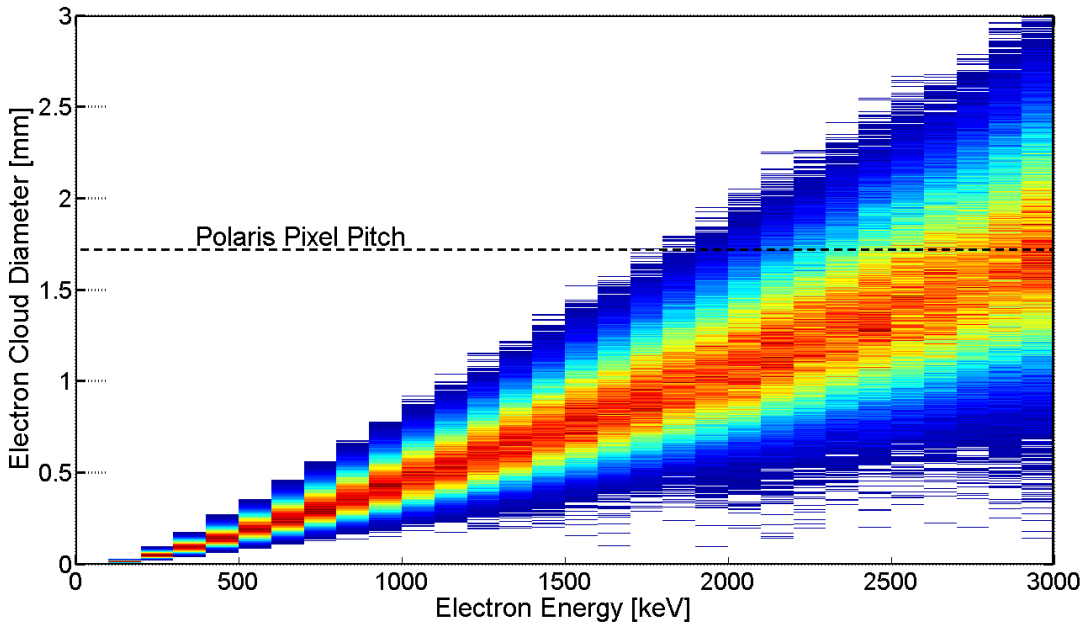

Figure 2.2: The electron cloud size distribution, calculated in MCNP, as a function of energy deposited. The pitch of the anode pixels is shown as a horizontal line for reference.

The key to detecting the radiation is not only in the creation of the charge itself, but also in the induction of charge on instrumented electrodes as the charge carriers drift through the semiconductor. An external bias is applied to the detector to force the electrons to drift toward the anode and the holes to drift twoard the cathode. An important consideration in CdZnTe is that the electron mobility-lifetime is typically two orders of magnitude higher than the mobility-lifetime of holes (19). Electrons have a higher mobility-lifetime because they move much faster than holes and are much less likely to get trapped for an extended time in the bulk material. As a result the electrons are the information carriers of primary interest when designing a CdZnTe detector.

The electron cloud will not maintain its original shape as it drifts through the bulk because the electrons will undergo random thermal motions in a process known as diffusion. The diffusion process typically expands the cloud on the order of 100 to 200 μm in a 15mm thick CdZnTe detector (18). For large energy clouds the difference

is insignificant, but the process is important because it places a lower limit on cloud size for events that drift through the bulk. For example, even if an alpha particle strikes the cathode surface and creates an extremely dense charge cloud, it will still diffuse to 100 to 200 μm before it is collected.

2.3.3 Charge Induction

Another key step in the radiation detection process for semiconductors is the generation of signals on electrodes which are instrumented with readout electronics. The fundamental principle is that the drift of the electron-hole pairs results in the accumulation of charge on these electrodes. A charge sensitive pre-amplifier can then be used to convert this charge information into a voltage signal, which is used to determine the amplitude and timing information for the event.

The most important element is the process of charge accumulation on the electrodes. A potential point of confusion is the belief that charge accumulation is due to the physical collection of charge by the electrodes: when the electron reaches an anode pixel or the cathode it increments the accumulated charge by one unit. This is a common misconception and an incomplete picture of the process. It is the movement of the electrons relative to the electrodes that results in charge accumulation, therefore the mechanism is based on charge induction rather than charge collection. A quantity known as the weighting potential is used to determine the charge induction on an electrode given a change in the position of the charge carriers.

A detailed description of how to calculate and apply weighting potential has been published (20). To summarize, the weighting potential is not an actual electric potential, rather, it is a tool to calculate the induced charge. The induced charge due to the movement of charge carriers is the difference between the weighting potential at the initial and final positions multiplied by the total amount of charge that moves. The weighting potential is calculated for a particular electrode by applying Poisson's

equation. The boundary conditions are specified by setting the weighting potential to one for the electrode of interest and zero for all other electrodes in the problem. Finally, the space charge is set to zero when applying the Poisson equation, as shown in equation 2.1,

$$\nabla^2 W = 0 \tag{2.1}$$

where W is the weighting potential. The weighting potential is a useful tool because it is simple to calculate for a device. Only knowledge of the electrode geometry and the dielectric constant of the material are required. The weighting potential calculated using the software MAXWELL3D is shown in Figure 2.3, based on the electrode configuration shown in figure 2.1.

The anode weighting potential is close to zero except near the anode itself. This means that the charge induced on the anode is basically independent of the depth of interaction and depends primarily on the energy deposited. The cathode has a weighting potential that changes linearly with depth. Therefore, the cathode signal amplitude should be directly proportional to the depth of interaction and the energy deposited. The ratio of the cathode to the anode signal (CAR) will then be a direct measure of the depth of interaction. Another technique to determine the depth of interaction would be to measure the timing difference between the start of charge movement, determined from the time when charge is first induced on the cathode, to the collection of all charge, determined based on the time when the anode signal rises rapidly.

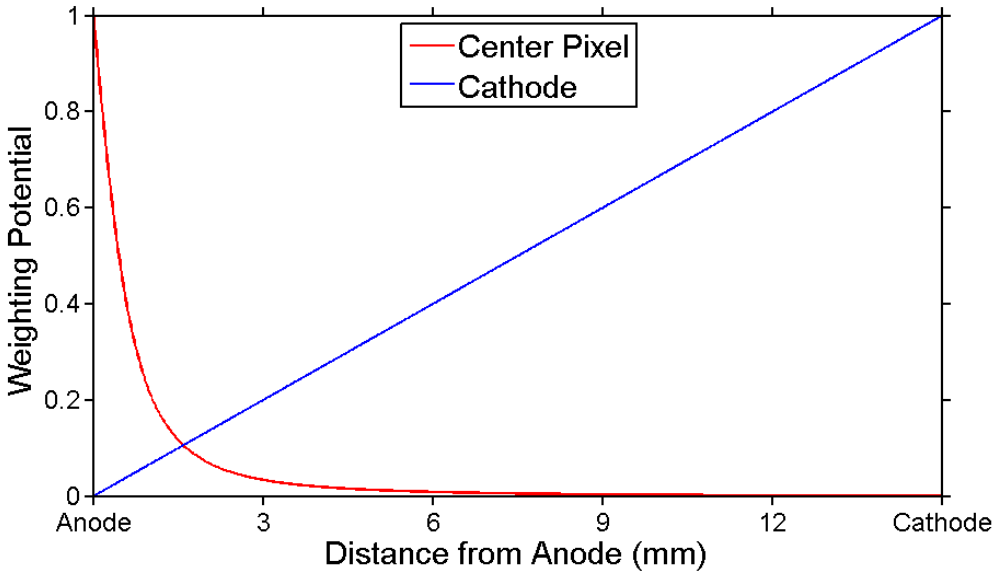

Figure 2.3: The weighting potential for the electrode configuration shown in Figure 2.1. The change in weighting potential between the initial and final charge carrier position is proportional to the total induced charge.

2.4 Applications of 3D Position Sensitive Detectors

2.4.1 Gamma Spectroscopy

Gamma spectroscopy is the process of generating a spectrum of energies deposited by gamma rays in the detector system. This spectrum can be used to identify the radioisotopes present near the detector as gamma rays are emitted with quantized energy. Many requirements must be met in order to achieve the ideal gamma-ray spectrometer. The most crucial factor is the ability to accurately measure the energy deposited by each particle, typically reported as the energy resolution of the peak FWHM where smaller values are better. For spectroscopy it is important that many of the gamma rays deposit all of their energy in the device, so material with a high atomic number and thus a high cross-section for photoelectric effect is desired. High-density detector material is also preferred to increase the overall probability that a gamma ray will interact. Finally, there are many gamma-ray spectroscopy scenarios, especially related to security applications, where the device must be used outside

of a laboratory environment. This means the detector must be relatively compact, lightweight, and durable.

There are numerous applications for gamma-ray spectroscopy, so the list presented here will be restricted to those targeted in this work. First and foremost the defense and security community wants a fieldable instrument that they can use to detect potentially threatening sources of radiation. The space science community is interested in gamma spectroscopy for applications such as measuring the energy signature of gamma-ray bursts or for studying soil composition on Mars. Nuclear facilities, such as power plants, have an interest in gamma spectroscopy for the purpose of monitoring the concentration and ratios of various isotopes within their facilities. Finally, applications such as decontamination and environmental monitoring often rely on gamma-ray spectroscopy to determine which isotopes are present.

2.4.2 Compton Imaging

Compton imaging is a method to obtain information about the location of a radiation source by applying Compton scatter kinetics to gamma rays that interact more than once in the device. Consider a gamma ray that first Compton scatters and then undergoes photoelectric effect within the detector. If the position and energy of each interaction is known then the Compton scatter angle can be calculated. A line connecting the two interaction locations forms the axis of a cone whose angle is calculated from the scatter angle. The gamma-ray event must have originated from the surface of this cone. After measuring several of these events the cones will begin to converge on the true source location.

This imaging technique has proven to be an extremely useful capability for situations that require gamma-spectroscopy. Furthermore, the development of CdZnTe detectors has increased the number of potential applications for Compton imaging due to their portability. A single CdZnTe detector can form a Compton image (21).

The defense and security community can use this capability to localize any threat sources they detect and discriminate against false positives based on the spatial distribution of the source. The space science community uses Compton telescopes to localize gamma-ray information without a bulky mechanical collimator (22). Compton imaging will allow nuclear facilities to localize isotopes in their plants. The biggest advantage, however, will probably be realized for the decontamination applications. With an imaging device the operator can localize the isotopes that emit gamma-rays without actually having to approach them, potentially preventing a significant dose.

2.4.3 Other Capabilities

The 3D position sensing capability of pixelated CdZnTe detectors enables additional imaging techniques. For example, coded aperture imaging, the process of placing a patterned attenuating mask near the detector and correlating the count distribution shadow to the source direction, is possible with this technology. Furthermore, a mask could be placed on each side of a single detector, in principle, such that all directions could be imaged simultaneously (23). There are also medical imaging techniques, such as small-animal Positron Emission Tomography (PET), that would benefit from the 3D position information.

Neutron detection is possible with CdZnTe due to the high cross section for capture of thermal neutrons in cadmium. When a neutron is captured by cadmium-113 it will emit gamma rays at 558.6 keV and 651.3 keV. The presence of peaks at these energies will indicate a neutron source is nearby (24). However, it is impossible to discriminate on an event-by-event basis between gammas, which are common, and neutrons, which are rare. This means that the sensitivity to neutrons will be a function of the gamma intensity, which is undesirable.

2.5 Motivation for Using Pixelated CdZnTe Detectors

The fundamental detection mechanism and the primary applications have been detailed for CdZnTe in the previous two sections. The purpose of this section is to justify pixelated CdZnTe as detector of choice for this work. First, a list of all the key advantages of CdZnTe will be presented. The chapter will end with a discussion of the limitations and challenges of CdZnTe for these applications.

2.5.1 Room Temperature

CdZnTe is classified as a wide band-gap semiconductor, with a bandgap energy of about 1.6 keV (15). This means that the probability of randomly exciting an electron from the valence band to the conduction band of the semiconductor is very low at room temperature, and thus stable operation is possible. High purity germanium (HPGe), the only technology that can achieve better energy resolution that CdZnTe with similar detector volumes, requires cooling down to 70K, which is undesirable for a fieldable device. It must be cooled before it is operated, which takes hours, and the detector must be thermally isolated from all other components in the system. This places demands on the engineering of the electronics, which must be low noise and connected directly to the detector electrodes. For these reasons, developing room temperature alternatives such as CdZnTe is an important priority.

2.5.2 Compact Design

If a small device is required that is capable of high resolution spectroscopy and Compton imaging, then CdZnTe is a good candidate. The fact that it does not require cooling to 70K helps reduce the device footprint relative to HPGe. Also, the high atomic number and density of CdZnTe mean that a high detection efficiency can be achieved in a small detector volume. Furthermore, a Compton image can be formed using a single crystal. Many Compton imaging devices, even modern ones (25), rely

on events that interact between two detectors to form an image. This is necessary in the absence of 3D position sensitivity. Arrays of 3D CdZnTe detectors are capable of imaging such events, but they can also image events that undergo Compton scatter and photoelectric effect within the same detector. Compton events occurring within one detector are measured to be more than an order of magnitude more probable than events between detectors in the case of an 18 detector array of CdZnTe crystals. Therefore, even a small device is still capable of performing Compton imaging when 3D position sensitive detectors are used.

2.5.3 Energy Resolution

Pixelated CdZnTe can achieve between 0.5% and 1.5% FWHM at 662 keV. Ultimately, the goal is to get as close to the performance of HPGe, about 0.2% FWHM at 662 keV, as possible. The closest remaining competitors are alternative room temperature semiconductors, such as HgI_2 or TlBr. However, at the time of publication neither of those materials could be made with the same volume, performance, and yield as CdZnTe. Beyond that there is a significant performance gap until the next major competitor, scintillation detectors. Recent breakthroughs in scintillator materials have allowed energy resolution close to 2.5% FWHM at 662 keV for $LaBr_3$ (26) or SrI_2 (27), but still significantly worse than CdZnTe.

2.5.4 Spatial Resolution

The 3D position measurement capability of pixelated CdZnTe detectors is useful for several reasons. It enables multiple imaging techniques. It also offers event classification capabilities. For example, a spectrum could be made of only events that interact in the detector four times or more, increasing the peak-to-Compton ratio. If a region of the crystal is known to be bad then those events could be discarded. Different interaction types, such as pair production, can be identified due to their

predictable pattern of energy depositions and positions.

Many detectors do not have any position information, which means that arrays of detectors are required to obtain position information. Some pixelated detectors are operated with only two dimensions of position sensitivity, in which case two planes of detectors could be used to create a relatively low efficiency Compton image.

There are only a few other devices that are capable of achieving 3D position sensitivity. One is the cross-strip germanium detector (28). This detector scheme has excellent position and energy resolution, but is challenging to field, as it requires cooling and many more electronic connections between the germanium, at 70K, and the electronics than a conventional HPGe readout scheme. Furthermore, the signal crosstalk between interactions is more severe for strips than for pixels. CdZnTe has also been fabricated in a cross-strip configuration, but those devices have not been able to achieve the same spectroscopic performance as pixelated devices, with a FWHM of 8% at 122 keV (29).

2.5.5 Potential to Correct Material Non-uniformity

Section 3.2.2 discusses the process of using position information to improve the accuracy of the energy deposition measurement. This is useful in the case of a device without a uniform response to all interaction positions, which is common in room temperature semiconductor crystals such as CdZnTe. Therefore, choosing pixelated CdZnTe over alternative device configurations such as a virtual Frisch grid (30) (31) or a coplanar grid (7), which lack position sensitivity, enables the use of poorer material.

Furthermore, the leakage current through the bulk of the semiconductor can influence the noise of the system, depending on the resistivity of the material. However, each pixel in a pixelated device only collects a fraction of the total bulk leakage current and the noise for each pixel is much smaller than for a planar electrode.

2.5.6 Disadvantages of CdZnTe

The use of CdZnTe has been limited by its expense and the difficulty to grow high quality crystals. Beginning with the expense of pixelated CdZnTe system, biggest factor is the cost of the CdZnTe crystal, which was purchased for $7500 per detector during my time at the University of Michigan. That works out to $1250 per cubic centimeter of CdZnTe and a cost of $135,000 for an eighteen detector array. This is likely due to the immaturity of the growth process. Thinner CdZnTe detectors have been grown for medical applications and were also used in this work, purchased at $150 per cubic centimeter. If the thick detectors can be fabricated at a similar price-to-volume ratio, CdZnTe will be able to enter more markets.

However, the cost will probably never drop significantly below that of medical grade CdZnTe, due to inherent difficulties in the growth and fabrication process. Therefore, CdZnTe will never be the detector of choice when the number one priority is obtaining a large number of counts at a low price. In this case large volume scintillators will be used for quite some time.

The complication in making a CdZnTe device is largely tied to the need to read out data from each pixel of the device independently. In the case of an 18 detector array with 121 pixels per detector more than 2000 readout channels are required. This means that the readout electronics must be designed to fit into a very small footprint and consume as little power as possible. The power is generated in a relatively small space and the heat must be removed.

Adding to the complication is the fact that a computational process must be performed to convert the raw signals from the electronics into the energy deposition and position of each interaction. This will be discussed in detail in Chapter III. Our research group has worked on the problem continuously for over a decade.

One last disadvantage that should be noted is the inability to distinguish neutrons on an event-by-event basis. If an event-by-event discrimination technique was devel-

oped it would have great potential, as the thermal neutron interaction probability is large in CdZnTe and the 3D position information could be used to perform some rudimentary neutron imaging (32).

CHAPTER III

Readout Electronics and Event Reconstruction

3.1 Event Readout

In a pixelated device each pixel should be connected to an independent preamplifier. In an ideal system all of these preamplifier signals would be continuously sampled in roughly 10ns intervals. In this configuration digital signal processing could be applied to each of the preamplifier signals to identify particle interactions. If two events recorded on different pixels are closely correlated in time than this would probably be classified as the track for a single incident particle. Anode waveforms would be correlated with the cathode waveform to determine the depth of interaction for each event.

The continuous sampling scheme provides the complete picture of what happens at every moment of time. It allows for robust event identification algorithms, baseline correction, and many other capabilities. Such a system would be necessary when event-by-event data is needed at a very high count rate such as in a spectroscopic computed tomography device. However, the data output from the system would be difficult to manage in real time. Assuming each pre-amplifier sample is described by 2 bytes, samples are taken every 10ns, and an array of eighteen detectors each with 121 channels is used, the readout system would have to handle a data collection rate of over 400 gigabytes per second. It is unlikely that this kind of bandwidth will be

available in a personal computer in the near future.

This leads to the inevitable tradeoff of data readout. Ultimately we must sacrifice some amount of information for the sake of data compression. Reading out all data at all times from all pixels is not yet practical. The concept of triggered readout is used to selectively sample data only when something interesting happens in the device. Consider a device with an event rate of 1000 per second and a maximum rise time on any electrode of 1μs: the probability of observing useful event information at a particular time is at most 0.1%. To capitalize on this relatively low event rate, data can be read out from the preamplifiers only when a trigger signal is generated, at which point the system typically experiences from some amount of dead time.

This section focuses on how to parse the data available on the preamplifiers down to the minimum information necessary to describe the history of one particle that interacts in the detector. The techniques used by the analog GMI and BNL ASICs will be discussed, as well as the digital ASIC from GMI.

3.1.1 Sparse Readout

When a trigger is generated in any pixel or cathode of any detector of an array system based on the GMI ASIC the signal from every preamplifier is read out. This requires the acquisition of over 2000 samples for an eighteen detector array. This readout technique is known as full readout; while it provides the maximum possible information from the system it tends to result in a relatively large dead time, on the order of 500 μs for an eighteen detector array system coupled to the GMI ASIC.

An alternate scheme is to only read out signals from the detectors or pixels of interest. Sparse detector readout refers to reading out the preamp signals only from the detectors that generated a trigger signal. In the case of an eighteen detector array, this would represent about an order of magnitude reduction in the required data transfer rate. Sparse pixel readout goes even further, such that only the pixels that

actually generate trigger signals are read out in addition to the cathode. Typically, the pixels neighboring the triggered pixel are also read out for various purposes. Sparse pixel readout would represent a reduction in data output from an eighteen detector system by about two orders of magnitude. However, the pixels that do not collect charge are still useful for baseline correction, discriminating between true signals and noise, and eliminating certain components of the electronic noise.

3.1.2 Preamplifier Readout

The extraction of data from the preamplifier is a critical step in optimizing the performance of any spectroscopic gamma-ray detector. Passing the signal to one or more shaping amplifiers and extracting pulse height and timing information has proven to be a practical scheme. Only two scalar values are read out per pixel, which results in a short readout time. Energy resolution better than 0.5% FWHM at 662 keV has already been achieved using this readout scheme (33), which will be referred to as an analog ASIC.

However, the signals generated on a particular preamplifier often cannot be described accurately by a single amplitude and time. Examples include two interactions occurring over a single pixel, or even over neighboring pixels in some cases. For this reason and many others such as event classification (34) and subpixel resolution (12) it is desirable to directly sample the preamplifier waveform. In what is referred to as the digital ASIC, each preamplifier signal of interest is sampled with a period as short as 12ns to capture the waveforms generated in CZT. Algorithms can be developed on a computer to properly analyze each event (14).

It is critical to minimize the contribution of electronic noise during the preamplifier signal extraction process to achieve the best possible energy resolution. This is done by determining the shaping time that minimizes the electronic noise. This has been done for CdZnTe detectors with planar electrodes and with strip electrodes; an

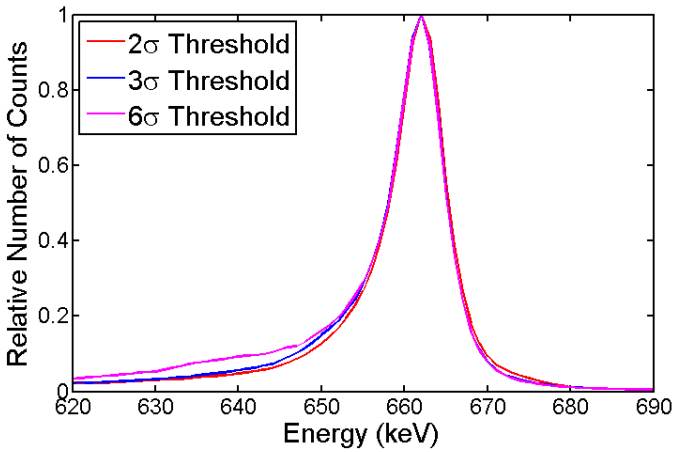

Figure 3.1: Photopeak 662 keV events from detector 4R143 using the GMI ASIC at three different noise discrimination thresholds, specified as a number of standard deviations above the fluctuation of the baseline. Data is shown for 1, 2, 3, and 4 pixel events combined.

optimal shaping time near 1μs was found (35). In the case of an analog ASIC the amplitude signal for both the cathode and anode is determined with a shaping time of approximately 1μs.

3.1.3 True Signal Determination

The GMI ASIC operates in full readout mode, thus up to 2178 pixel amplitudes are available for each event read out by an eighteen detector array system. It is critical to determine which pixels collected charge for each event. This is done by setting a noise discrimination threshold for each pixel and only recording signals from pixels that pass this threshold.

Figure 3.1 shows the impact on the energy spectrum of the true signal threshold. If it is set too high then events appear below the photopeak because true energy depositions are discarded. If it is set too low then events appear above the photopeak due to noise events recorded as false energy depositions.

The problem of discriminating true energy depositions from noise is a fundamental challenge in every readout scheme. In sparse pixel readout the system only reads

out pixels that trigger along with their neighbors. In this case the readout scheme determines which pixels collected charge. However, it is important to set the lowest possible trigger threshold in this case to ensure that all true energy depositions are recorded. It is also important to read out the pixels that neighbor the triggered pixels in case a small amount of charge was shared. Discriminating between small energy charge sharing events and noise is another major challenge in pixelated devices.

3.1.4 Baseline Correction

In this context the baseline value of a preamplifier will be defined as the average recorded amplitude when no charge is collected. In an ideal system each preamplifier will have a constant baseline value, regardless of time, temperature, or other operating conditions. Often this is not the case and some form of baseline correction is necessary.

In order to properly correct baseline shift it is important to monitor the baseline of each pixel. In a digital system this can be done on an event-by-event basis, as the preamplifier amplitudes will be sampled before and after charge collection. This is not possible in an analog system that reads out a single amplitude, as this amplitude is affected both by the collected charge and the baseline position.

Dr. Feng Zhang developed a technique to monitor the baseline position of each preamplifier in an analog system operating in full readout mode (18). The baselines are calculated for each system dump, which occurs after a sufficient number of events have been collected, typically around 1000. For each event, the amplitude of each pixel that does not collect charge above the true signal threshold is passed to the baseline determination algorithm. When a system dump occurs these amplitudes are averaged for each pixel. In this scenario the baseline value is available for each pixel and is updated every few seconds, depending on count rate.

There is no known technique for determining the baseline position as a function of time for an analog system that reads out a single amplitude value and operates in

sparse readout mode. At least two amplitude values would be required for each pixel for each event to monitor the baseline in this readout configuration. Fortunately, in the BNL ASIC the baseline position does not change rapidly, as excellent energy resolution is achievable without realtime baseline correction. The GMI ASIC, however, does require this baseline correction and the cause for the disparity in this behavior is not well understood.

3.1.5 Common Mode Noise Correction

The electronic noise is a major factor in pixelated CdZnTe detectors. If the noise between the pixels is correlated then it may be possible to reduce the noise by applying a common mode noise correction. When a detector is set to full readout mode then noncollecting pixels will be read out and report a value near their baseline. The difference between each pixel and its baseline are averaged and will be systematically high or low for that event if there is common mode noise. The values in the collecting pixels are then shifted based on the baseline offset of the noncollecting pixels.

It should be noted that this technique will only work well in the case that the baseline value is representative of the true noise impact on each noncollecting pixel. This may not be the case, however, as the baseline could be due to a transient signal preserved by the peak-hold. Furthermore, this technique cannot work in sparse readout mode, as the baseline values are not available for the non-collecting pixels in each event.

3.1.6 Circuit Overview

Figure 3.2 provides an overview of the readout circuit used for each pixel in the analog GMI ASIC. This is the circuit that is used for most experiments in this work. For the cathode channel the signal polarity is reversed. For the BNL ASIC the triggering and time pick-off behavior is slightly different. For the digital ASIC

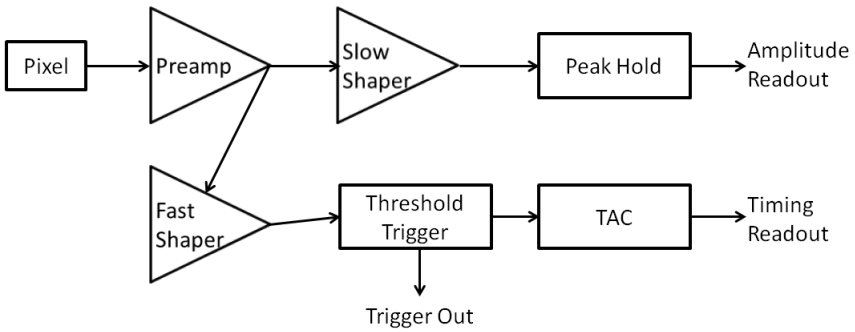

Figure 3.2: Overview of the circuit used to read out one pixel in the GMI ASIC.

the preamplifier output is sampled directly and the values are read out through an analog-to-digital converter (ADC).

3.2 Event Reconstruction

Event reconstruction is the process of converting the raw ASIC data into the best estimate of the position and energy deposited for each gamma-ray interaction. The majority of this dissertation will be focused on studying detailed aspects of this conversion process. The remainder of this chapter will be dedicated to explaining the event reconstruction techniques currently implemented at the University of Michigan. The majority of these algorithms were originally implemented on a pixelated CdZnTe system by Dr. Feng Zhang (18).

3.2.1 Calibration of the Cathode-to-Anode Ratio

The CAR is used extensively throughout the calibration process, as many of the later calibrations are dependent on accurate reconstruction of the depth of interaction. Therefore the proper implementation of the CAR is critical.

In an ideal system, the equation used to calculate the depth of interaction for a single-interaction event is given by equation 3.1,

$$z = T\frac{C}{A} \tag{3.1}$$

where z is the depth of interaction, T is the device thickness, C is the cathode signal amplitude, and A is the anode signal amplitude. In this idealized system the cathode and anode signals are assumed to have no baseline offset, identical gains, and a perfectly linear amplitude response.

In a more realistic system such as the GMI or BNL ASICs, there will be baseline offset, varying gain between pixels, and nonlinear preamplifiers. In this case the terms in equation 3.1 labeled C and A are more challenging to obtain. Ideally, a nonlinearity correction would be applied to the raw anode and cathode amplitudes. However, without knowing the depth of interaction it is challenging to perform a nonlinearity correction because the anode signal is influenced by depth dependent trapping.

There are several techniques to overcome the problem. One is to use an iterative technique: ignore trapping to get a rough nonlinearity correction, then do a rough depth reconstruction to get a better nonlinearity, which is used for a better depth correction, and so on. Iterative techniques are generally undesirable if the problem can be solved directly. This leads to a technique where the cathode signal is used to filter for cathode side events which are used as the sole input to perform the nonlinearity correction. However, this means that each source must be counted for a long enough time to acquire an adequate number of cathode side events.

The calibration sequencing issues described above represent one set of concerns. Another challenge is developing the algorithm for measuring the gain, offset, or nonlinearity of the anode and cathode. Once the depth-dependent nonlinearity issues described above are addressed the anode signal can be calibrated using photopeak centroids. The cathode spectrum, however, will not necessarily contain a peak. During calibration a source must be placed on the cathode side to ensure that the low

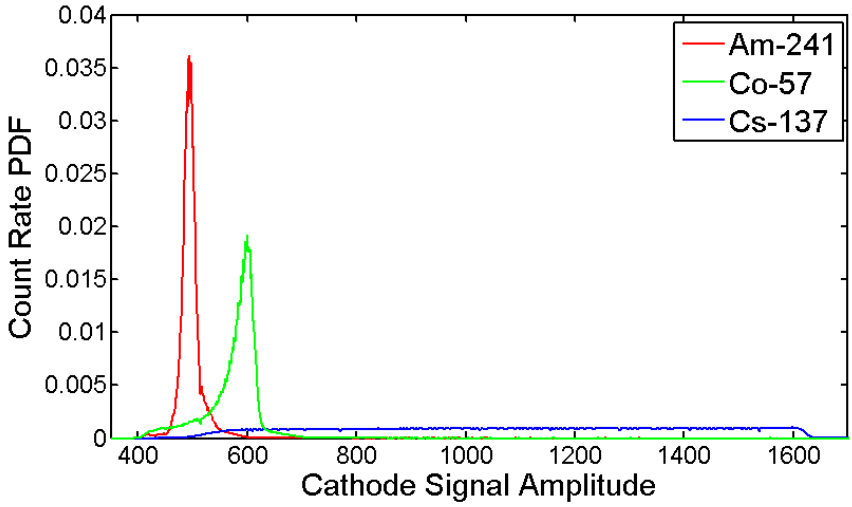

Figure 3.3: The cathode spectra of photopeak events for three different sources.

energy gamma-rays will interact in all of the pixels. The cathode spectrum of photopeak events will contain a relatively flat continuum for gamma-ray energies that result in a mean free path similar to or greater than the detector thickness. When events from a low energy source are used, gamma-rays will only interact near the cathode surface, so the cathode spectrum will generate a peak due to the large number of photoelectric events occurring in a narrow range of depth bins. To illustrate these cases, Figure 3.3 shows the spectrum from the 60 keV gamma from Am-241, the 122 keV gamma from Co-57, and the 662 keV gamma from Cs-137.

In the low energy case the centroid should be used to determine the cathode amplitude, but at higher energies an edge detection algorithm must be used. It is difficult to select an edge detection algorithm that gives the same answer that the centroid would give in the case that only cathode side events are included. If the true shape of the cathode distribution could be known then it would be possible, but the key edge feature is influenced strongly by both the system noise and the interaction location distribution. Thus, simulation of the expected interaction locations and a description of the system noise as a function of energy would be required to properly deal with this problem.

The reader should take away from the above discussion that it is difficult to calibrate the CAR without making approximations. Therefore, it is important to understand the impact of these approximations, which will degrade the depth reconstruction, on the energy resolution of the device. This requires a derivation of the relationship between the depth uncertainty and the energy uncertainty. First, consider equation 3.2, which shows the reconstructed energy, $E(n)$, is dependent on the measured amplitude after baseline correction, $A(n)$, and the gain of the voxel where the interaction is measured to occur, $g(n, z)$, where n is the detector pixel and z is the depth of interaction in millimeters.

$$E(n) = A(n)\ g(n, z) \tag{3.2}$$

For the sake of this derivation, the gain is defined relative to the cathode side amplitude. Furthermore, the depth will be defined as zero at the cathode and as a maximum at the anode. Generally a depth of zero represents the anode, but the opposite definition will be used here in order to simplify the derivation. Finally, if we assume that the photopeak amplitude decreases linearly toward the cathode, meant to model the effect of electron trapping, we get equation 3.3.

$$g(n, z) = \frac{E_0}{A_0(n, z)} = \frac{E_0}{A_0(n, 0)(1 + zs)} \tag{3.3}$$

In this context $A_0(n, z)$ is the amplitude measured during the calibration process for depth z in pixel n, E_0 is the energy of the calibration source, and s is the percent change in the photopeak position per millimeter. Equation 3.4 is obtained by applying the error propagation formula (15) to the measured energy equation.

$$\sigma_E^2 = \left(\frac{\partial E}{\partial z}\right)^2 \sigma_z^2 \tag{3.4}$$

Where σ_z is the depth uncertainty and σ_E is the energy uncertainty. If we plug in

equation 3.4 into 3.2, we will get to equation 3.6.

$$\sigma_E^2 = \left(\frac{-sAE_0}{A_0(n,0)(1+zs)^2} \right)^2 \sigma_z^2 \tag{3.5}$$

$$\sigma_E = \frac{sAE_0}{A_0(n,0)(1+zs)^2} \sigma_z \tag{3.6}$$

Finally, we are more interested in the energy resolution as a percentage then the energy uncertainty in units of energy. Dividing by the energy yields equation 3.7.

$$\sigma_E = \frac{s}{(1+zs)} \sigma_z \tag{3.7}$$

The denominator in equation 3.7 will be small if the trapping is small. Thus, for most detectors it is reasonable to simplify to Equation 3.8.

$$\frac{\sigma_E}{E} \simeq s\sigma_z \tag{3.8}$$

Equation 3.8 tells us the uncertainty due to the depth reconstruction is quite small for most detectors. In the case of a detector with 3% trapping through the bulk and 1 mm depth uncertainty the photopeak uncertainty would only be 0.2% FWHM due to depth uncertainty. Most Redlen detectors have less than 3% trapping and depth uncertainty around 1 mm, so this relatively small photopeak broadening represents an upper bound for good material.

Showing that depth uncertainty has a small effect on energy uncertainty is key to showing that approximations in the calibration of the CAR are acceptable. It is the most challenging to calibrate the CAR at low energies, but in this case the uncertainty is dominated by system noise, so a slight depth miscalibration is inconsequential. Other problems come into play at very high energies, where the linearity of the preamplifiers is typically the poorest, but once again the energy uncertainty is

dominated by other factors at those energies. Thus, from an energy reconstruction perspective, as long as all of the depths are calibrated correctly within 1mm the impact will be relatively small. In later chapters I will show that it is possible to achieve this level of accuracy using only a simple baseline offset and gain for each channel.

Another question is how possible miscalibration of the depth of interaction could effect the imaging performance. For Compton imaging the depth is always reconstructed using drift time. The drift time is correlated to the CAR at 662 keV and the energy dependence of drift time is handled with a time amplitude walk (TAW) correction. Therefore, as long as the CAR is calibrated properly at 662 keV, it will have no negative impact on the Compton imaging performance. Proper calibration at 662 keV can be achieved with a simple baseline offset and gain.

Coded aperture imaging is the most demanding application with respect to depth reconstruction using the CAR. If the aperture mask is placed above the cathode side then the depth plays a small role, but if placed above a side surface then the depth of interaction must be well calibrated or the image reconstruction will degrade. In this case an accurate calibration of the CAR, especially at low energies, is critical.

3.2.2 Depth Dependent Energy Calibration

Calibration of the photopeak position as a function of depth of interaction for each pixel is the most critical step in achieving excellent energy resolution in a large volume pixelated semiconductor. The correction is required because devices are known to have a depth dependent response due to weighting potential and trapping as well as a 3D position sensitive response due to material non-uniformity.

The basic principle is to divide a detector into a large number of voxels for independent calibration. We typically use 11 bins in each pixelated dimension and 40 bins along the depth dimension, resulting in almost 5000 voxels that require calibration. A large number of events, typically around 50 million, are recorded for each

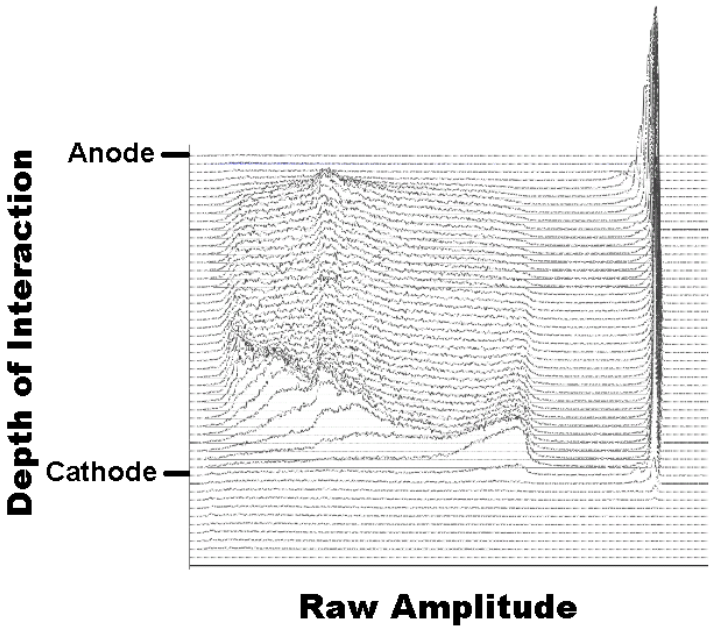

Figure 3.4: Depth separated spectrum for one pixel in detector 4R143 using the GMI ASIC. Events are from a Cs-137 source.

detector. A Cs-137 source is used for its strong single emission line, adequate penetration depth, and reasonably high probability of single-interaction photopeak events in CdZnTe. Only events that trigger one pixel (single-pixel events) are used for this calibration. For each event the depth of interaction is determined by the CAR, which will be discussed in the next section, while the other two dimensions are determined based on which pixel collects charge. Using this information, and approximately 50 megabytes of computer memory, a spectrum can be generated for each detector voxel. The spectrum at each depth for one pixel is shown in Figure 3.4.

The 662 keV photopeak position from Cs-137 is found in each voxel's spectrum. The position of these peaks will be a function of trapping, weighting potential, and charge generation, and may be further complicated by system problems such as the ASIC peak-hold. Fortunately, these effects are stable and repeatable for a particular combination of ASIC and detector, as the photopeak positions do not move significantly after months at bias and multiple power cycles.

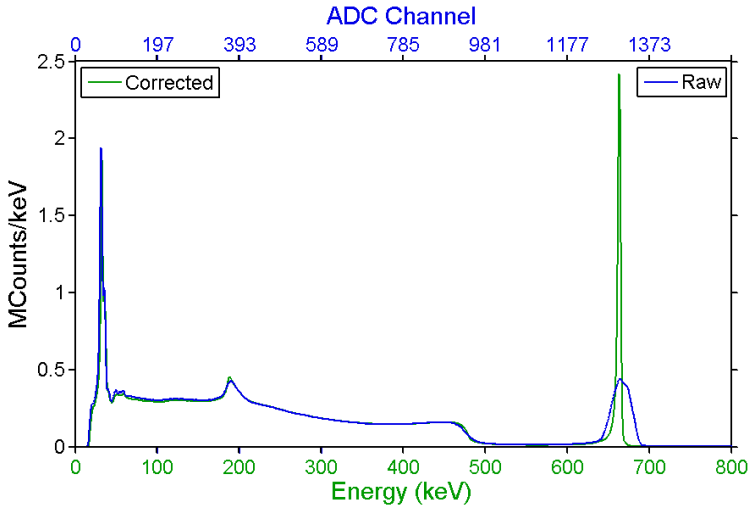

Figure 3.5: The blue curve shows the spectrum of single-pixel events from a Cs-137 source before correction and the green curve shows the spectrum after depth dependent energy calibration. The energy resolution improves from above 3% to 0.5%.

Once the centroid position is known for each voxel, an event-by-event reconstruction technique can be utilized. The energy deposited is given by equation 3.9,

$$E(n) = (A(n) - B(n))g(n, z(n)) \tag{3.9}$$

where E is the calculated energy deposition in pixel n, $A(n)$ is the raw signal recorded on pixel n, $B(n)$ is the associated baseline value, and $g(n, z(n))$ is the gain associated with the depth of interaction, $z(n)$, in pixel n. The gain term is calculated by equation 3.10,

$$g(n, z(n)) = \frac{E_{Photopeak}}{\langle A_{Photopeak}(n, z(n)) - B(n) \rangle} \tag{3.10}$$

where $E_{Photopeak}$ is the emission energy of the calibration source, 662 keV in the case of Cs-137, and the denominator is the average value of photopeak events in pixel n at depth $z(n)$ after baseline subtraction.

This correction results in a significant improvement in the energy resolution, an example is shown in Figure 3.5.

3.3 Drift Time Calibration

In order to be useful as a Compton imaging device a readout system must be capable of measuring both timing and amplitude information for each charge collection event. This requirement implies that all single-interaction events will have redundant depth information, as both the CAR and the drift time will be indicators of the interaction depth.

It is critical to determine which parameter is the most accurate indicator of the true depth of interaction. For a detector with good electron mobility, poor hole mobility, and uniform drift velocity throughout the bulk both the drift time and the CAR will be accurate indicators of depth.

As the hole mobility-lifetime product increases then the holes begin to play a role in the amplitude of the cathode signal. If the holes travel a distance R_H within the charge integration time for the cathode signal, then all events that interact at a depth less than R_H from the cathode will generate the same cathode amplitude. In this scenario, all events near the cathode appear at the same depth when using the CAR while the drift time reconstruction is unaffected. A similar situation arises when the integration time for the cathode signal is less than the maximum electron drift time. In this case ballistic deficit results in the depth of interaction blurring together for cathode side events when using the CAR.

It is possible to select a shaping time long enough to capture the full induction of an electron drifting through the bulk. For typical Redlen CdZnTe the holes travel very slowly (19) and play little role in the charge induction. For these reasons the CAR is usually a very accurate measure of the depth of interaction. The accuracy of the drift time reconstruction will degrade if the drift velocity is not constant from the cathode to the anode. In principle, this could be caused by non-uniform electric field or electron mobility. In either case, each drift time will still be uniquely correlated to a particular depth of interaction, but the relationship will no longer be linear. This

scenario is very common in CdZnTe from Redlen Technologies.

Ultimately the CAR has proven to be the most accurate indicator of the depth of interaction given the charge transport properties of modern CdZnTe. However, the drift time must be used when reconstructing the depth of interaction of multiple-interaction events. To rectify this situation, the relationship between the CAR and the drift time is calibrated under the assumption that the CAR is the correct indicator of depth. Then, the timing value of each event can be converted to a CAR value.

This calibration is achieved by generating a drift time distribution for photopeak events for each CAR bin of each pixel of the system. The centroid of each drift time distribution is used to find the drift time associated with each CAR bin. These centroids are fitted with a polynomial function that provides the CAR associated with a particular drift time. An example of this relationship is shown for a pixel with uniform drift velocity and for a pixel with non-uniform drift velocity in Figure 3.6.

For single-pixel events it is still unclear whether the CAR or drift time should be used to reconstruct the depth of interaction, as both will be accurate once their relationship is calibrated. In this case the most consistent indicator of depth is desired to minimize the uncertainty in the energy reconstruction. In the GMI ASIC the drift time is degraded by high frequency noise while the CAR is degraded by lower frequency noise. The uncertainty of each reconstruction technique will be measured experimentally in later chapters.

3.3.1 Time Amplitude Walk Calibration

The timing pickoff technique used on the anode and cathode timing signals will determine whether or not the system will require a TAW correction. The influence of TAW on these signals is important because both timing signals are required for accurate measurement of the drift time. A system that samples the preamplifier waveforms, such as the digital ASIC, should not be influenced by time walk as robust

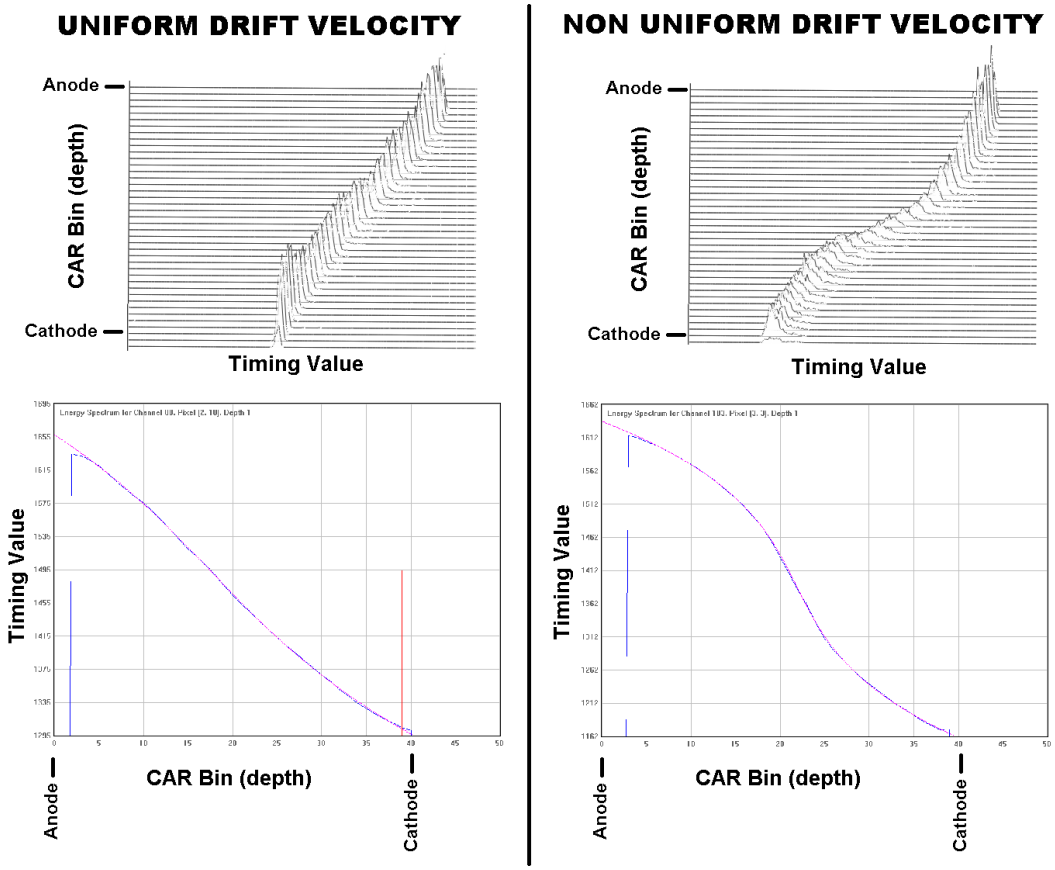

Figure 3.6: The top two plots show the timing spectrum for each depth of interaction in two different pixels. Below is the fourth order polynomial fitting function used for calibration of each pixel.

time pickoff techniques can be applied in digital signal processing. The BNL ASIC uses the peaking time of the shaped signal to determine the anode trigger time, which is not influenced TAW. However, a simple threshold timing trigger is typically used for the cathode timing pickoff in the BNL ASIC and to determine all timing values in the GMI ASIC. These signals experience significant TAW and must be corrected.

The TAW associated with each timing value will be a function of the charge induction rate during the rise of the pulse. It is therefore dependent on the drift velocity and the signal amplitude. In the case of the GMI ASIC both the anode and cathode signals have TAW and must be calibrated independently. To accomplish this goal, two interaction photopeak events are used. In this case the total energy deposited is always the same and thus the cathode TAW is always the same. However, the energy collected by each pixel can vary from the minimum energy required to trigger the timing circuit up to almost the photopeak energy. In this way the relative timing signals will only be affected by the anode TAW. Timing spectra are generated for a set of anode amplitude bins. The maximum drift time is associated with cathode side events. If TAW is a factor, this maximum drift time will be greater for smaller amplitudes than for larger amplitudes. The anode TAW is thus corrected by applying equation 3.11 to the drift time calculated in each pixel such that,

$$t(n) = t_{raw}(n) + (t_{cathode}(A_{cal}) - t_{cathode}(A(n))) \tag{3.11}$$

where $t_{raw}(n)$ is the measured timing value in pixel n before anode TAW correction, $t_{cathode}(A_{cal})$ is the timing value for cathode side events at the calibration amplitude, A_{cal} typically associated with 662 keV, and $t_{cathode}(A(n)))$ is the timing value for cathode side events for the signal amplitude of this pixel, $A(n)$. The calibration values shown in 3.11 are not unique to each pixel. In principle the drift velocity can be different in each pixel, so they should each get their own TAW calibration, but correcting this effect would require a significantly longer measurement time to

calibrate.

Once the anode TAW has been calibrated it is possible to calibrate the cathode TAW independently. This can be done using single-pixel events from the photopeak and Compton continuum. In this case both the anode and cathode signals will experience TAW walk, but the anode correction coefficients determined in the previous step can be applied. The CAR can be used to filter for cathode side events. In this case a timing spectrum with a peak will be generated for each amplitude bin, as expected for events from a single depth. Equation 3.11 can then be applied to correct the cathode TAW, using these timing centroid values and the amplitude of the cathode signal.

3.3.2 Weighting Potential Crosstalk Calibration

In the case of multiple-interaction events it is important to understand that the signal recorded on any one pixel will be influenced by the electron clouds from all other interactions in the detector. The amplitude recorded by a pixel is affected primarily by the electrons collected directly by that pixel. However, any electron that is collected by other pixels will end at a weighting potential of zero when it reaches the anode. Unless these electrons are generated very near the anode or cathode than the initial weighting potential is non-zero, which implies the net charge induction has the opposite polarity of the collected charge. In this way, the total signal amplitude of multiple-interaction events is reduced due to an effect that is known as WPCT.

The signal deficit on a particular pixel will depend entirely on the location and magnitude of energy depositions in other pixels. A technique to eliminate this undesirable influence has been developed (18). The 2-pixel photopeak events with both interactions occurring at nearly the depth are used. By requiring that the events occur at the same depth the result is that the initial weighting potential of the uncollected clouds are the same for both pixel. In this situation, the deficit in the total energy relative to the expected photopeak amplitude can be used to determine the

percent signal loss due to WPCT. This is calibrated as a function of overall depth of interaction and the separation distance between the two pixels.

The signal deficit information can then be used to correct the WPCT of each event, as shown in equation 3.12,

$$E(n) = E_{raw}(n) + \sum_{i=1}^{N} E_{raw}(i)C(d(n,i), z(i)) \tag{3.12}$$

where $E(n)$ is the corrected estimate of the energy deposited on pixel n, $E_{raw}(n)$ is the estimated energy before correction, N is the number of pixels that collected charge, and $C(d(n,i), z(i))$ is the percent signal loss due to WPCT for pixels separated by a distance $d(n,i)$ at a depth of $z(i)$. For this equation to hold true, $C(d(n,n), z(n))$ must be defined as zero, such that an interaction does not introduce negative crosstalk on the pixel that collects it.

Dr. Feng Zhang developed this calibration and reconstruction technique prior to performing a rigorous mathematical derivation of the ideal reconstruction process. This was done by Prof. Zhong He in 2008 (36). This work proved that this technique was a good approximation. This paper also caused a re-evaluation of the WPCT correction and lead to the realization that equation 3.12 was not applied correctly. In the previous implementation the crosstalk in pixel n due to pixel i was actually added back to pixel i rather than pixel n. The end result was that the totally energy was correct, but the individual energies were slightly wrong. While this has no impact on the spectroscopy of the device it will, in principle, degrade the accuracy of the image reconstruction.

3.3.3 Using the Cathode Signal to Correct Timing Information

The depth of each interaction for a multiple-interaction event can be determined by the timing information, as discussed in previous sections. However, the CAR still contains information regarding the average depth of interaction, which should be

utilized to minimize depth uncertainty, if possible.

When using drift time to reconstruct the depth of interaction the uncertainty is dominated by the timing pickoff uncertainty, or timing jitter. This timing jitter is a function of the noise on the signal and by the charge induction rate on the preamplifier. A sharply rising signal, as seen on the anode pixels, will have a much smaller absolute timing uncertainty than a slowly rising signal such as the cathode. For this reason the cathode timing information is often the biggest contributor to the depth uncertainty of each interaction in multiple-interaction events. For multiple-pixel events this effect is somewhat offset by the fact that each pixel will only see a fraction of the charge, which will also cause a low charge induction rate in the case of small energy depositions.

The cathode timing information is a major source of depth uncertainty for a multiple-interaction event and the CAR information would otherwise go unused. To correct this situation the depth of interaction calculated by the CAR can be compared to the energy weighted average of the individual depths of interaction from drift time. This average reconstructed depth of interaction will then be shifted based on the CAR information. This process is shown mathematically in equation 3.13, such that

$$z(n) = \frac{R_{CA}}{\sum_{i=1}^{N} \frac{E(i) z_{raw}(i)}{E(i)}} \tag{3.13}$$

$$z(n) = z_{raw}(n) R_{CA} \frac{\sum_{i=1}^{N} E(i)}{\sum_{i=1}^{N} E(i) z_{raw}(i)} \tag{3.14}$$

where R_{CA} is the CAR, $z(n)$ is the depth of interaction in pixel n after correction based on the CAR, $z_{raw}(n)$ is the depth of interaction in pixel n before the correction, N is the total number of pixels that collect charge, and $E(i)$ is the energy deposited on pixel i.

3.3.4 Nonlinearity Calibration

The implementation of a nonlinearity correction on a 3D position sensitive pixelated detector is different in several ways from the nonlinearity correction of a detector with a single readout electrode. One challenge was described earlier when discussing the calibration of the CAR. Furthermore, pixelated devices have a large number of independent readout channels, so the calibration of channel should be automated. Finally, a position sensitive system has the capability to correct the energy deposited on an interaction-by-interaction basis. Without the position sensitivity it is only possible to correct the total energy deposited. An entire chapter of this dissertation will be dedicated to the the full description of how nonlinearity is implemented and evaluated in the system.

CHAPTER IV

Energy Resolution Degradation in Multiple Pixel Events

4.1 Introduction

The energy resolution will always degrade as more pixels collect charge during the detection of a single incident gamma-ray. When the energy resolution of multiple-pixel events is reported it is consistently worse than for single-pixel events (37). This is expected as multiple-pixel events are inherently different than single-pixel events in several fundamental ways such as electronic noise, depth reconstruction, and WPCT. In this chapter the known differences between single-pixel and multiple-pixel events will be described and quantified when possible.

It is important to differentiate between multiple-pixel events and multiple-interaction events. A single-pixel event can contain multiple interactions. In order to occur within one pixel, these interactions are normally very close together and the impact on the spectrum is small. Conversely, it is possible to have a multiple-pixel event caused by a single interaction when a charge cloud is split between two pixels. It is, of course, possible and probable to have an event that involves multiple pixels and multiple interactions. The four primary scenarios are shown schematically in Figure 4.1. One final, and important, scenario to consider is the case where a multiple-pixel event is

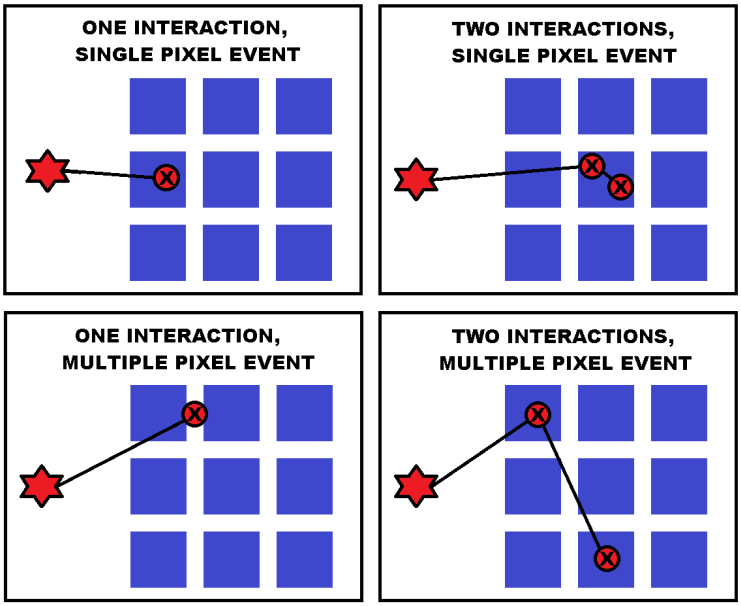

Figure 4.1: Illustration of various event types in the system. The star represents a source of gamma rays, the blue squares represent pixels (in this case the detector only has 9 pixels). The red circles represent gamma interactions.

recorded even though only one pixel collects charge. This is caused by the induction of a transient signal on a pixel that neighbors a true charge collection. The transient is at first positive, then ends negative, as the charge it collected at a point with a weighting potential of zero according to the pixel of interest. The slow shaped signal for this pixel will end negative, but if it has a positive value at any time due to the shaped transient signal, then the peak hold circuit will report this positive value. Thus a pixel that does not actually collect any charge can register a positive signal. This effect becomes much more severe at higher energies and for interactions near the edge of a pixel. The magnitude of this effect is strongly influenced by the true signal threshold, as discussed in 3.1.3.

Another important distinction is between the different types of multiple-pixel events. Two pixel events can be classified into three categories based on separation distance: side neighbor, diagonal neighbor, and non neighbor. Each of these categories is illustrated in Figure 4.2. Each of these categories has radically different behavior.

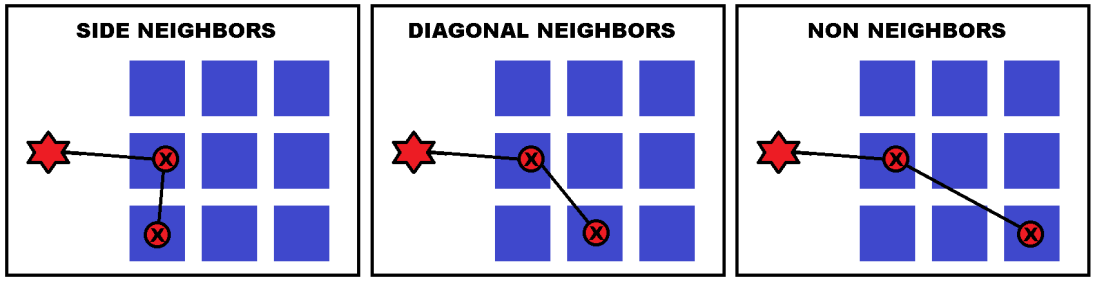

Figure 4.2: Illustration of side-neighbor, diagonal-neighbor, and non-neighbor events in a pixelated device.

Side neighbor events account for more than half of the two pixel events at 662 keV and are challenging to reconstruct because they could contain a single interaction that undergoes charge sharing, an interaction under each pixel, or some combination of the two. Diagonal neighbors are far less common, accounting for less than 10% of the 2-pixel events at 662 keV, but they are important because they have a large WPCT, like side-neighbor events, but they do not include charge sharing events. The last category, non-neighbor events, are the most valuable events for imaging and have the least influence due to weighting potential cross talk. They also consist entirely of multiple-interaction events.

The categories described in this section will be used throughout this chapter to help study the issue of multiple-pixel event energy resolution degradation.

4.2 Summary of Experimental Results on Multiple-Pixel Event Resolution

Table 4.2 presents the energy resolution for an eV Products detector tested with both the GMI and BNL ASICs and a Redlen detector tested with the GMI ASIC. The BNL ASIC is known to have much lower electronic noise, on the order of 2 keV relative to 3 or 4 keV noise in the GMI ASIC, and this is reflected in the improved energy resolution of single-pixel events. The noise is even more important for multiple-pixel

Detector ID Number	4E1	4E1	4R143
Detector Manufacturer	eV Prod.	eV Prod.	Redlen
ASIC Used for Test	GMI 2.3	BNL H3D	GMI 2.3
Test Date	Sept. 2007	Oct. 2009	Aug. 2011
Data Acquired By	(38)	(39)	W. Kaye
1-Pixel Energy Resolution	0.70%	0.52%	0.73%
2-Pixel Energy Resolution	1.11%	0.83%	1.31%
3-Pixel Energy Resolution	1.93%	1.07%	1.71%
4-Pixel Energy Resolution	2.83%	1.42%	2.17%

Table 4.1: Energy resolution for three different experiments with analog ASICs coupled to CdZnTe detectors

events and the performance gap between the BNL ASIC and the GMI ASIC becomes more evident.

There are additional factors beyond the electronic noise. Comparing the GMI data for detector 4E1 to the data for detector 4R143 we can see that 4E1 does better for 2-pixel events while 4R143 does better for 3- and 4-pixel events. The 3- and 4-pixel events are explained by the lack of a critical multiple-pixel event correction, that will be discussed in Chapter VII, that had not yet been developed when 4E1 was tested with the GMI ASIC. The 2-pixel events are better for 4E1 because the impact from the Chapter VII correction is small for these events while 4R143 has grid fabrication issues that will be discussed in Section 4.3.

Section 4.6 will show that the performance in both the BNL ASIC and the GMI ASIC can be explained entirely based on our limited understanding of the electronic noise. However, table 4.2 shows that even two very good detector connected to the same ASIC can have very significant differences in the performance of multiple-pixel events. This chapter will address the factors that must be considered when studying the variation of multiple-pixel event resolution between detectors or ASICs.

4.3 Charge Loss to Grid

If a charge cloud is shared between two side-neighbor pixels then some fraction of that cloud must be located directly above the grid. In order to fully collect the electrons they must be steered away from the grid and into the pixels. If this process is not done completely within the shaping time than a signal deficit can arise for side-neighbor interactions. This deficit will depend on the orientation of the cloud relative to the grid, so it will manifest itself in the form of a broader photopeak.

It is possible to measure this effect. First, consider the WPCT correction described in section 3.3.2. We expect that for most events there will be a significant contribution from WPCT, with the exception of cathode side events, as the initial weighting potential is zero. The spectrum of cathode side events can be compared between side-neighbor and non-neighbor events. If the grid steering is near perfect than the non-neighbor and side-neighbor photopeak centroids should be at the same amplitude, while a smaller amplitude in the side-neighbor data indicates an inadequate steering effect.

To illustrate the quality of the steering grid, Figure 4.3 shows the photopeak centroid as a function of depth for 2-pixel photopeak events in detector 4R143 where both interactions occur at approximately the same depth. Data is shown separately for non-neighbor events, side-neighbor events with 80V on the grid, and side-neighbor events with 60V on the grid. When the grid voltage is insufficient the photopeak centroid of side-neighbor events is lower than the non-neighbor events, but when the grid voltage is increased their centroids are aligned. The impact can be observed by comparing the energy resolutions. With 60V on the grid the side-neighbor events acheived 1.67% energy resolution at 662 keV, which improved to 1.28% when the grid voltage was increased to 80V.

This does not definitively prove that there is no impact on energy resolution degradation from insufficient grid steering. Although we can see the amplitudes match on

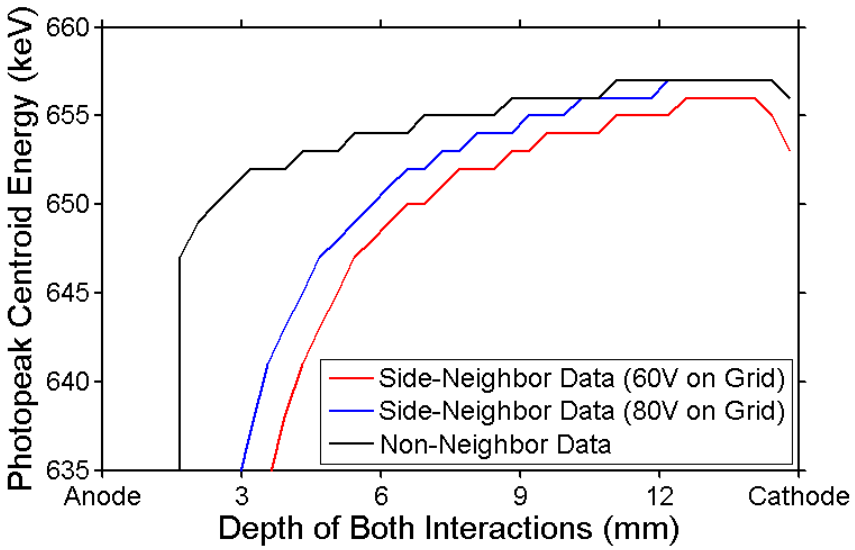

Figure 4.3: Photopeak centroid as a function of depth for 2-pixel photopeak events where both interactions occur at approximately the same depth.

the cathode side, that represents the behavior of all pixels combined. There could still be some pixels that have not yet reached complete saturation. To illustrate this point, the side-neighbor event energy resolution is shown for each pixel for detector 4R143 at 80V in Figure 4.4. A significant variation in the energy resolution is observed, which indicates a variation on a pixel-by-pixel basis in the effectiveness of the steering grid.

Incomplete grid steering on a pixel-by-pixel basis is prevalent in CdZnTe. When the same test was repeated on other detectors it was found that some pixels could not produce a photopeak at all between side neighbor events, even though the overall spectrum indicates optimal grid steering. This is a major factor that degrades the energy resolution of side-neighbor events.

4.4 Weighting Potential Crosstalk

Section 3.3.2 introduced the concept of WPCT. This phenomenon occurs only for multiple-interaction events, therefore, it is a prime suspect in the degradation of

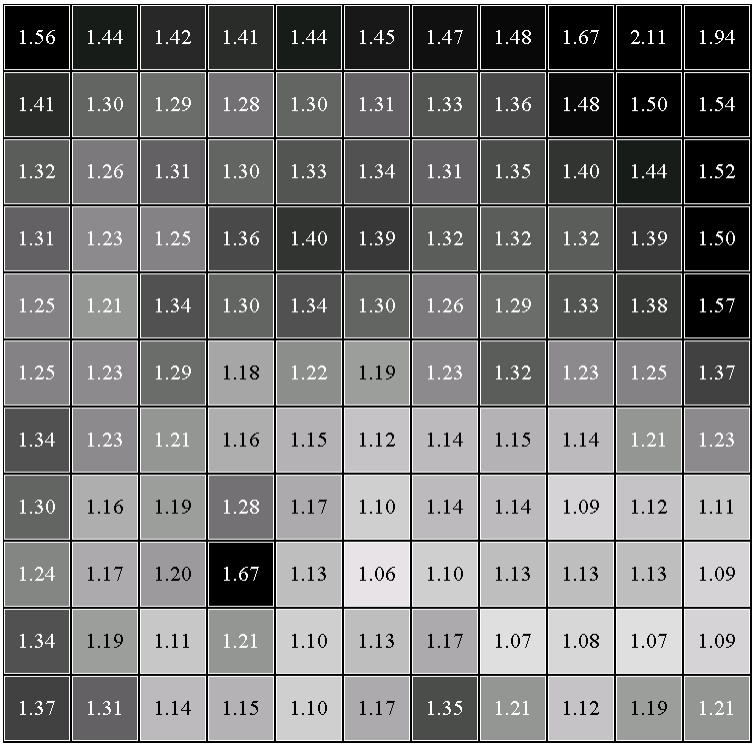

Figure 4.4: The side neighbor event resolution of each pixel in detector 4R143. The grid is operated at 80V, but there is still a significant variation in the energy resolution of each pixel. This energy resolution degradation is not correlated with the single pixel performance, thus, insufficient grid steering is likely responsible.

the energy resolution of multiple-pixel events. A correction algorithm is available, but the cross talk will vary on a scale finer than the pixel pitch, which is the spatial resolution limit for two of the three dimensions using an analog ASIC. This means that the algorithm is not capable of correcting the subpixel variation in the WPCT. This effect should be much greater for interactions that occur in two nearby pixels rather than two distant pixels.

In order to understand the impact of this WPCT, the two pixel event energy resolution is plotted as a function of separation distance between pixels in Figure 4.5. The worst energy resolution among 2-pixel events is observed in the side-neighbor events. This may not necessarily be due to WPCT, as a large fraction of these events are charge sharing. It is better to compare the difference between diagonal neighbors and distant non neighbors. We observe that diagonal neighbors and the closest non neighbors achieve energy resolution around 1.28%, while the distant non neighbors average out around 1.20%. This indicates that the impact of WPCT is small on non neighbor events after the correction has been applied.

The reader may note the asymmetric behavior of charge sharing events in Figure 4.5, in the sense that interactions involving the side neighbor on the left or right performs measurably better than those that involve the side neighbor that is above or below. This phenomenon is dominated by the behavior of the edge pixels; as the edge pixels on the top and bottom each have two neighbors on the left or right but only one neighbor above or below and the opposite is true for edge pixels on the left and the right. Therefore, the row of good pixels along the bottom in Figure 4.4 does more good for the left-right side neighbors than for the up-down side neighbors.

Another important limitation of the WPCT calibration, described in Section 3.3.2, is that the depth separation is not considered. Ideally the depth separation should not effect the WPCT, it should only depend on the absolute depth of each interaction. However, there are some cases where this could be problematic, for example, if the

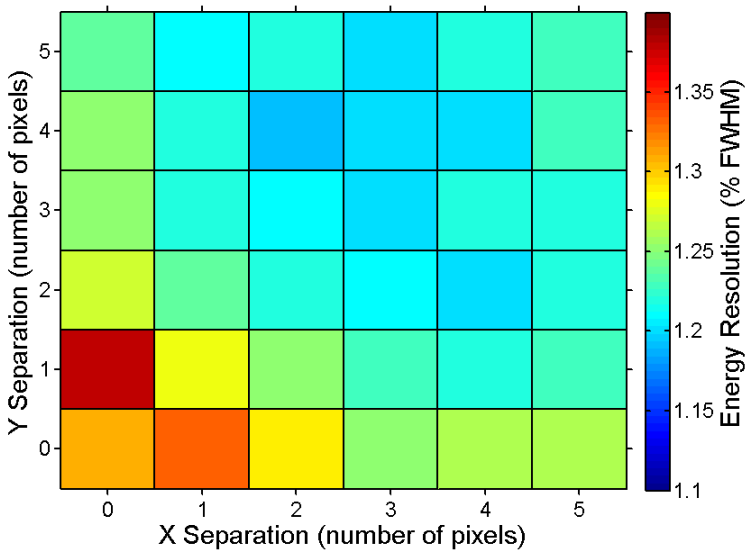

Figure 4.5: Each square represents a different separation distance between pixels and is colored based on energy resolution for those events. (0,1) and (1,0) are side neighbors, (1,1) represents diagonal neighbors, (0,0) is the data from all events combined, and everything else represents varying separation distances for non-neighbor events. Symmetry is expected about a diagonal line from (0,0) to (5,5).

shaping time was shorter than the maximum possible drift time. In this case the WPCT would be reduced for events with a large separation distance. To study this effect the energy resolution and photopeak position data were generated as a function of depth separation. The results from detector 4R167, in Figure 4.6, show that as long as a sufficiently large value of hold delay time is used there is no degradation in the event reconstruction for large separation distances. If the hold delay time is too short then a depth dependent nonlinearity is introduced to the system, which will be described in Chapter VII and Chapter VIII.

4.5 Depth Reconstruction

The depth reconstruction of multiple-interaction events, be based on the drift time, differs from the depth reconstruction of single-pixel events, based on the CAR. The drift time reconstruction will be subject to TAW and potentially WPCT. For

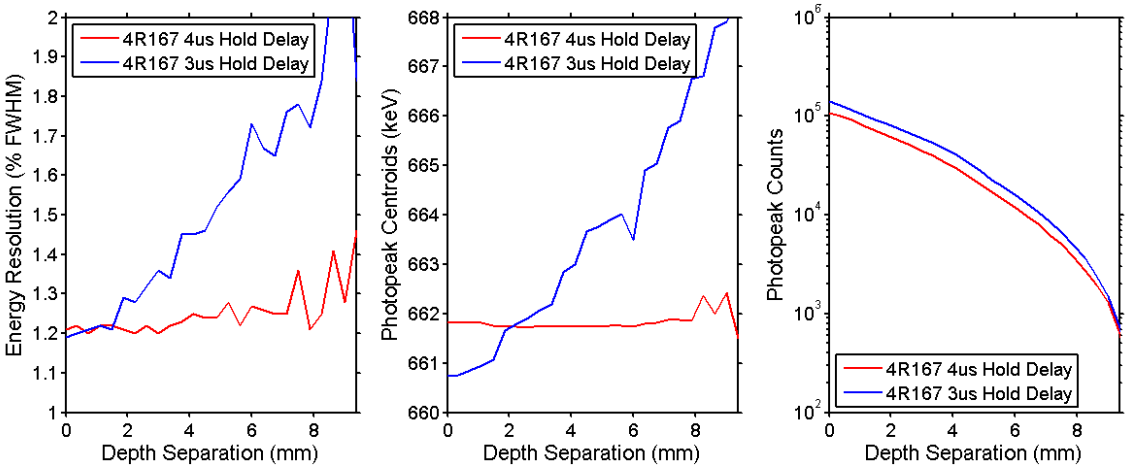

Figure 4.6: Energy resolution (left), photopeak position (middle), and number of counts(right) as a function of separation distance between the depth of interactions for multiple-pixel non-neighbor events for two different hold delay times. When the hold delay time is too short events with a significant depth separation cannot be properly reconstructed.

these reasons it is possible that the depth uncertainty will play an important role in the energy resolution of multiple-pixel events.

The depth reconstruction factor is similar to grid steering in the sense that, while major issues are observed in some detectors, it is possible to identify detectors that have only a small impact from depth reconstruction. To justify that point, consider Equation 3.8 in Section 3.2.1. Measured depth reconstruction data, shown in later chapters, indicates that a depth resolution of 1 mm for multiple-pixel events is expected from the GMI ASIC.

The impact of depth reconstruction on the energy resolution depends on both the uncertainty in the reconstructed depth and the magnitude of the photopeak shift as a function of depth. There are detectors with almost no trapping, such that the photopeak centroid moves less than 0.5% throughout three quarters of the bulk. The spectrum at each depth for a representative pixel from such a detector, 4R143, is shown in Figure 4.7. If this detector can achieve 1mm depth resolution, then Equation 3.8 would predict an energy resolution of 0.05% if depth reconstruction

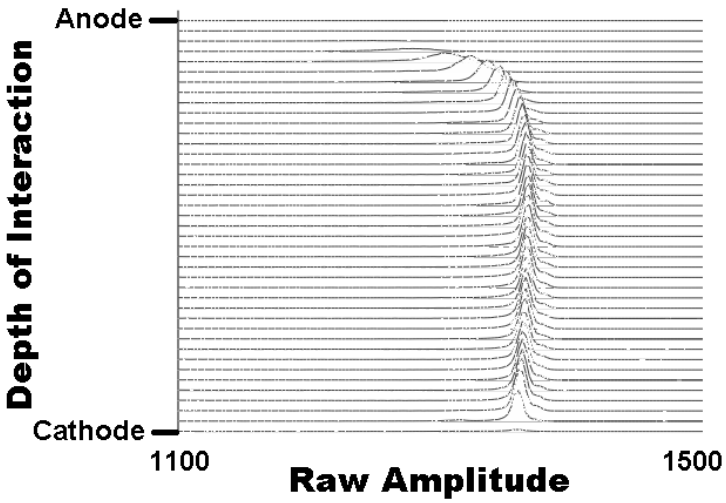

Figure 4.7: The spectrum at each depth from one pixel of detector 4R143. The change in signal amplitude is very small with respect to depth, except in the region of the detector near the anode surface.

is the only factor considered. For these scenarios, even if either trapping or depth uncertainty were doubled or tripled, the impact of depth reconstruction on multiple-pixel events will be small. Furthermore, the depth resolution of multiple-pixel events is not significantly different from single-pixel events, based on collimator experiments presented in the following chapters.

There are some circumstances where depth reconstruction will degrade energy resolution for multiple-pixel events. This is expected if the trapping is non-negligible and the depth reconstruction from drift time is much worse than for CAR. This scenario is observed occasionally in detectors from Redlen when a unique relationship does not exist between drift time and CAR. This implies that events at the same depth have different drift times, which could be caused by subpixel variation in the drift velocity. Regardless of the cause, the result is that there is no longer a unique relationship between drift time and depth and the depth reconstruction of multiple-pixel events will be significantly degraded. This makes the trapping in the detector uncorrectable for multiple-pixel events and degrades their energy resolution. This behavior is unusual and has only been observed for a few detectors in a shipment of

more than 100 CdZnTe detectors from Redlen Technologies.

4.6 Noise

When a signal is recorded from multiple pixels we expect a greater contribution from electronic noise to the overall signal uncertainty. Assuming that the magnitude of noise on each pixel is the same, the noise on each pixel is independent, and the noise can be described by a Gaussian distribution, then we expect the noise contribution to add in quadrature sum as shown in equation 4.2,

$$(\sigma_{E,noise})_{total} = \sqrt{(\sigma_{E,noise})^2_{pixel1} + (\sigma_{E,noise})^2_{pixel2} + ... + (\sigma_{E,noise})^2_{pixelN}} \tag{4.1}$$

$$(\sigma_{E,noise})_{total} = \sqrt{N}\,(\sigma_{E,noise})_{eachpixel} \tag{4.2}$$

where $(\sigma_{E,noise})_{total}$ is the overall uncertainty due to electronic noise and $(\sigma_{E,noise})_{pixelN}$ is the noise contribution due to pixel N.

Correlation between the noise values on each pixel is an important factor that determines the energy resolution of multiple-pixel events. First, imagine the case when two pixels are perfectly correlated. In this case the noise must be summed directly, rather than in quadrature, as doubling the number of fully correlated pixels used to calculate an amplitude value will directly double the noise. In this case, the performance of the system will be significantly worse than for a system without noise correlation, which is summarized in Figure 4.8.

Some degree of positive correlation is expected, as the preamplifiers are in close physical proximity and share a common ground and power line. It is difficult to measure the noise correlation because we cannot get two completely independent and known signals injected into two pixels. If test pulses are used there would have to be

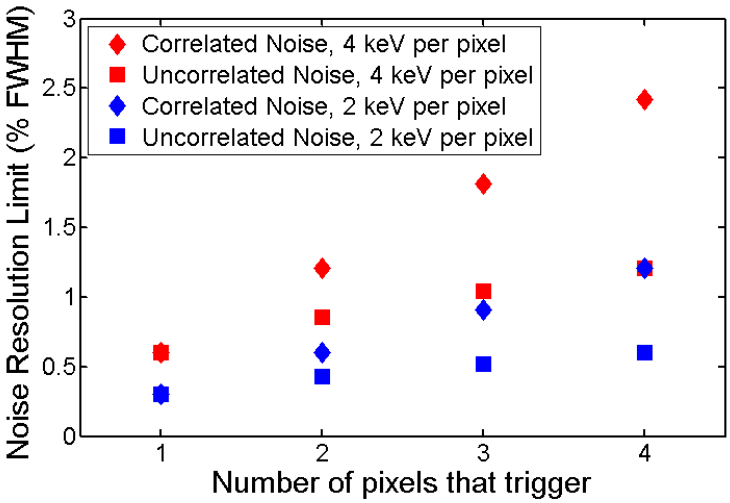

Figure 4.8: The limit on energy resolution at 662 keV due to noise as a function of the number of pixels that read out for an event. Squares represent the noise behavior if each pixel is completely independent and diamonds represent the behavior if they are completely correlated. Red datapoints are for a system noise of 4 keV, which is close to the GMI ASIC system, and blue datapoints are for a system noise of 2 keV, which is close to the BNL ASIC system.

assurance that they are completely independent and not contributing to noise, even through ground connections. Another technique is to monitor the relative baseline positions of each non-collecting pixel during an event. While this is the best tool currently available, there is still a significant disconnect between the fluctuation in the baseline value and the true noise of the system, due to effects such as peak hold. For now, a bound is placed on the contribution between the two extreme behaviors of perfect correlation and no correlation.

If the GMI ASIC is assumed to operate with a noise level of 4 keV and the BNL ASIC operates with 2 keV noise then all the data presented in 4.2 falls within the range of possible multiple-pixel event resolutions shown in 4.8. Therefore, to better understand whether or not the theoretical limit of energy resolution has been reached for multiple-pixel events a more thorough understanding of the noise correlation between pixels is necessary.

4.7 Nonlinearity

The impact of nonlinearity in the reconstructed energy of each pixel for multiple-pixel events can be studied by calculating the photopeak centroid as a function of the energy deposited on one of the pixels for photopeak two-pixel events. Ideally the centroids would align at the calibration energy independent of the energy on each pixel, indicating that there is no observable nonlinearity. If the nonlinearity is systematic then we should be able to observe it even if we combine events from all pixels. The scenarios of events with a separation distance of exactly twice the pixel pitch (the pixels have the same y position and an x offset of two pixels or the same x position and a y offset of two pixels) and side-neighbor events are considered separately and shown in 4.9 along with the counts in each energy bin.

Starting with the side-neighbor events, we see that the majority of the energy bins are well populated with counts, which is expected because charge sharing can manifest itself with all possible combination of energies. The centroids fluctuate by a couple keV with an overall standard deviation, weighted by the counts in each bin, of 0.46 keV. If we convert this to a FWHM assuming it manifests itself as a gaussian blur, than we expect to see a delta function broaden to 1.1 keV FWHM due to this effect. This is a significant improvement over the behavior before nonlinearity correction, which produced an uncertainty of 3.31 keV FWHM for these events.

The dataset for a separation distance of two pixels has very few counts below 200 keV or above 450 keV. This is because these events must be Compton scatters and the energies are restricted by Compton kinetics given the source-detector geometry. In this measurement the source is placed on the cathode side, making it very unlikely that a forward-scattered event could travel a lateral distance of two pixels. Between 200 keV and 450 keV the trend is very similar to the side-neighbor events. This indicates that the side neighbor behavior was due to nonlinearity rather than to charge sharing effects such as WPCT as a function of collection fraction by each pixel. The standard

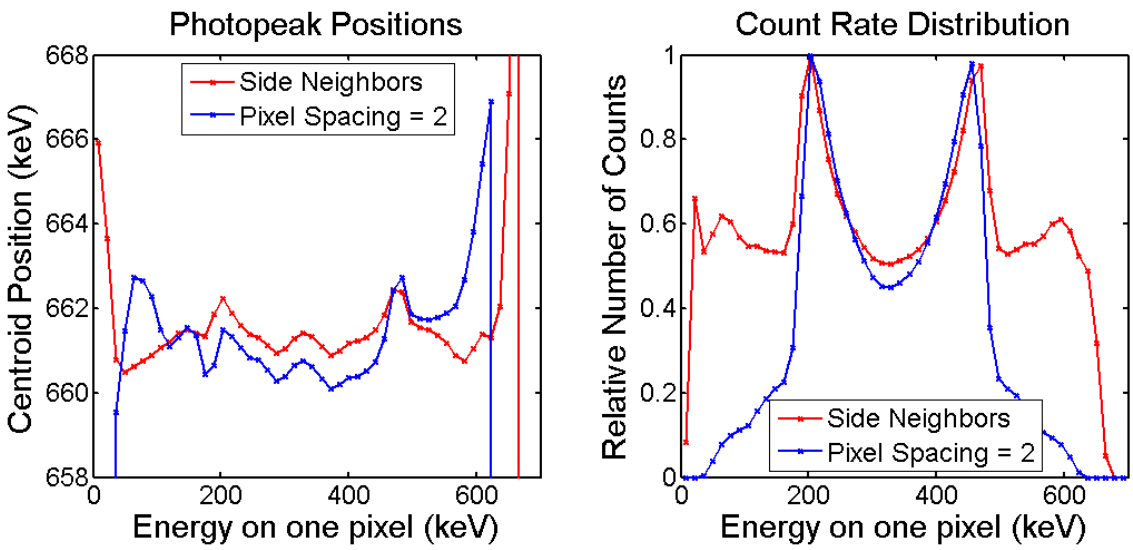

Figure 4.9: On the left is the centroid position of two pixel photopeak events as a function of energy deposited in one of the pixels. On the right is the relative number of counts in each energy bin. Data are shown for side-neighbor events and for events that take place with a neighbor pixel that is separated vertically or horizontally by two pixel pitches.

deviation is 0.75 keV, or 1.76 keV FWHM in this case, slightly worse than the 1.21 keV FWHM measured before nonlinearity correction.

The trend in the overall data indicates the problem is not a major factor in the energy resolution of multiple-pixel events. However, this does not show the complete picture, as it is possible that many pixels have problems due to the nonlinearity correction that get averaged out in the combined data. In this case we want to study events between two specific pixels. Side-neighbor events are useful because there are many counts, but discrepancies could be due to problems with grid steering, as demonstrated in Section 4.3, rather than nonlinearity. The data between pixels with a separation distance of two pixels is ideal for the study, but to get statistically significant counts between two particular pixels requires a long measurement time. A week long dataset taken with 4R143 has sufficient statistical strength to study this problem.

The results are shown for events between each pixel and its rightmost neighbor in

Figure 4.10. Results for events between each pixel and its neighbor two pixels away on the right is shown in Figure 4.11. Both datasets show the majority of pixels closely follow the trends of the overall data. There are only a handful of pixels that have an issue with nonlinearity. They are usually observed in pairs, as one bad pixel will disrupt its own data and the data of its left neighbor in these figures. Also, pixels that have issues in the side-neighbor data also tend to show the same problem in the data for a separation distance of two. This indicates the problem is likely due to nonlinearity and not grid steering.

Overall, the impact of the nonlinearity is relatively small for two-pixel events. The factor of 1.76 keV for non-neighbor events has little influence when added in quadrature sum to the overall photopeak width, which is greater than 8 keV. However, these results should be treated with caution, as the deviation in the photopeak centroid is more extreme at lower energies. If we consider three- or four-pixel events those energies are more likely to get sampled and contribute to the peak broadening.

All of the results presented in this section have been based on measurement data taken with the GMI ASIC. If we examine data from BNL ASIC we see that the impact of nonlinearity on multiple-pixel event energy resolution is even smaller due to a more linear response from this ASIC, which is shown experimentally in section 8.4. This point is illustrated by Figure 4.12, which shows centroid position as a function of energy for events separated by a distance of two pixel pitches for data from both the GMI and BNL ASIC. The uncertainty is 0.57 keV for the BNL data without any nonlinearity correction applied, less than half the result from the GMI data. This result is expected, as the energy resolution using the BNL ASIC does not show the same improvement after nonlinearity correction as the GMI ASIC.

Figure 4.10: These are the same data shown in 4.9, except they are broken into the relationship between each pair of pixels. Data are shown for events between each pixel and its side neighbor on the right side.

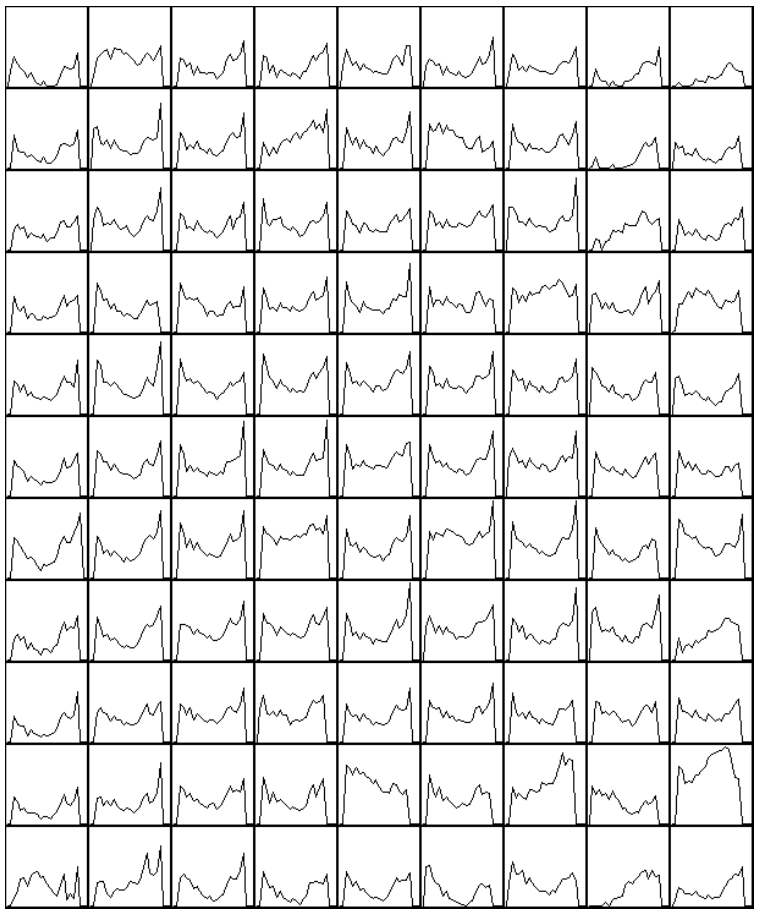

Figure 4.11: These are the same data shown in 4.9, except they are broken into the relationship between each pair of pixels. Data are shown for events between each pixel and its neighbor exactly two pixels away on the right side.

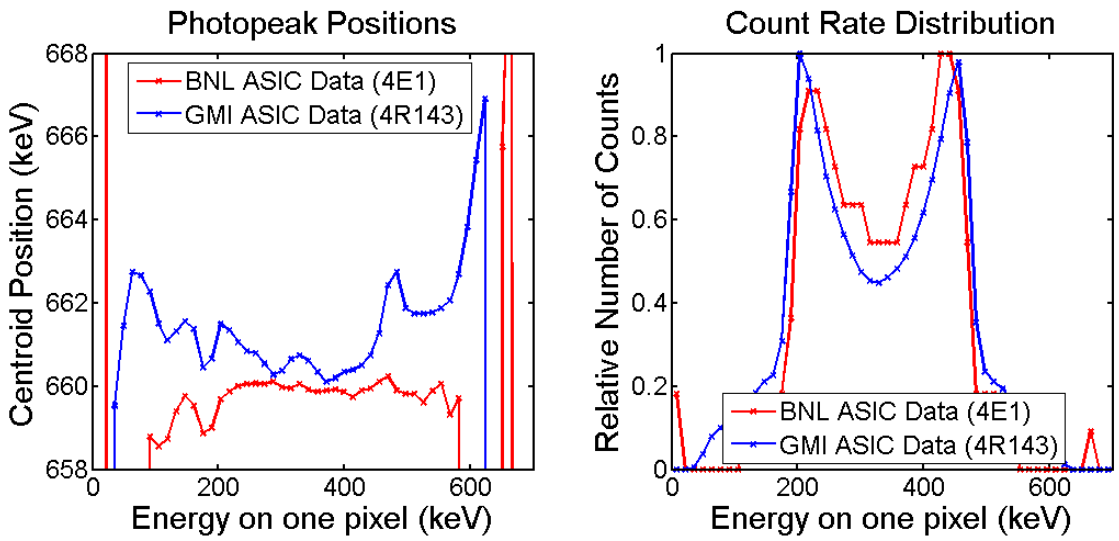

Figure 4.12: On the left is the photopeak centroid position of two pixel photopeak events as a function of energy deposited in one of the pixels. On the right is the relative number of counts in each energy bin. Data are shown for events with a separation distance of two and for events that take place with a neighbor pixel that is separated vertically or horizontally by two pixel pitches. All data are shown without applying a nonlinearity correction.

4.8 Charge Collection Variation due to Multiple Interaction Locations

A single-interaction event generates an electron cloud that is confined to one region of the material while a multiple-interaction event will depend on the response of multiple regions of the material. There is a difference between the two scenarios and it may play a role in the degradation of multiple-interaction events. However, the effect is challenging to quantify or measure.

There are two important considerations for multiple-interaction events: the electron cloud area is not confined to a single region and the total area of the electron cloud will also change. The initial electron cloud diameter increases more rapidly at higher energies, thus if the energy deposited is reduced by a factor of two the cloud diameter will be reduced by a factor greater than two. This would indicate that the total cloud area should be smaller for multiple-interaction events. However, each of the electron clouds will undergo diffusion as they drift through the bulk. Thus, determining which scenario has a greater total cloud area will vary on a case-by-case basis.

4.8.1 Sampling Multiple Material Regions

Focusing on the impact of spatially separated electron clouds, it is important to consider the response of each pixel. CdZnTe is known to have a larger number of small point defects such as tellurium inclusions (40). With an analog ASIC the correction parameters are based on the average behavior of the pixels. A large electron cloud contained within a single pixel will sample a large fraction of the pixel area and thus the response should look similar to the calibrated behavior. Smaller electron clouds will sample smaller fractions of the pixel and will be more subject to sub-pixel fluctuations in response. This effect is balanced by the fact that multiple-pixel events

sample more pixels which may reduce these fluctuations.

4.8.2 Sampling Different Material Regions

Photopeak single-pixel events cannot occur near the edge of the pixel as they will either lose charge to the gap and fall out of the photopeak or some charge will be collected by a neighbor resulting in a multiple-pixel event. At 662 keV, single-pixel events only occur in about 75% of the pixel area, assuming events cannot occur within 125 μm of the edge of the pixel. The other 25% of the pixel area will generate side-neighbor photopeak events or events in the photopeak tail if they do not pass sufficient charge to the side neighbor.

The side-neighbor events occur in a region of the material that is never calibrated. Instead, the gain is corrected using information from the pixels on each side of the grid. Thus, the gain correction parameters are expected to provide more benefit to the single-pixel events than to the multiple-pixel events on average. This argument holds true for multiple-interaction events without charge sharing as well, as the electron clouds are smaller and less likely to trigger a side-neighbor pixel when they occur near the edge of a pixel.

4.8.3 Charge Loss to Side Neighbor Events

If a small amount of charge is shared with a neighboring pixel it is difficult to reconstruct correctly, as discussed in section 3.1.3. Whether or not this is more of a problem for multiple-pixel events depends on the cloud size and diffusion in the material. If there are a large number of interactions then degradation from this factor is likely, as all the clouds will diffuse and there is a much greater chance that one of them will be near a grid.

This problem should also be considered from the perspective of cloud density. Low energy charge clouds are especially problematic because they can expand beyond 100

μm due to diffusion which results in a low electron density in the cloud. If a 662 keV cloud shares even 5% of its area with a neighbor then it then neighbor pixel will likely trigger, but a 60 keV cloud can lose a third of its area to a neighbor without triggering the GMI ASIC. Thus, low density clouds, present only in the multiple-pixel events of the photopeak, are more likely to lose charge to a side neighbor without triggering.

4.8.4 Multiple Samples of a Non-Gaussian Distribution

Another way to look at this problem is to think about the shape of the photopeak distribution. In CdZnTe it is very common to see a low energy tail on the photopeak; the region between the peak and the Compton edge is roughly 30% of the photopeak area in an eighteen detector array used throughout this dissertation. These events below the photopeak induce significantly less charge than expected. For single-pixel events these appear in the tail of the photopeak and have no effect on the FWHM. However, for multiple-pixel events this will probably only happen to one of the two interactions, with a higher overall probability than for a single-pixel event. If it happens to a relatively small energy deposition then it may not end up in the tail, as the charge loss will be quite small. Instead, it will be closer to the peak and more likely to degrade the FWHM.

For any event there is a chance that it has some charge collection problem. Based on the previous discussion, it is not clear if the multiple clouds of a multiple-interaction event are more likely to have a problem than a larger single interaction cloud. Nevertheless, when the problem occurs for multiple-pixel events it is more likely to contribute to the FWHM.

4.9 Summary

Understanding the degradation of multiple-pixel events requires the analysis of many possible factors, which must be carefully considered on a system-by-system and detector-by-detector basis. Factors such as grid steering, depth reconstruction, and charge collection variation will depend strongly on the quality of the detector. Factors such as nonlinearity and noise are highly dependent on the readout electronics. WPCT variation will be the same for all analog ASICs and all detectors with the same geometry, as it depends exclusively on electrode configuration. When the final energy resolution values are examined, they can be explained entirely by the bounds of the electronic noise.

CHAPTER V

Depth Reconstruction Using Signal Ratios

5.1 Introduction

The correct determination of the interaction positions within the detector material is the key to the excellent spectroscopic and imaging capability of pixelated semiconductors. Two dimensions of an interaction position are provided by the physcial location of the pixel that collects charge. Without a technique for sub-pixel position determination, position uncertainty in these two dimensions is limited by the pixel pitch. The ASICs used in this work are based on relatively simple sample-hold and timing pickoff circuits that do not allow for sub-pixel position resolution.

The next two chapters will focus on the determination of the third dimension of position sensitivity, which will be referred to as the interaction depth. A collimation system is used to study and validate the depth reconstruction. This chapter will focus on reconstructing the depth of interaction based solely on the ratio of the cathode to the anode signal (CAR). While this technique works only for single interaction events, it is used in the calibration of all events, as it is the least sensitive to the internal electric field of the device. The following chapter will discuss the drift time technique for depth reconstruction which is applied to multiple-interaction events.

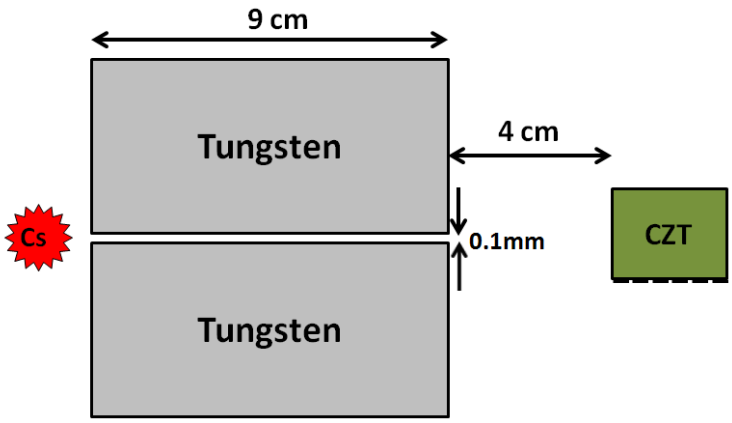

Figure 5.1: Collimator geometry used for depth reconstruction validation experiments.

5.2 Experimental Technique for Depth Reconstruction Verification

The ideal instrument for studying depth reconstruction in pixelated devices is a beam of gamma-rays that irradiates a single depth in all pixels of the detector. This can be achieved by collimating a source with two attenuating slabs with a narrow spacing between them, as shown in Fig. 5.1.

The beam width should be much smaller than the depth uncertainty of the device, in which case the uncertainty in the reconstructed depth distribution will be a measure of the depth resolution of the system. Ideally, the position of the beam relative to the detector would be known such that the reconstructed depth can be compared to the true depth. This is discussed in section 5.4.

5.3 Experimental Determination of Depth Uncertainty

5.3.1 Overall Depth Uncertainty

A collimated beam is used to study the depth resolution of many pixelated semiconductor detectors, including various sizes and anode configurations of CdZnTe as well as HgI_2 devices. The depth resolution is consistently better than 1 mm FWHM

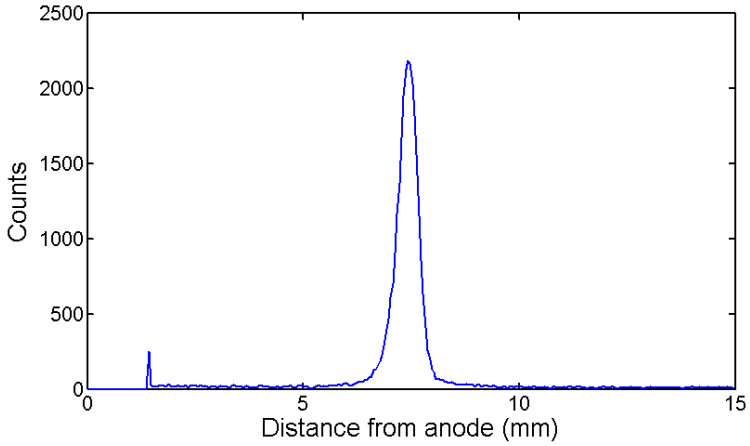

Figure 5.2: Depth spectrum of 662 keV photopeak events in detector 4E3 using the BNL ASIC. A collimated fan-beam irradiates the central depths of the detector.

for a collimated beam of 662 keV gamma-rays. This statement does not hold true for detectors with large fluctuations in the cathode signal. These fluctuations must be on the same order of magnitude as the gamma-ray signal and must occur with a period similar to the shaping time in order to degrade the depth resolution. Depth resolution of 0.5mm is shown in 5.2, using an excellent detector from eV Products and the BNL ASIC. Depth resolution of roughly 0.7mm is shown in Figure 5.3for a good Redlen detector connected to the GMI ASIC.

An interesting feature of both depth distributions presented is that they are asymmetric with a tail favoring depths near the anode, which is most pronounced in Figure 5.3. In order to study the nature of this tail, the depth distribution is plotted independently for each pixel, as shown in Figure 5.4 for the BNL ASIC data and Figure 5.5 for the GMI ASIC data. The overall depth resolution is limited by the misalignment of the depth distribution between pixels, especially in the case of the detector coupled to the GMI ASIC. Ideally this would be due to something as simple as failing to properly determine the baseline offset and gain of each channel, resulting in inconsistent calculation of the CAR. However, the alignment is the worst in the central region, and quite good near the anode and cathode, so it would, at the least,

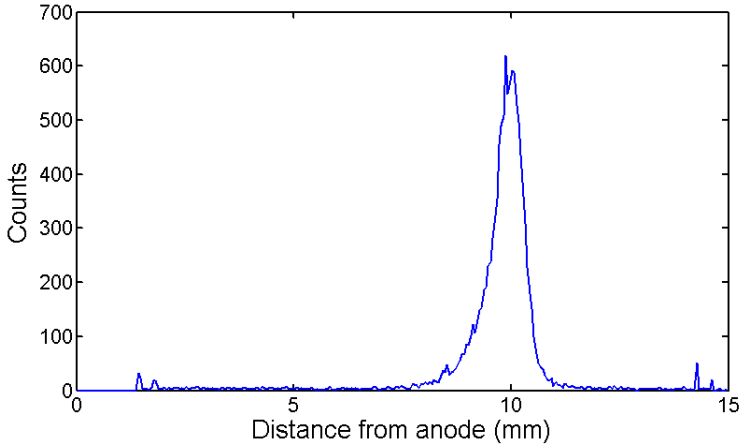

Figure 5.3: Depth spectrum of 662 keV photopeak events in detector 4R60 using the GMI ASIC. A collimated fan-beam irradiates a depth 5mm from the cathode surface.

require a nonlinear behavior in the CAR reconstruction. The next section addresses one possible cause of the misalignment.

5.3.2 Depth Reconstruction Near the Side Surfaces

The fact that the depth of interaction distributions do not align well for all pixels is an important observation because, if uncorrectable, it puts a limit on the depth resolution of the system. If it is related to the nonlinearity or inaccurate gain and offset determination for each pixel then it should have no spatial dependence within the device. However, if a plot is made showing the depth centroid calculated for each pixel a pattern can be observed, as shown in figures 5.6 for the BNL ASIC data and 5.7 for the GMI ASIC data. Both detectors show a bias toward lower centroid values near the bottom left corner, which is in close proximity to some signal wires that run along the side of the detector. The Redlen detector shows a significant deficit near one side, which happened to be 2 mm away from another CdZnTe detector at the time of the experiment. The eV Products detector has one side with consistently smaller centroid values, although the effect is much less pronounced. This behavior is not observed near the cathode side. The CAR shows a nonlinear relationship with

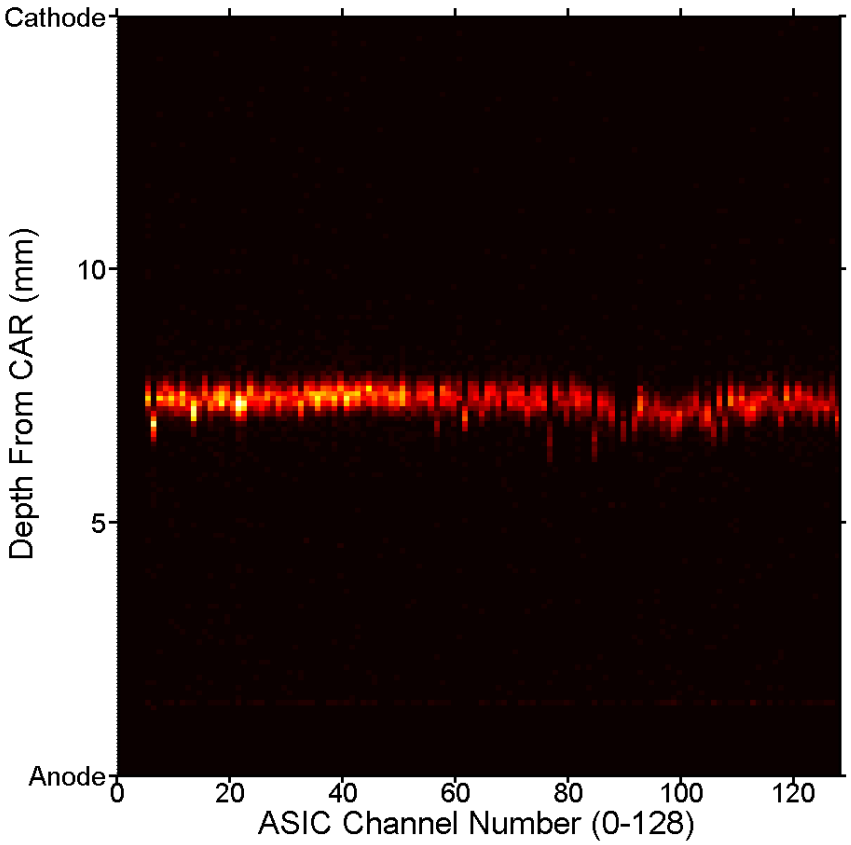

Figure 5.4: Depth spectrum of 662 keV photopeak events in each pixel of detector 4E3 using the BNL ASIC. A collimated fan-beam irradiates the central depths of the detector. Each channel represents a different pixel position.

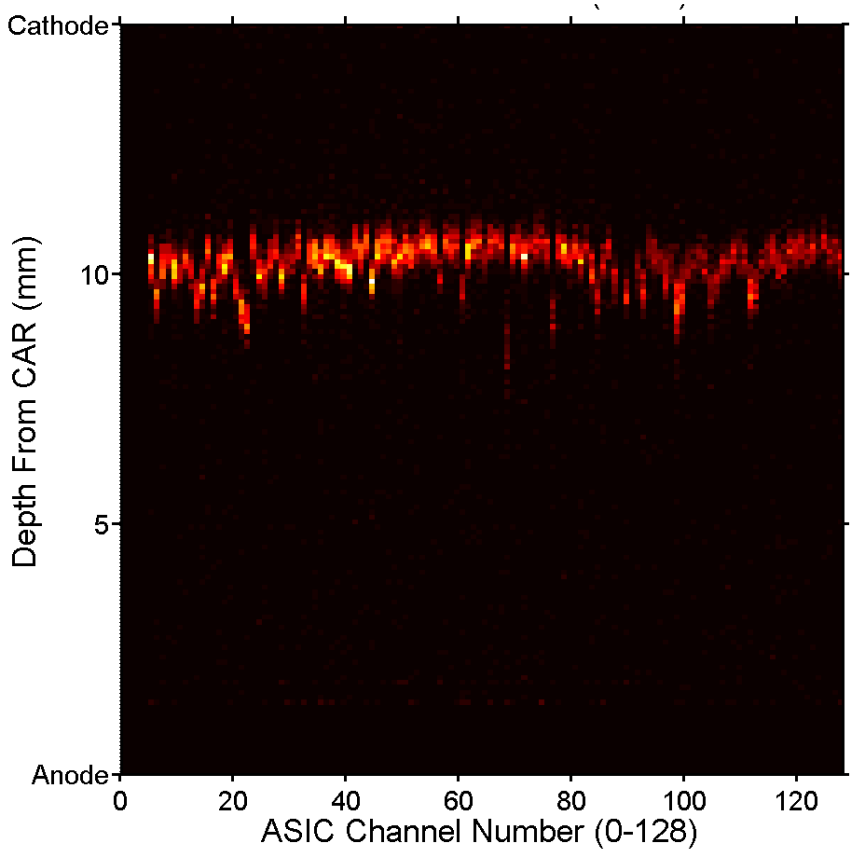

Figure 5.5: Depth spectrum of 662 keV photopeak events in each pixel of detector 4R60 using the GMI ASIC. A collimated fan-beam irradiates a depth 5mm from the cathode surface. Each channel represents a different pixel position.

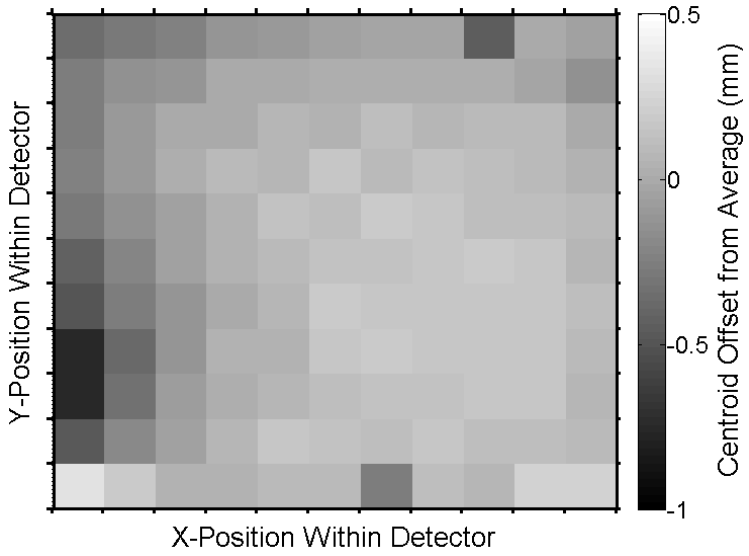

Figure 5.6: Centroid of the depth of interaction distribution for 662 keV photopeak events in each pixel of detector 4E3 using the BNL ASIC. A collimated fan-beam irradiates the depths approximately 8cm from the cathode surface of the detector. Each square represents a pixel.

depth that changes as a function of position within the device.

This effect could be explained by a nonlinear weighting potential on the cathode. In order to test this hypothesis we can turn to collimated data taken for each nine detector plane of an eighteen detector array. The cathode of the central detectors should have some amount of small-pixel effect behavior occurring near the edges, as the cathodes of neighboring detectors will play a small role in the weighting potential distribution. If there is no neighboring detector on a particular side then this small pixel effect should not be seen.

A collimated beam is injected into each plane of the eighteen detector array. The depth centroid of each row and each column of pixels is calculated relative to the overall depth centroid for each detector. In this way the centroid distribution along the x-axis or y-axis can be calculated for each detector. There are only three possible cases: a detector with a neighbor on both sides, a detector with a neighbor only on the left side, or a detector with a neighbor only on the right side. For each case, in each dimension, there are six detectors that should show the same behavior. The

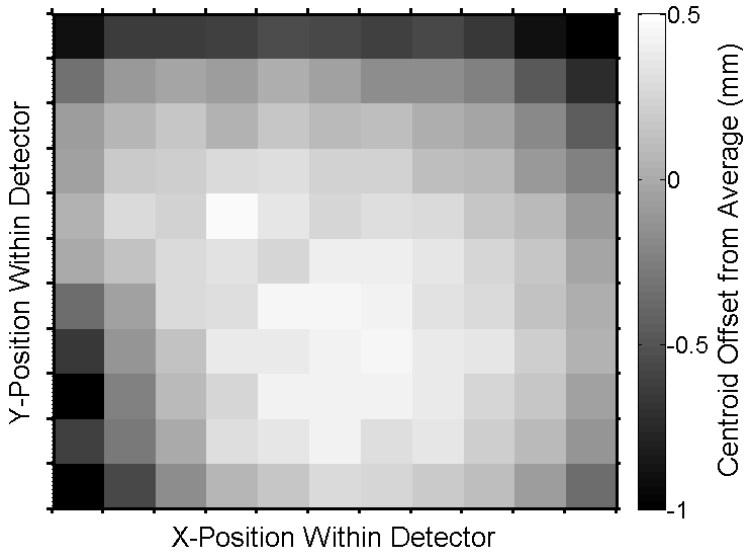

Figure 5.7: Centroid of the depth of interaction distribution for 662 keV photopeak events in each pixel of detector 4R60 using the GMI ASIC. A collimated fan-beam irradiates a depth 5mm from the cathode surface. Each square represents a pixel.

behavior of these detectors is averaged and shown in Figure 5.8. If a neighbor detector is present then the centroid on the edge of the detector is significantly lower than if no detector is present. The depth centroid is systematically larger in the center of the detector. For detectors with one neighboring detector the maximum depth centroid is biased away from that neighboring detector.

This effect would be challenging to correct, requiring, at the least, precise knowledge of the exact geometry and orientation of each detector relative to its neighbors. Furthermore, it is not easy to model. The weighting potential for one plane of the eighteen detector array, nine detectors in a three-by-three array, is simulated in Maxwell. Due to the air gap between the crystals the impact of the neighboring cathodes on the weighting potential is small. For now, this effect places a fundamental limit on the depth resolution of our array system, with a 0.7 mm spread in average depth of interaction between the center of the detector and the edge. In principle, larger gaps between detectors could be used to mitigate this effect, at the cost of intermodule efficiency.

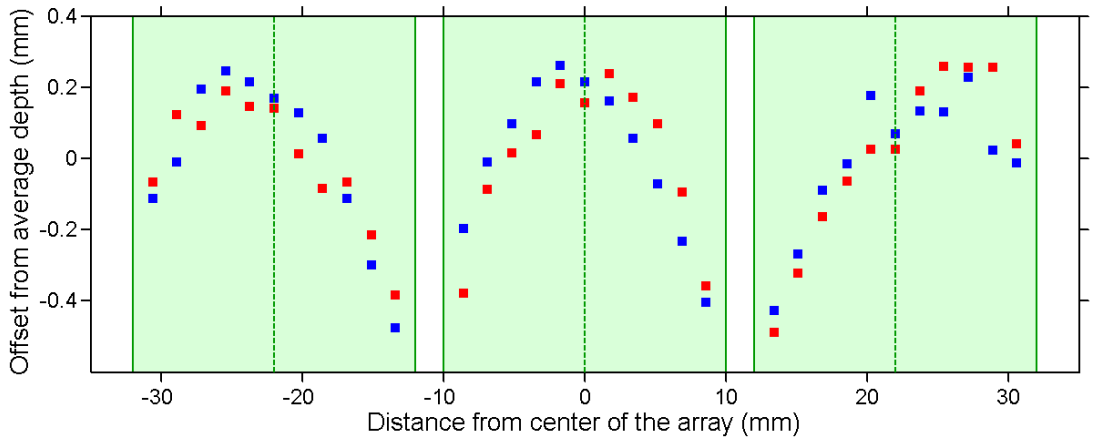

Figure 5.8: Average depth centroid as a function of the distance from the center of the array in the x-dimension (blue dots) or y-dimension (red dots). The centroid is calculated relative to the average depth centroid for each detector. Each data point represents the average depth centroid from six detectors, which itself is an average over eleven pixels in a row or column.

5.3.3 Depth Uncertainty versus Depth

All of the depth uncertainty data presented so far has been from a single depth in each detector. However, it is important to make sure that the system can achieve acceptable depth uncertainty for any position in the bulk. To measure this behavior multiple measurements were taken at different collimator positions for each detector. The beam is moved incrementally from cathode to anode and the depth uncertainty is measured as a function of beam position. The results for six detectors are shown in Figure 5.9.

As a general rule the depth uncertainty is stable throughout the bulk. There is typically a reduction in the depth FWHM near the cathode or the anode. This could be due to events that are reconstructed beyond the physical volume being moved back in, which would artificially reduce the depth uncertainty. It could also be due to the alignment of the pixel-by-pixel centroids when the beam is positioned near the cathode or anode, as discussed in section 5.3.2.

Detector 4O4d, purchased from Orbotech, shows the worst depth reconstruction. It is an example of a detector with a noisy and unstable cathode, which is reflected

by poor depth resolution throughout the bulk. This degree of cathode instability has not been observed amongst the 100 most recently received 15mm thick detectors from Redlen.

The two 5mm detectors achieved the best depth resolution. However, the depth resolution limit for these devices should be much lower than for the thick devices. This is because the drift of electrons through 1mm of a 15mm thick crystal only results in a 7% change in the CAR, while the same drift length in a 5mm thick crystal would result in a 20% change in the CAR. In this sense thinner detectors should be more sensitive to depth, especially if it is limited by the signal to noise ratio.

Detector 4R60 is classified as an excellent detector from Redlen and shows good depth reconstruction throughout the bulk. Detector 4E5 is one of the poorer detectors from eV products, in terms of energy resolution, but it still achieves better depth reconstruction throughout the bulk then detector 4R61 from Redlen. 4R61 has much better energy resolution than 4E5, but experiences an internal electric field uniformity issue that causes depth resolution degradation.

The data shown in Figure 5.9 support the claim that for good CdZnTe material it is reasonable to achieve better than 1mm depth resolution throughout the bulk.

5.3.4 Depth Uncertainty at Lower Energy

Reconstruction of the depth of interaction at low energies using the CAR is only important for coded aperture imaging. It will have little impact on spectroscopy, as the energy uncertainty at low energies tends to be dominated by electronic noise rather than depth-dependent carrier trapping. For Compton imaging all events are reconstructed using drift time, so the depth resolution using the CAR at low energies is irrelevant. For coded apertures it becomes important if the mask is placed above a side surface of the detector rather than the cathode. In this case the lower limit on mask pixel size, which limits the image resolution, will be determined by the depth

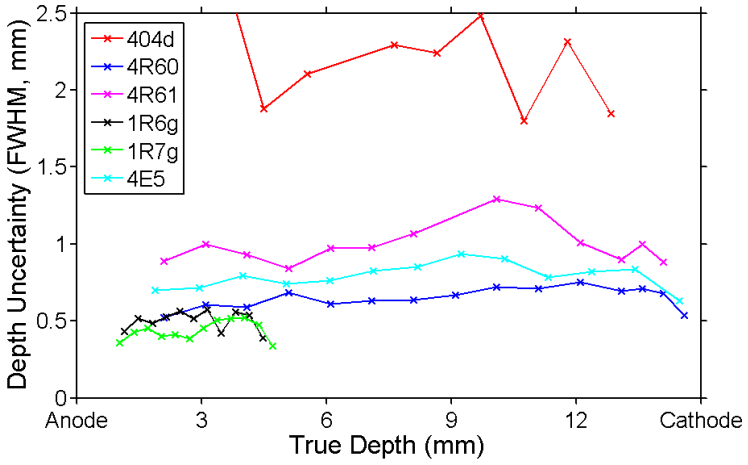

Figure 5.9: The depth uncertainty as a function of depth for six different detectors. Cs-137 single interaction photopeak events are used. A collimator is used to irradiate one depth at a time, a depth distribution is generated, and the centroid is plotted for each detector. All detectors are 15mm thick except 1R6g and 1R7g which are only 5mm thick.

uncertainty. Such a configuration is a long term goal of our group, so collimated data at low energy was taken to decide if the system could meet this need.

The results, for detector 4R60, are shown in Figure 5.10. The outermost rows of pixels will receive the most counts, as the beam irradiates a side surface of the detector. It can be seen that the depth resolution is systematically worse. This is expected, as the signal-to-noise ratio on the cathode signal will be much lower at lower energies. Nevertheless, depth resolution on the order of the 1.72mm pixel pitch is achievable, which means that the spatial resolution of a side surface is not necessarily worse than the spatial resolution on the cathode surface. Therefore, putting a coded aperture mask on the side of the detector is a viable option, assuming the depth of interaction is also reconstructed accurately, which will be the topic of the remainder of this chapter.

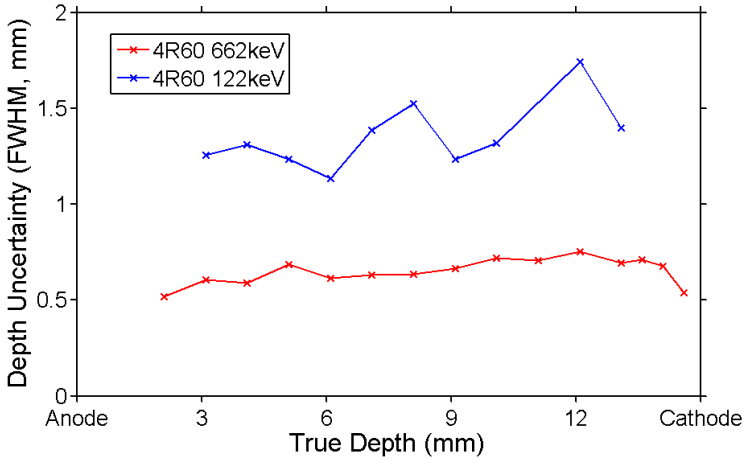

Figure 5.10: The depth uncertainty as a function of depth for six different detectors. Co-57 single-interaction photopeak events are used for the blue curve, while Cs-137 events are used for the red curve. A collimator is used to irradiate one depth at a time, a depth distribution is generated, and the centroid is plotted for each detector.

5.4 Experimental Determination of Depth Accuracy

5.4.1 Locating Cathode and Anode Position

The analysis in this chapter has been focused on measuring the depth uncertainty, which impacts both the spectroscopic and imaging performance of the device. Now the focus will shift to quantifying the accuracy of the depth reconstruction technique, which has no impact on spectroscopy but is critical for image formation. In order to know whether or not the measured depth reflects the true depth of interaction, the beam position must be carefully calibrated to known detector positions. This can be done by sweeping the beam across the anode and cathode to determine the true boundaries of the detector relative to the collimated fan beam.

The planar cathode position is calibrated to the beam position by measuring the photopeak count rate while moving the beam in 100μm increments. The count rate is first measured with the entire beam width striking the detector, and then with the entire beam beyond the detector. Assuming a symmetric beam, the average of these two count rates will be observed when the center of the beam is aligned with

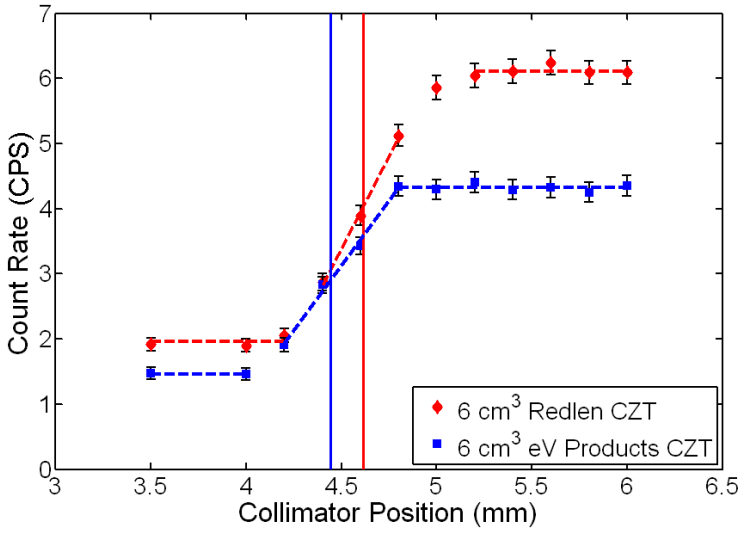

Figure 5.11: This figure shows the technique used to determine the position of either the cathode or, in this case, the anode surface. The low count rate data are fit to determine the number of counts without the beam striking the detector. The high count rate data are used to determine the number of counts when the entire beam strikes the detector. The measured surface position is shown with a vertical line.

the cathode boundary. This cathode boundary position is calculated by fitting the data in the region where the count rate changes rapidly. An example of the fitting technique to determine the boundary position is shown in Figure 5.11.

The beam position of the pixelated anode is more challenging to measure due to the poor hole movement in wide-bandgap semiconductors. By applying a positive bias to the planar electrode, the electrons drift away from the pixels, inducing sufficient charge to register counts from the collimated beam; however, the polarity of the induced signals will be reversed from typical operating conditions and the ASIC is not designed to measure the amplitude of signals with opposite polarity. Therefore, the pre-amp signal of the planar electrode is shaped with NIM equipment, and the pulse-height distribution is recorded with an MCA. Under these conditions, the pixelated anode position is measured using the same procedure outlined for the cathode.

Ultimately this data allows us to measure the overall device thickness. The two 5mm thick detectors from Redlen are measured to be 4.99mm and 5.01mm by the

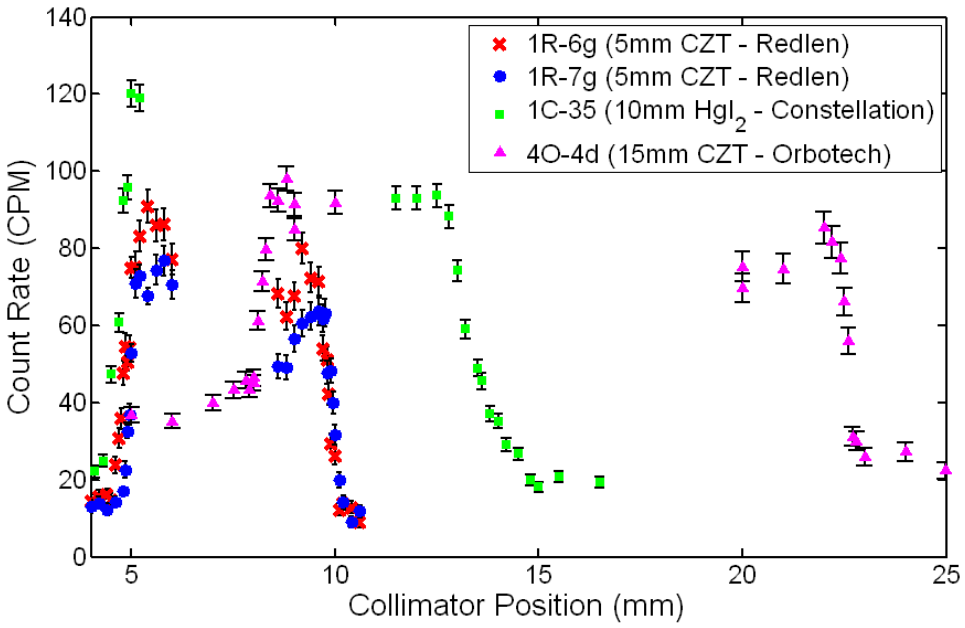

Figure 5.12: This figure shows the data used to find the anode (left side) and cathode (right side) for four different detectors. A collimated beam of 662 keV gammas is used and the count rate is measured as a function of the beam position.

collimation system using the data shown in Figure 5.12. Figure 5.12 includes data for four different detectors. The three CZT detectors (1R6g, 1R7g, and 4O4d) show good, sharp transitions at the expected locations of the cathode and anode. Detector 1C35, a HgI_2 detector from Constellation Technologies, shows a tail on the cathode side distribution and shows a dropoff in counts earlier than expected. This is due to a large cathode side dead region in the device, which was verified using this technique.

5.4.2 Overall Depth Accuracy

The purpose of section 5.4.1 is to determine the relationship between beam position and true depth. Once this is known it is possible to compare the measured depth to the true depth of interaction. The depth spectra for each collimator position are shown in Figure 5.13. In an ideal detector all of the counts would fall on the blue line, but uncertainty spreads the distribution out and inaccuracy shifts the distribu-

tion away from the line. Systematically, 4R61 shows a poorer uncertainty and greater inaccuracy relative to the more ideal 4R60.

The difference between the true depth and measured centroid of each depth distribution is calculated and plotted versus true depth, shown for six detectors in Figure 5.14. The 15mm thick Redlen detectors have the best depth reconstruction accuracy, within an offset less than 0.5mm through the majority of the bulk. In general, all detectors are accurate near the cathode, which is expected because the CAR is calibrated to cathode side information. Close to the anode the CAR is systematically too large. This is expected because the anode signal is no longer constant; it gets smaller nearer the anode which overestimates the ratio.

Detectors with bad trapping, such as 4E5 with almost 10% trapping through the bulk, tend to underestimate the CAR in the central regions of the crystal. This is due to the stronger impact of trapping on the anode signal than on the cathode signal and the calibration of the CAR to cathode side data. The anode signal experiences a greater signal reduction due to trapping, therefore, when the beam is moved to the center of the device the anode amplitude increases more than the cathode amplitude due to the decrease in trapping and thus the CAR is smaller than it should be.

The thin detectors did not show any improvement in accuracy over the thick detectors from Redlen, indicating that their fractional depth inaccuracy is actually much greater than the thick detectors. This could be due, in part, to a larger anode weighting potential in the bulk of the device, reducing the linearity of the relationship between the CAR and the depth of interaction.

For Compton imaging the most important consideration is the relative depth separation between each interaction. If the depth inaccuracy is constant for all depths then the reconstructed interactions will be shifted systematically. This will not have a major impact on the Compton image. However, if the different depths have different measured depth offsets, the Compton image will be degraded.

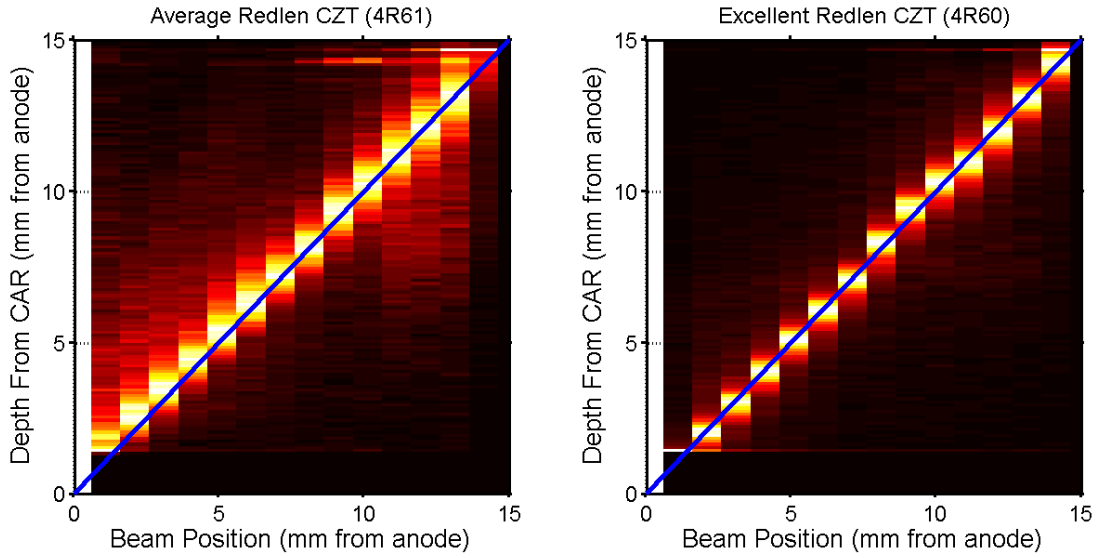

Figure 5.13: This figure shows the depth spectrum collected at each collimator position using a Cs-137 source. The blue diagonal line shows the ideal relationship between measured depth and true depth. Only single-interaction photopeak events are considered.

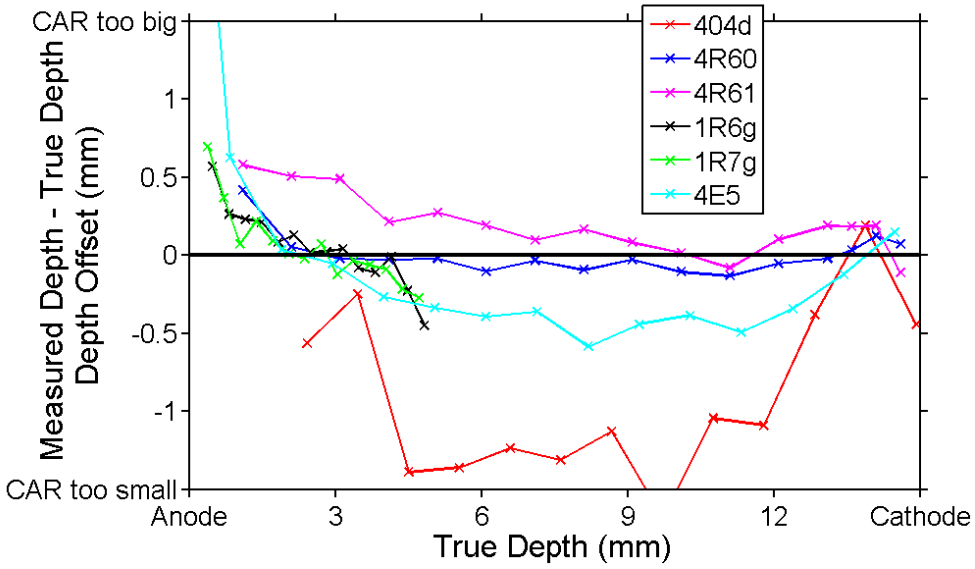

Figure 5.14: This figure shows the offset of the centroid of the reconstructed depth spectrum from the true depth for each collimator position for six different detectors. A depth offset of zero (shown with a solid horizontal black line) is desired. Only single-interaction photopeak events from a Cs-137 source are considered.

5.4.3 Depth Accuracy at Lower Energy

As mentioned in section 5.3.4, the depth reconstruction at lower energies is important only for coded aperture imaging. The Co-57 depth of interaction distributions are shown for each beam position in Figure 5.15. The good detector, 4R60, is capable of accurate depth reconstruction at 122 keV through most of the bulk.

The three collimator positions closest to the anode surface have similar depth centroids. It is difficult for such a low energy deposition to trigger the system so near the anode. Therefore, none of the counts in those bins passed through the collimator. The only events that are measured when the collimator is very close to the anode are from background. These events are uniformly distributed with respect to depth. However, all of the events that occur within a few millimeters of the anode are reconstructed to the same depth. The count distribution for each collimator position in Figure 5.15 is normalized to have the same maximum intensity, so the pile-up of events near the anode is made to look like a peak in the reconstructed depth of interaction distribution.

This work indicates that a good detector like 4R60 could be used for coded aperture imaging with a mask on the side while detector 4R61 could not. A major challenge for the future will be developing techniques to reliably identify these issues in a detector without going through the trouble of using a collimator.

5.5 Conclusions

The collimator experiments have proven to be a valuable tool to understand the depth reconstruction using the CAR in pixelated detectors. Most detectors are shown to reconstruct the depth of interaction with uncertainty on the order of 1 mm throughout the entire volume of the detector. There is systematic bias observed in an array system, where neighboring detectors cause spatially dependendent distortion in the

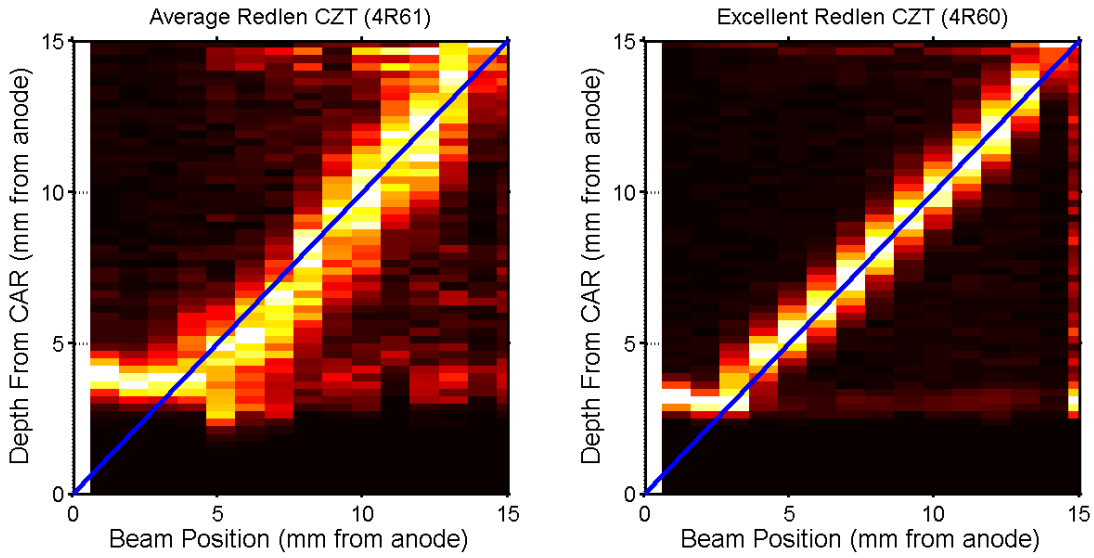

Figure 5.15: This figure shows the depth spectrum collected at each collimator position using a Co-57 source. The blue diagonal line shows the ideal relationship between measured depth and true depth. Only single-interaction photopeak events are considered.

CAR reconstruction. The CAR accuracy is measured by calibrating the position of the beam relative to the detector and then testing each depth within the device. For most detectors tested the CAR accuracy is better than 1mm throughout the volume.

CHAPTER VI

Depth Reconstruction Using Drift Time

6.1 Introduction

Use of the electron drift time is required in order to reconstruct the depths of interactions when a multiple-interaction event occurs within a single detector, as the CAR can only reconstruct the depth of a single interaction. Compton imaging requires position information on at least two interactions, so accurate drift time reconstruction is of paramount importance. This chapter is dedicated to measuring the depth reconstruction behavior of multiple-interaction events. The most important depth reconstruction techniques for drift time have already been described in sections 3.3, 3.3.1, and 3.3.3.

The majority of the measurements in this chapter will be taken using the analog GMI ASIC. This ASIC uses leading edge triggering to obtain anode and cathode timing values, which is known to be subject to amplitude walk. This is achieved by passing the preamplifier signal through a fast shaper, with a shaping time on the order of 100ns, and triggering when the shaped signal passes a fixed threshold. Measurements are also presented using the BNL ASIC which uses the peaking time to identify the anode timing information, which is expected to have almost no walk. This is done by passing the preamplifier through a slower shaper, with a shaping time on the order of 1μs, and reporting the time when the shaped signal reaches

a maximum. It is important to analyze the TAW and timing crosstalk behavior separately for these two systems. If a different timing pickoff technique were used the analysis would change. This chapter is intended to illustrate means for studying these systems in general and to identify problems related to time pickoff.

6.2 Comparison to CAR Reconstruction

The first step in evaluating the timing reconstruction is to study the best case scenario: photopeak single-interaction events at the energy used to correlate the drift time and CAR. These events will not require TAW correction and there are no complications such as WPCT due to multiple interactions. Furthermore, any problems encountered in reconstructing these events will likely apply to all other event types, as the mapping from drift time to CAR is always required.

Figure 6.1 compares the accuracy of the drift time reconstruction to the CAR for single-pixel photopeak events at 662 keV. In general there is good agreement between the drift time and CAR data, with a depth inaccuracy of at least 0.5mm for almost all positions. However, the depth reconstruction is systematically biased toward the cathode side for detector 4R60. This could be due to the fact that the drift time and CAR correlation is performed using a fourth order polynomial fit. In many Redlen detectors the relationship between drift time and CAR is nonlinear and a higher order fit may be required.

Figure 6.2 compares the depth uncertainty of the drift time and CAR. The depth uncertainty is less than 1mm for most positions in both detectors and the drift time uncertainties are only slightly worse than the CAR results. The problems arise closer to the cathode, especially for 4R61. This is explained by a region of slow electron drift in the central region of the detector. Events closer to the anode will never pass this region, but all events closer to the cathode must pass through. Even detector 4R60 demonstrates some of this behavior, although it is much less severe. This is also

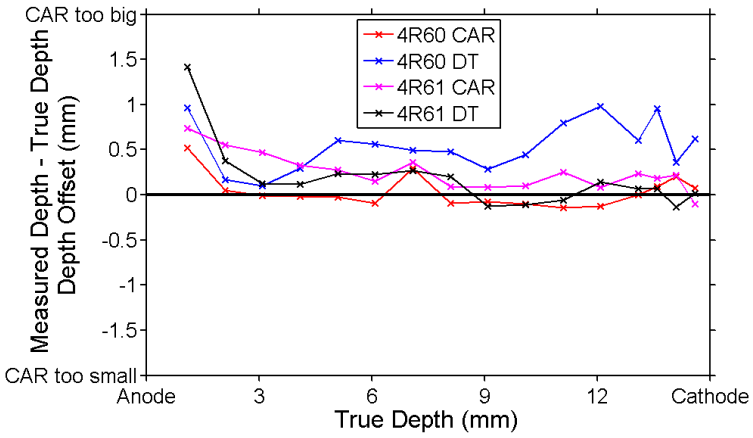

Figure 6.1: Offset of the depth centroid from the true beam position. Drift time and CAR data are compared for single-interaction photopeak events from a Cs-137 source.

reasonable considering that the decrease in the drift velocity in the central depths is much greater for 4R60 than for 4R61.

Overall, the drift time is only slightly poorer than the CAR as a reconstruction technique.

6.3 Time Amplitude Walk Measurements

Now that the timing reconstruction has been validated using single-pixel events we will study more complicated cases. The goal is to understand the anode timing amplitude walk behavior of each system. This is done by studying multiple-interaction photopeak events, as there will be no cathode TAW but the anode TAW will depend on the distribution of energy between the multiple interactions, as discussed earlier in section 3.3.1. Furthermore, any events that occur between neighboring pixels are discarded, as these may not be true multiple-interaction events and have more complicated behavior which will be addressed later. A collimated beam of Cs-137 gamma-rays is used. The data are then binned as a function of energy deposited in each pixel and the depth of interaction in each pixel. Therefore, a two pixel event is binned twice and a three pixel event is binned three times. The TAW should manifest

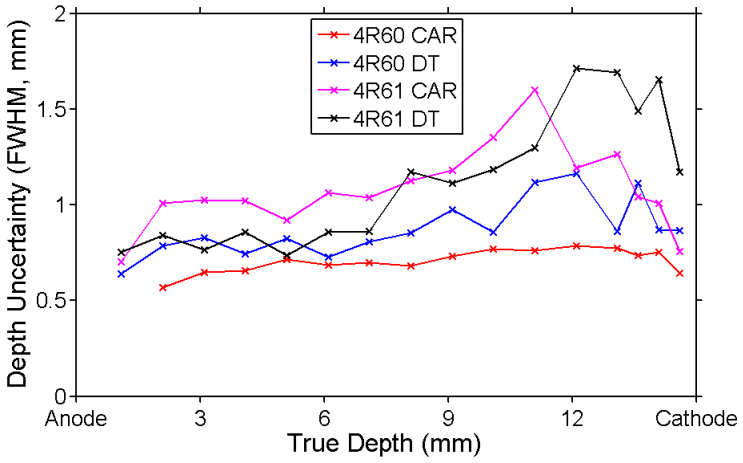

Figure 6.2: FWHM of the depth distribution for several collimator positions comparing. Drift time and CAR data are compared for single-interaction photopeak events from a Cs-137 source.

itself as an offset of the depth centroid as a function of energy deposited on each pixel.

In general the depth behavior of the multiple-interaction events will be more challenging to study, because only one of the interactions is guaranteed to occur at the collimated depth. Therefore, the peak in the depth distribution will always sit on top of a distribution of counts from other depths. Nevertheless, a clear peak is formed and it is possible to measure its centroid and uncertainty.

The results for the GMI ASIC are shown in Figure 6.3. The expected large number of counts away from the beam position is evident from the large smear between 200 and 250 keV. This is due to the relatively high probability that a photon that scatters at 90 degrees will interact at a different depth. Forward scatter is more likely to escape the detector and is less likely to move to a different depth. The most important feature is observed below 200 keV, where the depth distribution is clearly shifting toward the cathode side. This is expected using leading edge triggering, as the smaller energies take longer to trigger and appear to have drifted for a longer time, thus they are reconstructed closer to the cathode. The vertical lines near the anode are due to events with raw data beyond the anode getting piled up in the last CAR bin that is correlated to the drift time.

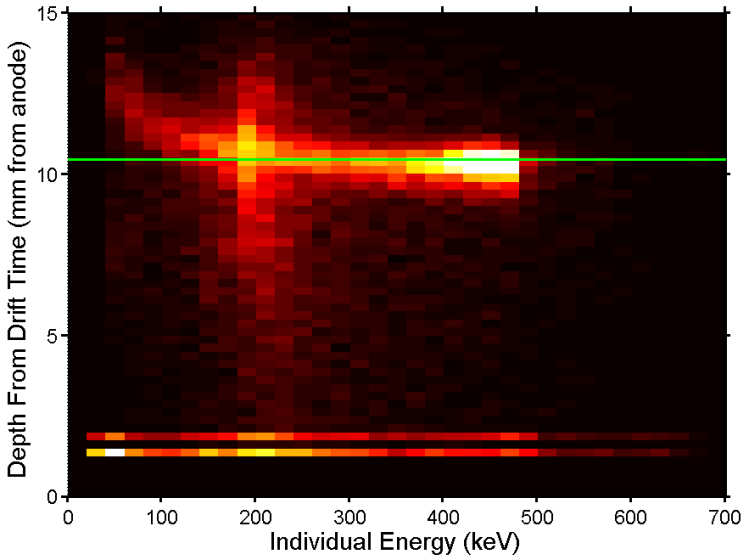

Figure 6.3: Depth of interaction for non-neighboring multiple-pixel photopeak events in detector 4R60 using the GMI ASIC. The horizontal axis is the energy deposited and the vertical axis is the depth for each interaction in an event (thus a 2-pixel event will be counted twice). The horizontal green line shows the expected depth centroid position based on single-interaction data. No TAW correction is applied.

The anode TAW in the GMI ASIC is corrected using the algorithm described in Section 3.3.1. The resulting depth distribution is shown in Figure 6.4. In this case the depth reconstruction at lower energies is improved dramatically.

The results for the BNL ASIC are shown in Figure 6.5. The same Compton scatter pattern is observed, which is expected because the interaction probabilities should not vary when we change ASICs. However, there is no TAW visible in the data, even though no correction has been applied. In this case the peaking time is an effective time pickoff technique.

6.4 Timing Weighting Potential Crosstalk

Now we will move on to a more complicated timing reconstruction issue: WPCT in the timing domain. The concept of WPCT has already been discussed in the energy domain. It is also conceivable that the timing signals could be distorted in a

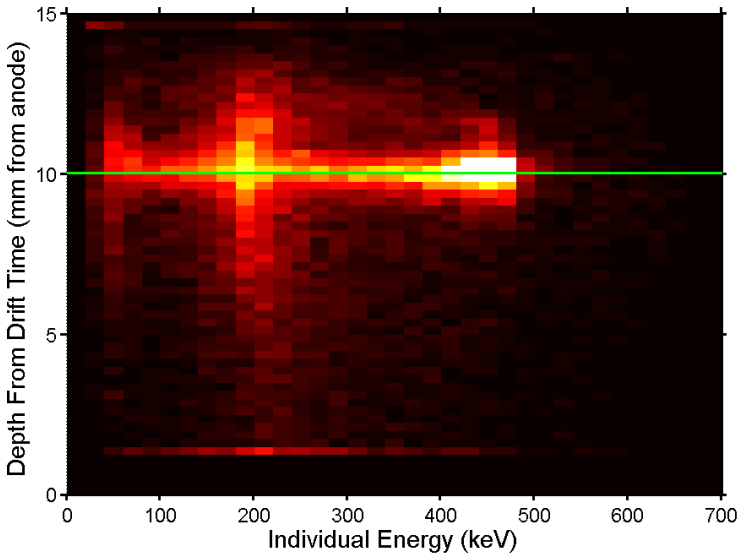

Figure 6.4: Depth of interaction for non-neighboring multiple-pixel photopeak events in detector 4R60 using the GMI ASIC after TAW correction. The horizontal axis is the energy deposited and the vertical axis is the depth for each interaction in an event (thus a 2-pixel event will be counted twice). The horizontal green line shows the expected depth centroid position based on single-interaction data.

multiple-interaction event due to WPCT, especially in the case of side-neighboring interactions where there are large transient signals induced on each pixel.

Figure 6.6 shows the depth distribution in the GMI ASIC as a function of individual energy deposited for side-neighbor interactions, in exactly the same fashion as Figure 6.3. There is a remarkable difference: the side-neighbor events experience almost no anode TAW, even though no TAW correction has been applied. In the absence of WPCT in the timing domain these two plots should look very similar.

This can be explained by the nature of the leading edge triggering of the ASIC and the weighting potential of the device. Imagine two electron clouds drifting above two neighboring pixels. At first they will both induce positive charge on both pixels. Only when the clouds get very close to the anode do we start to see the polarity of the charge induction reverse, such that each cloud will be inducing a positive charge on the pixel that collects it and a negative charge on the neighbor pixels. If the

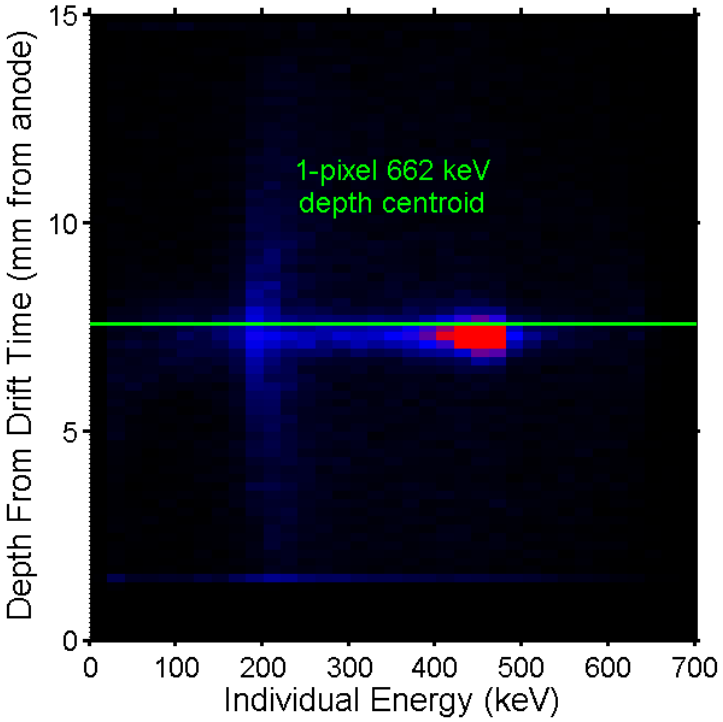

Figure 6.5: Depth of interaction for non-neighboring two pixel photopeak events in detector 4E3 using the BNL ASIC. The horizontal axis is the energy deposited and the vertical axis is the depth for each interaction in an event (thus a 2-pixel event will be counted twice). The horizontal green line shows the expected depth centroid position based on single-interaction data.

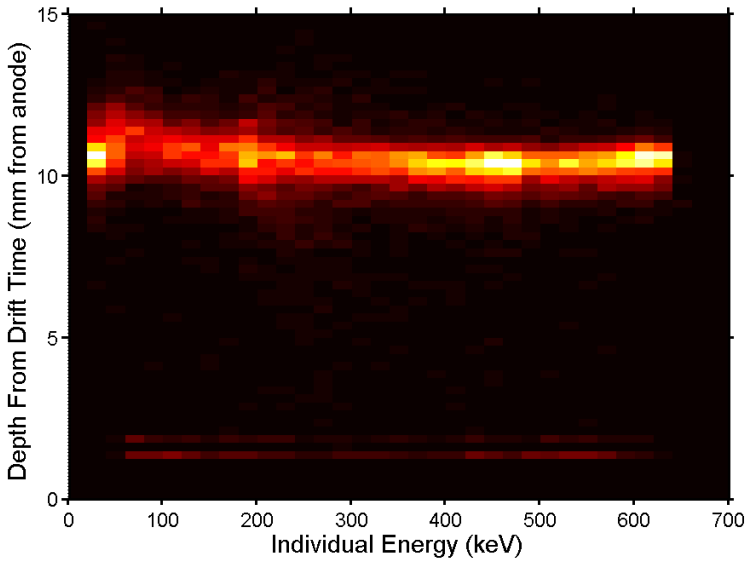

Figure 6.6: Depth of interaction for side-by-side neighboring two-pixel photopeak events in detector 4R60 using the GMI ASIC. The horizontal axis is the energy deposited and the vertical axis is the depth for each interaction in an event (thus a 2-pixel event will be counted twice).

system triggers before the weighting potential polarity reverses for the neighboring pixels then the TAW should be a function of the total energy over the two pixels. Therefore, for side neighboring two pixel photopeak events, the time walk will always be the same as should be expected for a single photopeak interaction. In principle this issue could be alleviated by increasing the anode trigger threshold, but this would be at the expense of sensitivity to small charge inductions.

Figure 6.7 shows the depth distribution in the BNL ASIC as a function of individual energy deposited for side-neighbor interactions. The low energy events are placed much closer to the anode than expected. The non-neighboring events did not have any TAW for this ASIC, yet the reconstructed depth of side-neighbor events changes significantly as a function of energy.

The justification of the behavior in the BNL ASIC is exactly the same as for the GMI ASIC: WPCT in the timing domain. In this case the peaking time is used as a time pickoff technique. Consider a two-pixel side neighbor event with most of

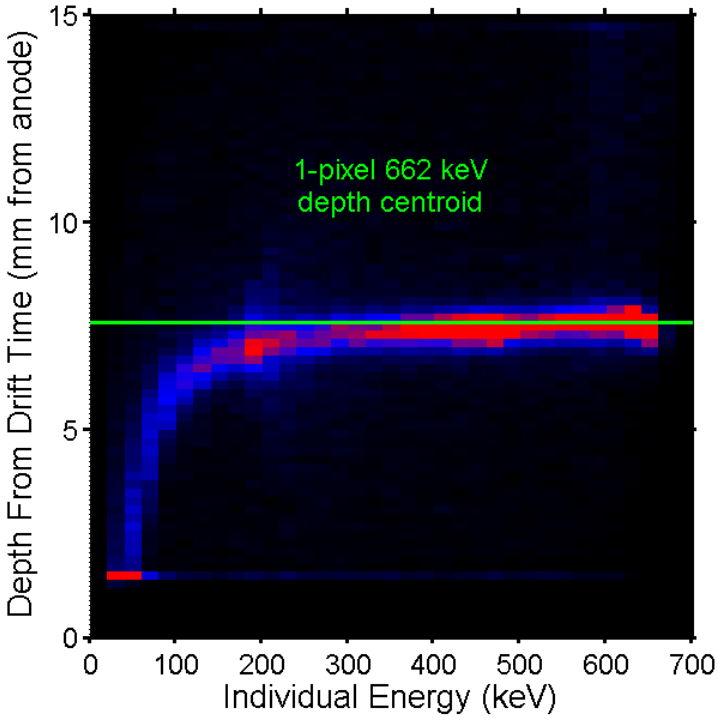

Figure 6.7: Depth of interaction for side-by-side neighboring two-pixel photopeak events in detector 4E3 using the BNL ASIC. The horizontal axis is the energy deposited and the vertical axis is the depth for each interaction in an event (thus a 2-pixel event will be counted twice). The horizontal green line shows the expected depth centroid position based on single-interaction data.

the energy collected by a single pixel. The pixel that collects most the charge will have almost no influence from the pixel that collects little charge. However, the pixel with the small charge collection will be affected by the transient signal from the large charge collection. This transient signal is induced on the pixel collecting the small charge before the true charge collection time. This causes the peak in the charge induction to occur before the true collection, biasing the peaking time toward smaller values and the reconstructed depth of interaction is shifted toward the anode. The effect becomes more severe at lower energies, as the influence from the transient signal becomes more dominant.

The influence of WPCT on the peaking time in the BNL ASIC has been modeled by Dr. Jae Cheon Kim. A simulation package was developed that generates the preamplifier signal of each electrode in a pixelated device considering charge generation, transport, and induction, as well as the response of the electronics (41). The preamplifier and shaped signals are shown in Figure 6.8 for the scenario of a side-neighbor event measured by the BNL ASIC where one pixel collects the majority of the charge.

These results demonstrate that the timing signals for side neighboring events are not completely reliable when using an analog ASIC. Due to the WPCT in the timing domain it is difficult to extract any unique timing information. One simple and effective reconstruction technique is to just assume the depth of interaction is the same for both events. In the GMI ASIC the depth data can be averaged and in the BNL ASIC the depth data from the largest energy deposition should be used. This is effective because many side neighbor events are actually charge sharing, which should be reconstructed to exactly the same depth. Even the Compton scatters tend not to travel very far, or else they would not end up in a side neighbor pixel, so this is an acceptable approximation for many Compton scattered events as well.

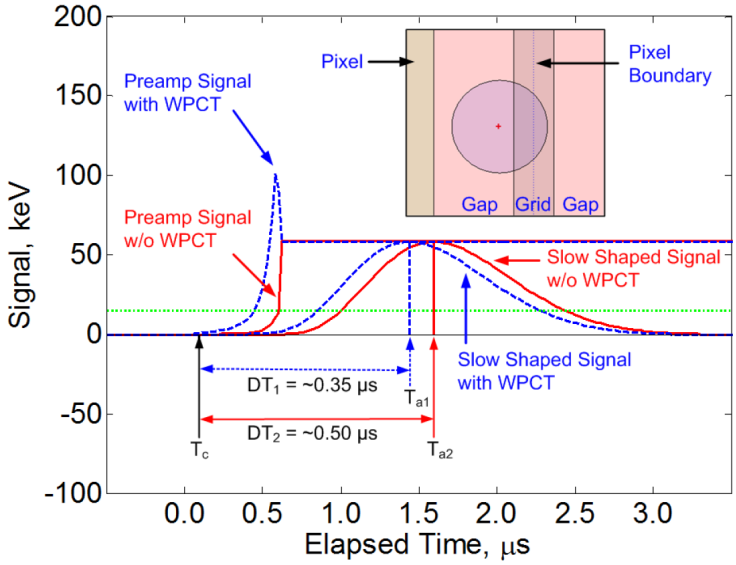

Figure 6.8: The preamplifier and shaped signals for a side-neighbor event in the BNL ASIC where one pixel collects the majority of the charge. The signals are shown for the pixel that collects the smaller fraction of the charge cloud. Data are shown with and without the WPCT contribution from the larger energy deposition. Figure provided by Dr. Jae Cheon Kim.

6.5 Overall Depth Reconstruction for Multiple-Pixel Events

This chapter has focused on detailing the issues involved in the timing reconstruction. Ultimately, the question that matters the most for device performance is: how accurate and precise is the depth reconstruction of multiple-interaction events?

The depth accuracy of two-pixel events is shown in Figure 6.9 for photopeak 662 keV events in detectors 4R60 and 4R61 using the GMI ASIC. Comparing with Figure 6.1, the multiple-interaction events have much more accurate depth reconstruction than single-pixel events when drift time is applied. This can be explained by the calibration described in section 3.3.3, which corrected the systematic shift in the drift time reconstruction of detector 4R60. Thus, the depth inaccuracy is small for multiple-pixel events, with less than 0.5mm uncertainty for most positions in both detectors.

The depth uncertainty of two pixel events is shown in Figure 6.10. Comparing to

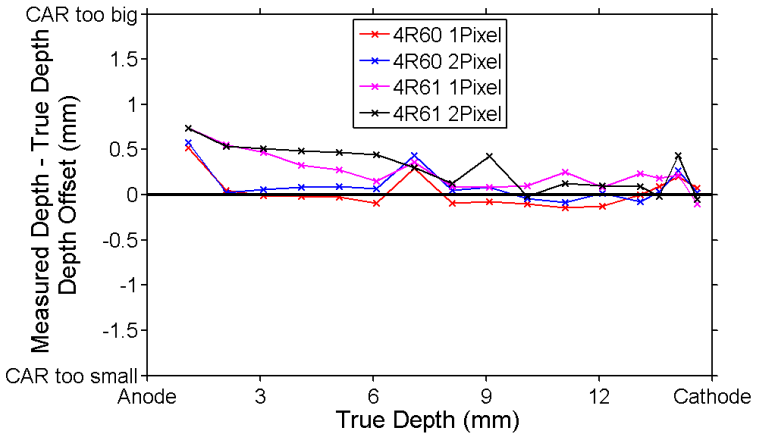

Figure 6.9: Offset of the depth centroid from the true beam position. Two-pixel events are compared to single-pixel events for two different detectors. Photopeak events from a Cs-137 source are used.

Figure 6.2, we see that the multiple-interaction events do have poorer depth resolution than single-pixel events reconstructed with drift time. This is likely due to the fact that the average energy deposited is smaller for multiple-interaction photopeak events and thus the expected time jitter is larger. Detector 4R60 is still capable of achieving depth resolution around 1mm throughout the bulk, while detector 4R61 degrades well beyond 1.5mm FWHM near the cathode, likely due to the electron drift velocity deficit in the center of the detector.

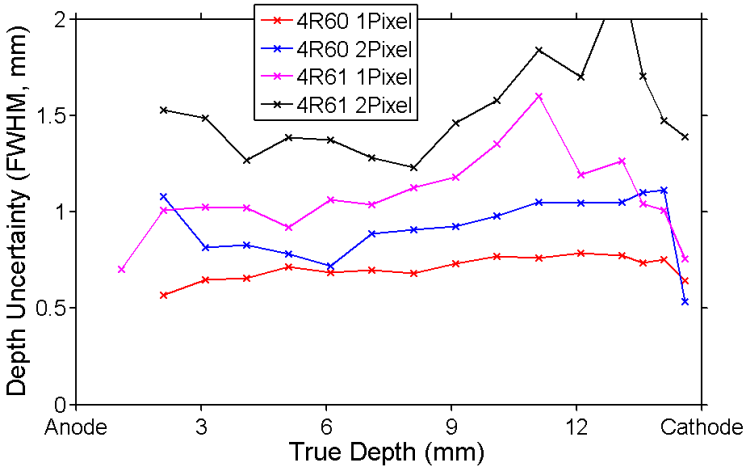

Figure 6.10: FWHM of the depth distribution for several collimator positions comparing. Two-pixel events are compared to single-pixel events for two different detectors. Photopeak events from a Cs-137 source are used.

CHAPTER VII

ASIC Hardware Problems

7.1 Introduction

This chapter focuses on problems due to ASIC design flaws. While ASICs are not expensive to mass produce, the design and initial manufacturing cost of an ASIC is on the order of hundreds of thousands of dollars. For this reason, there exists a need to correct ASIC flaws with software solutions.

Two major system problems with the GMI ASICs will be discussed in this chapter. One issue is high noise on the test pulse. The only way to resolve this without redesigning the electronics is to use a low noise external test pulse, but that is challenging to inject into each pixel. As a result, this problem has been ignored and we have been unable to get a trustworthy measurement of the noise in each pixel.

The high test-pulse noise is noteworthy because it complicates the solution to the second ASIC design flaw: a bad peak-hold circuit. The output of the peak-hold circuit is time dependent, even after the maximum value of the shaped signal has been sampled. This introduces a depth dependent nonlinearity in our system that can be corrected by characterizing the behavior of the peak-hold circuit as a function of amplitude and time. Unfortunately, the noisy test pulse is the best means to characterize this behavior.

This chapter will detail how the multiple-pixel event energy resolution of the

system was improved by adding back the signal deficit caused by the peak-hold circuit. This deficit is measured with the noisy test pulse.

7.2 Single Channel Readout

The amplitude and timing pickoff circuits of each ASIC channel are studied using a mode of operation named single channel readout. In single channel readout mode the test pulse is injected into one channel and the system is triggered at the injection time. The system records the amplitude and timing value for each test-pulse event. The ASIC records the amplitude value by passing the slow shaped signal through a peak-hold circuit. The time delay between the initial trigger of the system and the initiation of the readout cycle is determined by the hold-delay time of the system. Thus, longer hold-delay times will require the peak-hold circuit to hold the amplitude value for a longer time. In single channel readout mode the hold-delay time of the system is incremented between measurements, such that the response of a channel can be determined as a function of the time delay between the system trigger and the system readout.

Understanding this behavior is important because the time interval between the trigger of a pixel and the readout of the system is not constant when measuring gamma-ray events, especially when multiple pixels are involved. Therefore, it is critical that the peak-hold circuit reads out a constant amplitude value independent of hold-delay time. Prior to my arrival, this was known to be a problem in the GMI ASIC, but early attempts at correction proved unsuccessful (42). In sections 7.2.1 and 7.3 I will show why this is a challenging correction to implement.

7.2.1 Test-Pulse Noise

Injecting a test pulse on the input of the pre-amplifier is a standard technique to evaluate the performance of detector readout electronics. It is especially useful for

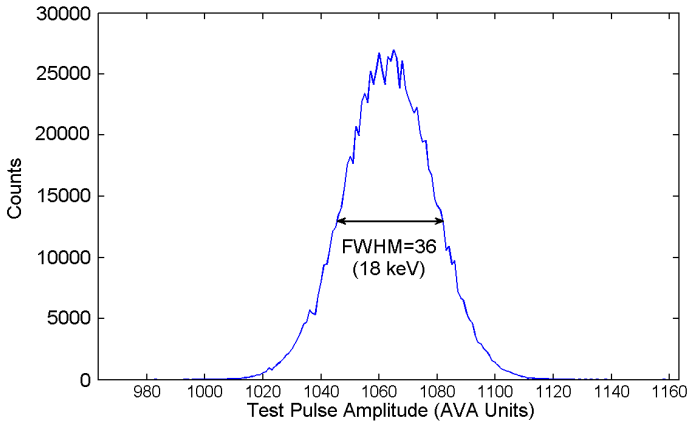

Figure 7.1: Pulse height spectrum from one million test-pulse events in a single channel of the analog GMI ASIC. One ADC unit is roughly equivalent to 0.5 keV.

measuring the electronic noise under various operating conditions. Therefore, it is very important to design an ASIC system that allows for the injection of a test pulse. The GMI system generates a test pulse internally to serve this purpose.

Fig. 7.1 shows the pulse height spectrum of one million pulser test-pulse events. The FWHM of the distribution is an alarming 18 keV. The true system noise is known to be much lower, as it has achieved a FWHM below 5 keV at 662 keV. This is also not due to one bad channel in the ASIC; no channel in the ASIC is capable of achieving an amplitude FWHM close to the true system noise. This high noise is apparent in the test pulse of all analog GMI ASICs tested.

Another troubling aspect of the test pulse is the shape of the pulse height spectrum. After one million events the distribution should more closely resemble a Gaussian shape. This is even more exaggerated when studying the shape of the timing distribution from the test pulse, shown in Fig. 7.2. The system is read out after a fixed delay from the injection of the test pulse. Therefore, the uncertainty in the test-pulse timing value should be due only to the timing jitter associated with the injected trigger. The distribution has two peaks and a dip in the middle, a shape that is consistent across a wide range of amplitudes and timing values, as well as for

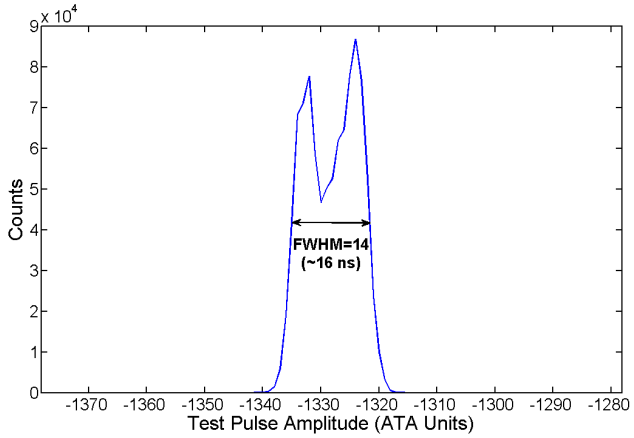

Figure 7.2: Spectrum of timing values from one million test-pulse events in a single channel of the analog GMI ASIC. One ADC unit is roughly equivalent to 1.2 ns.

the dozens of ASIC chips that have been investigated in single channel readout. The cause of the unexpected width and shape of the test-pulse spectra is still unknown, and GMI has been unable to resolve it through design iterations.

The high noise and unexpected behavior make the test pulse an undesirable choice for system calibration. Nevertheless, it is the best means of calibrating the peak hold, thus it is critical to understand these underlying distributions.

7.3 Peak-Hold Drop Measurement

Careful measurements of the peak-hold circuit are required in order to properly correct its time dependent behavior. Fig. 7.3 shows an example of the peak-hold output as a function of hold delay when a test pulse is injected at a constant amplitude. The dashed curve in Fig. 7.3 represents the signal deficit from the maximum value output by the peak-hold circuit. Ultimately, this will be used as a correction parameter that we will add back for each event to recover the true amplitude. This distribution will be referred to as the correction curve.

The initial rise of the measured signal in Figure 7.3 is due to the response of the slow shaper. The maximum value is reached at 1.3 μs, which indicates the peaking

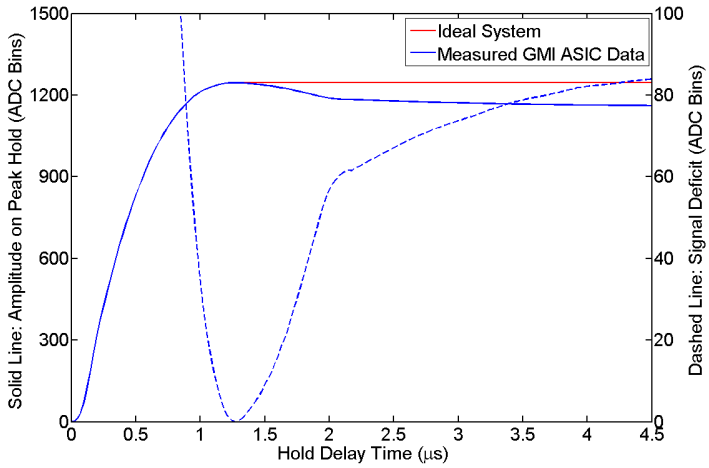

Figure 7.3: The solid blue curve shows the average test-pulse amplitude as a function of hold-delay time. The dashed blue curve shows the difference between the maximum amplitude value and the amplitude at each hold-delay time. The solid red line illustrates the behavior of an ideal peak-hold circuit. The data has undergone significant smoothing, detailed in section 7.4.3.

time of the shaping circuit. The hold-delay time must be large enough to gaurantee the peaking time of each pixel can be reached before system readout for all possible interaction positions and energies.

7.3.1 Amplitude Dependence of Correction Curve

Ideally, the correction curve would have the same shape regardless of pulse amplitude. In that case, a single curve could be measured and scaled to any amplitude. Unfortunately, Figure 7.4 shows that the shape of the correction curve changes significantly with test-pulse amplitude. Therefore, it is clear that this effect must, at the least, be characterized as a function of hold-delay time and measured pulse amplitude.

7.3.2 Channel to Channel Variation in Correction Curve

Based on the results of Section 7.3.1, the peak-hold drop depends on both pulse amplitude and hold-delay time. This could be further complicated by the fact that each pixel has its own independent readout electronics and each combination of

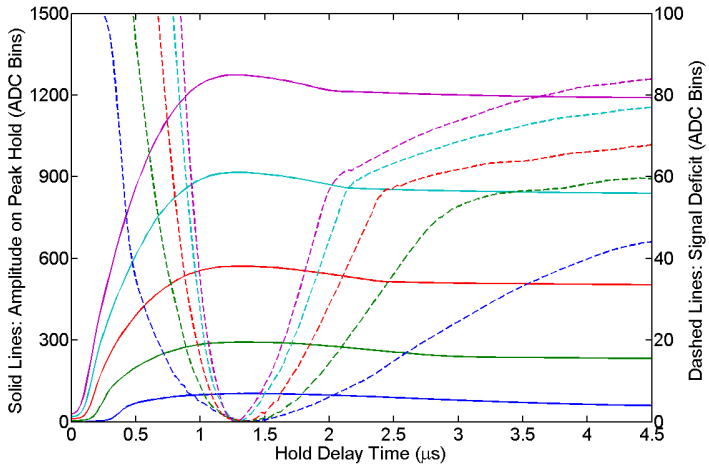

Figure 7.4: Each solid curve shows the average pulse height as a function of hold-delay time for different test-pulse amplitude settings. The dashed curves show the difference between the maximum amplitude value and the amplitude at each hold-delay time. The data has undergone significant smoothing, detailed in Section 7.4.3.

preamp, shaper, and peak hold may demonstrate different behavior. To investigate this possibility the noisy test pulse is injected into each channel of the ASIC, one at a time, using a constant pulse amplitude. The results are shown in Figure 7.5.

The vast majority of the ASIC channels show nearly identical behavior. There are a few channels, in red, that show different behavior. These are known as the special channels, as their preamp signal polarity is inverted to read out the cathode and grid. This observation is consistent across several ASICs with or without a detector plugged in. This indicates that each correction curve can be applied to all anode signals, but the cathode signal will not benefit from this correction.

The system should be much less sensitive to the drop in the cathode signal, as this is only used to reconstruct the depth of interaction (DOI), and small errors in the reconstructed depth result in even smaller shifts in energy, assuming the photopeak centroid position is fairly uniform across depth. Compton imaging depends on the multiple-pixel event DOI reconstruction, but this only uses the cathode signal to adjust the centroid depth of all interactions in an event; the relative interaction

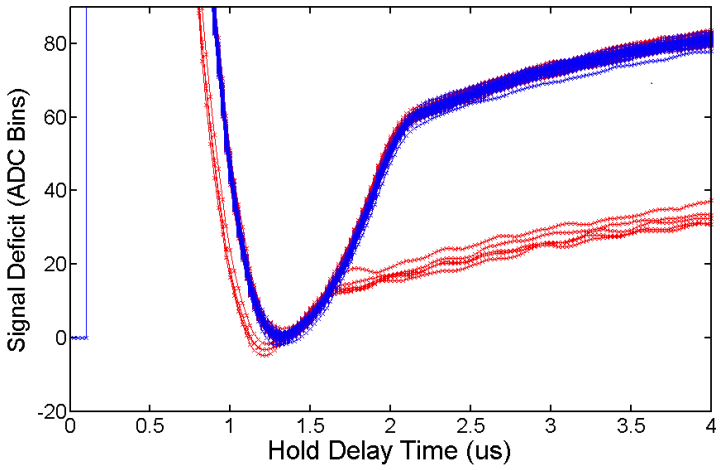

Figure 7.5: Each curve shows the peak-hold drop correction curve for one channel in an ASIC. The lower numbered channels are colored in red and the higher number channels colored in blue. The five outlier curves, in red, are from the special channels, numbered one to five and used to readout the cathode and grid.

separations remain the same regardless of cathode signal amplitude.

7.3.3 Timing Linearity

All of the correction curves presented thus far have been measured as a function of hold-delay time. For each pixel, the correction curves must be applied as a function of the timing value read out by the time-to-amplitude converter (TAC) of each pixel. Ideally, the TAC will have a very linear response, such that the timing behavior of each channel can be easily calibrated relative to the hold-delay time. In order to study this, the timing centroid of a pixel was measured as a function of hold-delay time. The derivative of the timing centroid versus hold-delay time, should be constant for all hold-delay times, assuming a linear response. This derivative is shown in Figure 7.6 to be constant across the entire time range of interest. Due to the strange test-pulse timing distribution shape, as shown in Figure 7.2, a wide region of interest must be used to find each centroid, or significant error is introduced.

The encouraging conclusion from this experiment is that the TAC is constant

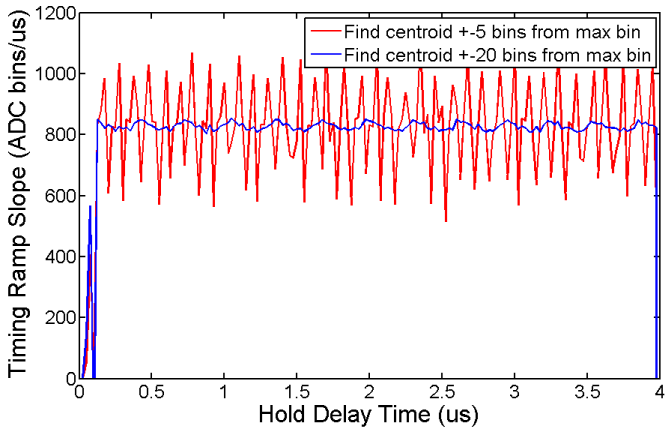

Figure 7.6: The rate of change of the TAC output as a function of hold-delay time, for one ASIC channel. If response of the TAC is linear, then the slope should be constant. The timing centroid uncertainty is very high unless a wide region is used to calculate it.

within the measurement uncertainty caused by the noisy test pulse.

7.4 Peak-Hold Drop Correction

Until now this chapter has focused on illustrating the problem with the peak-hold circuit and the test pulse as well as presenting the techniques for acquiring the necessary data to correct it. The rest of this chapter will detail how the calibration technique is actually implemented and show the impact on energy resolution.

Ultimately, the goal is to determine the signal amplitude prior to the peak-hold drop for each amplitude value read out by each collecting pixel. The correction factor depends on the time interval between charge collection and system readout as well as the signal amplitude. The process of converting the measured timing value into the timing intervals used for the test pulse is detailed in section 7.4.1. The process of reconstructing the signal amplitude is detailed in section 7.4.2.

7.4.1 Timing Value Conversion

It was shown that the TAC has a linear response in section 7.3.3. The situation is made even simpler due to the realtime active baseline detection implemented by Dr. Feng Zhang. For each block of approximately 1000 events the timing and amplitude baselines are measured for all of the pixels that did not collect charge for each event. Using this technique, a baseline offset very close to zero can be achieved for the timing circuit.

This means that the conversion from timing value to peak-hold time will require only a timing gain of each channel. This can be obtained two ways. One is to inject a test pulse into each channel and find the gain based on the timing centroid. However, in Figure 7.6 it is clear that the timing centroid measurement is strongly influenced by the strange shape of the timing distribution and it is challenging to get a reliable measurement.

An alternative technique is to use data already calculated during the regular calibration process. One of the first calibration steps is determining a timing cutoff for each channel, which specifies an upper bound on what we consider reasonable timing information. Typically the cathode triggers system readout and the pixels will trigger at a slightly later time. However, the maximum timing value always occurs when the pixel generates the first trigger in the system, which is true for interactions near the anode side or single-pixel events with no cathode trigger. In this case, the time delay between the pixel trigger and the system readout is just the hold-delay time used for the measurement. Therefore, these anode timing cutoffs can be directly converted into the timing gain of each channel. This simple technique yields similar results to injecting a test pulse into each channel.

One final adjustment to the timing information is required due to the anode TAW. When the correction curves were generated the system readout was triggered at the instant the test pulse was injected. However, in the real system the trigger is subject

to TAW and will occur slightly later than the initial rise of the pulse. Therefore, an appropriate TAW correction algorithm must be applied prior to correcting the drop of the peak-hold circuit. The cathode TAW can be neglected unless a peak-hold drop correction is applied to the cathode signal.

7.4.2 Amplitude Correction

The correction curve is always reported in terms of signal deficit. Studying Figure 7.4 as an example, the correction curves have a minimum value of zero that occurs at the hold-delay time when the test pulse outputs the maximum. This signal deficit value is the amplitude that we will add back to each event to correct the peak-hold drop.

However, this process requires normalizing each curve to the measurement of its maximum. This is problematic because the curve is undergoing the most rapid change in shape at this point. Therefore, if the timing dimension is undersampled the maximum value will be identified inconsistently. The uncertainty in each of the correction curves will be a function of both the uncertainty at each point on the curve and the uncertainty of the normalization point. By selecting the maximum as the normalization point the uncertainty associated with the correction curve is significantly increased compared to pinning each curve to the most slowly changing region where several points can be averaged. The disadvantage of the later approach is that it will not accomplish a secondary goal of the peak-hold drop correction algorithm, which is to reduce nonlinearity of the system. This will be discussed in detail in the following chapter. For this reason, all of the correction curves are normalized to the maximum peak-hold output.

One final detail is in the amplitude sampling mesh. The timing mesh is sampled as finely as possible, using a sampling period of 25ns, in order to do the best possible job capturing the maximum amplitude and to provide more measurement points for

averaging purposes. The choice of the amplitude sampling mesh is dominated by the low energy behavior of the peak hold. The correction curve changes much more rapidly at low energies and must be sampled more often, while at very high energies the shape of the curve changes very little. Therefore, at the low energies the system is sampled as finely as the test-pulse amplitude can be adjusted. The interval between test-pulse amplitudes increases with energy, such that a very coarse mesh is used at the high energies.

All injected test-pulse data for a complete calibration is shown in Figure 7.7 to illustrate the logic behind the amplitude sampling intervals. The top graph in Figure 7.7 plots the peak-hold value as a function of hold-delay time to illustrate each test-pulse amplitude that was used. The bottom graph shows the correction curve as a function of energy. If the amplitude mesh was selected perfectly, then the spacing between each two correction curves should be about the same, such that no two amplitude bins have radically different behavior between them. However, it is clear from the bottom graph in Figure 7.7 that the largest separation between correction curves occurs at the lower amplitudes. This is the best that can be done, given the fact that the test-pulse amplitude can only be specified in intervals of roughly 15 keV, which is insufficient at the lowest energies.

7.4.3 Data Smoothing

The acquisition time is always a major consideration when proposing a new system calibration. Due to the test-pulse uncertainty the peak-hold drop calibration does require a significant acquisition time, on the order of hours. The pulse can be injected in parallel to six ASICs at once in an array, which speeds up array calibration by a factor very close to six. Nevertheless, it is always desirable to reduce the calibration time whenever possible.

To accomplish this goal, the data can be smoothed by averaging neighboring

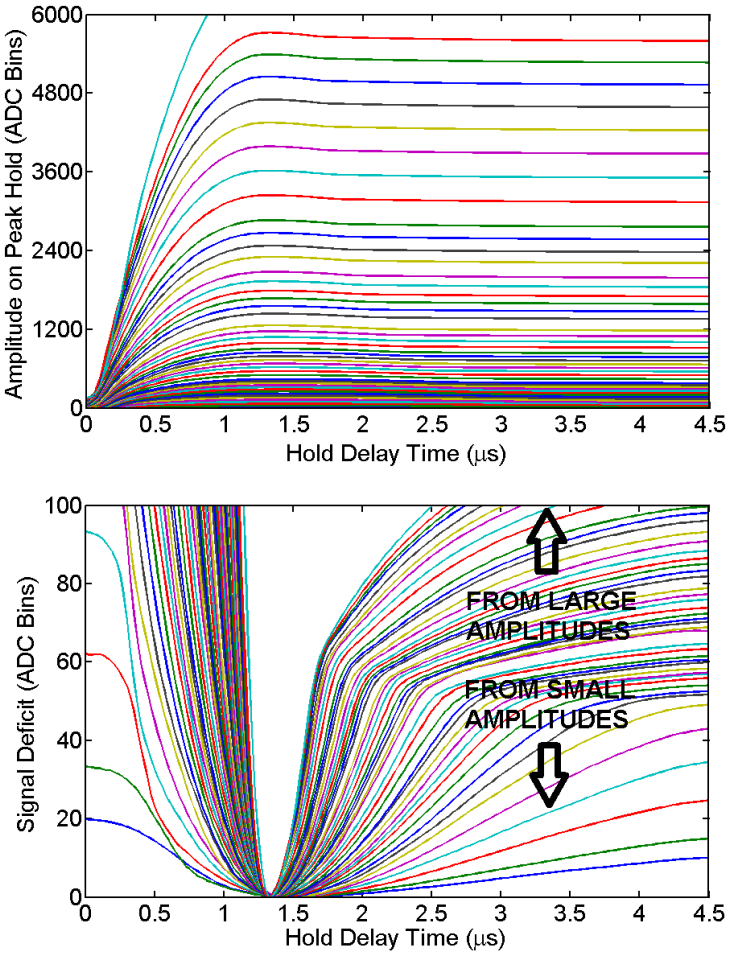

Figure 7.7: Illustration of the need for variable amplitude sampling intervals. The peak-hold response (top) and correction curve (bottom) are shown for all test-pulse amplitudes injected for a complete ASIC calibration. For low amplitudes the amplitude is changed slowly, as shown on the top plot. However, the correction curve is changing so rapidly at low energies that this region has the largest spacing between correction curves, as shown on the bottom plot.

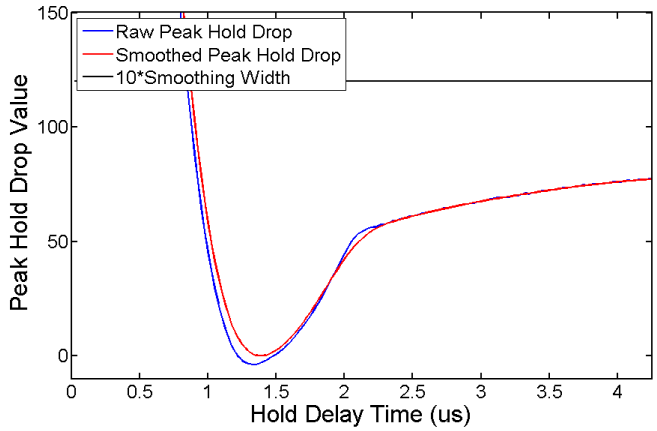

Figure 7.8: Impact of smoothing a peak-hold response using a uniform sampling interval. The blue curve shows the raw data. The red curve shows the output of the smoothing algorithm. The black curve shows the smoothing window width at each hold-delay time, which in this case is a constant value of 12 samples (spanning 300 ns).

datapoints. This technique is effective if the statistical fluctuations are greater than the true change within the smoothing window. To initially study this problem a dataset with a very long acquisition time, and thus very low statistical uncertainty, is used. In Figure 7.8 the neighboring 10 values on each side of each datapoint are averaged for all hold-delay times. This technique results in good agreement between the raw and smoothed data in the time region between 2.5 and 4.0 μs, where most of the gamma-ray events will fall. However, the maximum value is not correctly identified because the smooth width is too large in that region.

Figure 7.9 shows the result of allowing the smooth interval width to vary, based on the amplitude of the derivatives. When the curve changes slowly, a wide smoothing interval is used, otherwise, the smoothing interval is much smaller. This technique does an excellent job when the data is already quite smooth. For a more realistic acquisition time the smoothing window calculation experiences greater uncertainty, but the technique is still effective for all ASICs and amplitudes tested. An example of applying the smoothing algorithm to data with limited statistics is shown in Figure 7.10.

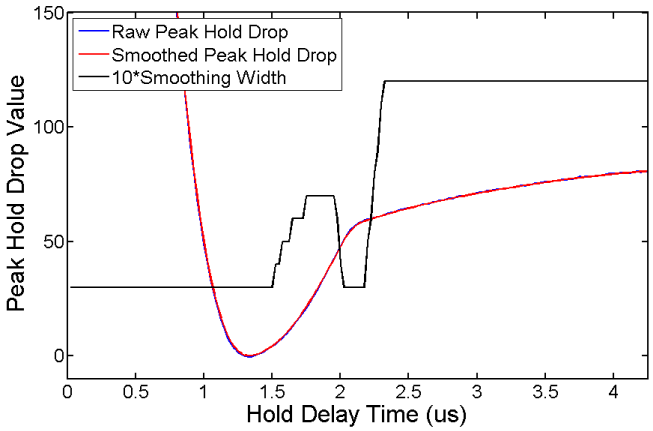

Figure 7.9: Impact of smoothing a peak-hold response using a variable smoothing interval. The blue curve shows the raw data. The red curve shows the output of the smoothing algorithm. The black curve shows the smoothing window width at each hold-delay time.

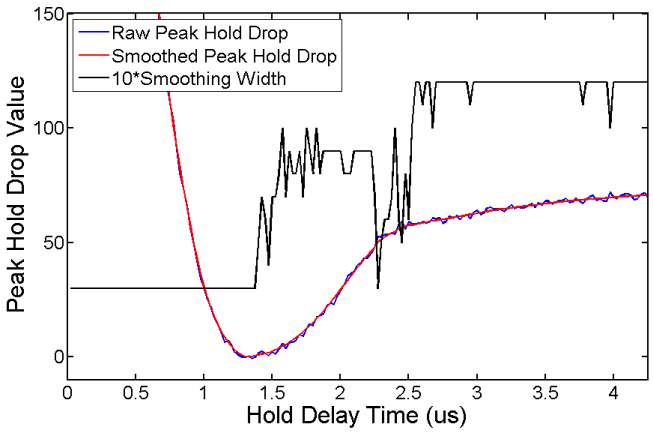

Figure 7.10: Impact of smoothing a peak-hold response using a variable sampling interval. The dataset shown here has significant statistical uncertainty. The blue curve shows the raw data. The red curve shows the output of the smoothing algorithm. The black curve shows the smoothing window width at each hold-delay time.

7.4.4 Impact of Peak-Hold Drop

The final result of applying the peak-hold drop algorithm to every detector in an eighteen detector array is shown in Figure 7.11. For one- or two-pixel events there is almost no impact in energy resolution due to the peak hold. This is expected because the most problematic region for the peak hold is in the lower energies. A single-pixel Cs-137 photopeak event will always occur at 662 keV and it is relatively unlikely that a two pixel event will have a very low energy deposition. However, with an increasing number of pixels triggered more and more low energy signal collections occur. Thus, for the three pixel and especially for the four pixel events the improvement due to the peak-hold drop correction is significant.

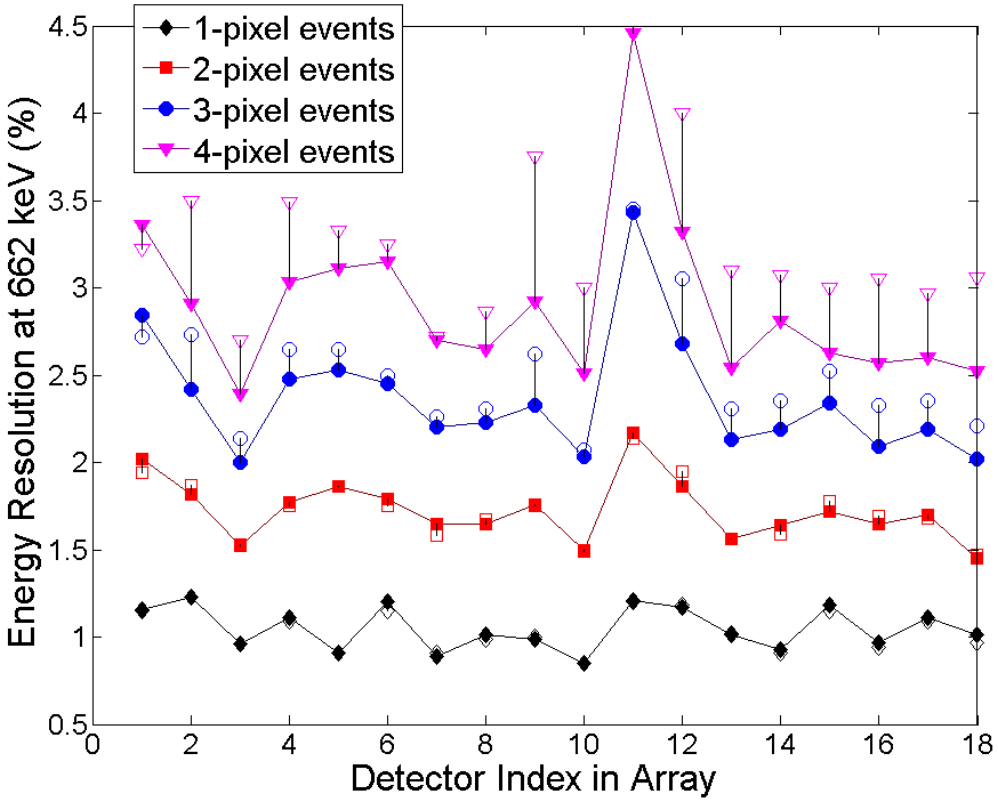

Figure 7.11: Energy resolution at 662 keV for each detector in an array of eighteen detectors before (empty shapes) and after (filled shapes) applying the peak-hold drop correction. Data is separated based on the number of pixels that are triggered. 1- and 2-pixel events show no change on average, while 3- and 4-pixel events improve systematically.

CHAPTER VIII

System Linearity

8.1 Introduction

In an ideal gamma-ray spectrometer the measured pulse height will be proportional to the deposited energy. This chapter will investigate the linearity of the reponse for CdZnTe detectors coupled to the GMI ASIC or to the BNL ASIC. Methods to calibrate the nonlinearity of the system will be discussed. Finally, the performance of an eighteen detector array system will be evaluated after the system nonlinearity has been corrected.

8.2 Nonlinearity Correction for 3D CZT

8.2.1 Comparison to Traditional Techniques

One reason that germanium detectors are a good choice as gamma-ray spectrometers is their near linear response. In 1967, a team of researchers at the University of Michigan showed that a Ge(Li) detector could achieve at most a 1.2 keV deviation from linearity in the range of 100 keV to 1.4 MeV (43). Furthermore, this nonlinearity was due primarily to the electronics.

Achieving this level of linearity is more challenging for a pixelated CdZnTe device. A germanium detector can be read out using a single preamplifier, while a CZT system

requires a preamp for each pixel. Therefore, the demands placed on the preamp designers are much more severe; in addition to the noise they must minimize the footprint and power consumption of the electronics. The linearity of the electronics is secondary to these factors in terms of design considerations. As a result, significant differential nonlinearity in the GMI VAS_UM3 system was observed during initial tests at the University of Michigan (38).

The process of calibrating the nonlinear preamp response is challenging in pixelated detectors due to the large number of independent readout channels. For both the GMI and BNL analog ASICs the variation in the response of each preamp is sufficient to justify independent calibration. With over 2000 readout channels in the eighteen detector array, long count times are required to get a statistically significant calibration in each pixel for each source energy line.

The event identification capability, inherent to a pixelated device, ultimately leads to additional nonlinearity correction capability. In a device without position sensitivity it is challenging to know the number of gamma interactions that occur in each photopeak event. Therefore, if there is some nonlinearity due to information carrier generation or collection it is very difficult to calibrate. A Cs-137 photopeak event could be caused by a single electron cloud generated by a 662 keV energy deposition or by two or more electron clouds with many possible combinations of individual energy depositions.

In a pixelated semiconductor the charge collected by each pixel can indicate the energy deposited by each interaction along the incident gamma-ray track. The majority of single-pixel events are single-interaction events. Therefore, by considering only single-pixel events in the nonlinearity calibration, the calibration will be able to correct nonlinear charge generation or collection. In scintillators such as NaI this could be used to lower the limit on energy resolution, if such a scheme could be realized for light collection.

Calibrating a detector using only the single-pixel events makes it very easy to independently correct the response of each preamp. However, the probability of a photopeak event occurring in a single pixel decreases monotonically with energy. At energies above 1.5 MeV the probablity of a single-pixel event is very low. For this reason the response is challenging to calibrate on a pixel-by-pixel basis in this energy range. Instead, data from all pixels can be combined for each detector, which comes at the expense of energy resolution.

The single-pixel events should permit the complete calibration of any nonlinearity due to the preamps or charge collection issues in the device. For a two pixel event, the nonlinearity correction determined from one pixel events should be applicable to each energy deposition. However, the photopeaks for multiple-pixel events do not always appear at exactly the expected energies, for reasons that will be discussed later in this chapter. Therefore, additional nonlinearity corrections are generated for 2, 3, 4, and 5+ pixel events. These correction parameters cannot be determined on a pixel-by-pixel basis because multiple pixels are involved in each interaction.

8.2.2 Summary of Prior Work on Nonlinearity

Dr. Feng Zhang implemented a nonlinearity correction for our 3D CZT systems before my arrival at Michigan. In 2009 he presented the performance of the BNL ASIC system for energies up to 2.6 MeV (44), which included the basics of how the linearity was performed. However, there were many critical details and considerations left out that will be discussed here in order to fully document the existing calibration techniques.

The first critical decision to make is when the nonlinearity correction should be applied. If applied before depth correction then the photopeaks will be more broad, requiring additional counts to find each photopeak position. Furthermore, different sources will have different depth distributions, introducing a systematic bias as a

function of energy. Therefore, it is necessary to calibrate nonlinearity after depth correction. The major problem with this approach is that the nonlinearity will affect the CAR, which is used to reconstruct the depth. Ultimately, this is dismissed as a fairly small effect, due to limited depth resolution to begin with and the fact that the most critical depth reconstruction is done using drift time, which is only mapped to the cathode-to-anode ratio at a single anode energy. The TAW correction resolves the energy dependent depth reconstruction of the timing signals.

If the nonlinearity is due entirely to the preamplifier then it should be possible to correct the nonlinearity of each pixel with one response function. However, there are other complications, such as the peak-hold drop discussed in Chapter VII, that can cause a nonlinear response as a function of depth. Our ability to correct these effects with gamma-ray data is very limited because low energy sources can only penetrate to a fraction of the depths for most pixels. This is why the work in Chapter VII was a critical step in establishing a system response function with correctable nonlinearity.

A nonlinearity calibration algorithm was developed for pixelated semiconductor detectors. Many radioactive sources, typically Am-241, Co-57, Ba-133, Na-22, Cs-137, Co-60, and Th-228 or Na-24, are used to provide gamma-ray data at a variety of photopeak energies for each pixel. The same depth correction, calculated using Cs-137 data, is applied to all events from all sources. Events from all depths are combined for each pixel for each source. The photopeak position is measured for all probable emission lines for all sources for every pixel. The number of events acquired for each source is typically an order of magnitude less than for the Cs-137 calibration used to perform the depth correction, as data are not required at each depth for nonlinearity correction.

The measured data provide the system response at several discrete energy values. In order to apply this correction to any measured event, the system response must be continuous with respect to energy. After testing a variety of options, a polynomial

fitting function was used to describe the data, typically with a fifth order fit. However, when the correction was extended to energies above 1.5 MeV it could not reliably identify the photopeak position for each channel due to a lack of counts. Therefore, an overall response is calculated from all pixels combined for events above 1.5 MeV. This is spliced together with a pixel-by-pixel fit at lower energies, including a transition region of several hundred keV where both fits are used. This technique is unnecessarily complicated for most detector systems and undesirable even for the pixelated system, as variation in nonlinearity on a pixel-by-pixel basis is not corrected at high energies.

In order to insure that the multiple-pixel event photopeaks appear in exactly the same position as the 1-pixel events nonlinearity corrections were performed for events involving two, three, four, and five or more pixels. Events from all pixels are combined and a single response function is generated for each number of pixels involved in an event.

An important discussion point is the fact that the test pulse data is not used in the nonlinearity correction, even in the case of the BNL ASIC that has a properly functioning internal test pulse. Dr. Feng Zhang attempted to use the test pulse for the nonlinearity correction, including combinations of test pulse and gamma-ray data, but nothing could outperform the results he obtained using only gamma-rays (45). One explanation is that the test pulse is different than a true gamma-ray pulse with respect to shape and the manner in which the system is triggered, as the system is not triggered by the timing pickoff when the test pulse is injected. The shape of the test pulse is the same at all energies, while the gamma-ray rise time will trend toward larger values at higher energies as the electron cloud expands. Another major problem with the internal test pulse is that it is difficult to know the true amplitude of the pulse injected into the system, the best that can be done is to assume that the digital pulse amplitude settings are perfectly linear with no baseline offset.

8.2.3 Techniques to Automate Calibration

The nonlinearity calibration must be performed in an automated fashion, as there are more than 2000 independent readout channels in an array of eighteen pixelated detectors. A completely automated nonlinearity calibration is challenging to implement because it is difficult to know where each peak should be and what constitutes a real peak that will have a beneficial contribution to the overall fit. Therefore, my techniques focus on three issues: defining an appropriate search region for each peak, discriminating against statistically insignificant or erroneous peaks, and limiting the data that is actually used for each fitting curve such that all points are within expectations.

Defining the search region for each peak is challenging, especially for sources with multiple emission energies in a narrow energy range, such as Ba-133. It is not practical to solve the arbitrary problem, such that it would work for any source in any detector, without some prediction of the behavior of the preamplifier. Otherwise, if the nonlinearity could take any form, it is impossible to define a limited search region that does not overlap the search region of other peaks. Instead, the capability was added to allow the user to input some guidelines for how each source should be treated. These include the width of the search regions, specified in percent of photopeak amplitude for each source, the relative offset of the search regions, the number of counts required to be considered a peak, and the amount of smoothing desired. Typically high energy sources or low count sources require some smoothing to consistently identify the peak.

Special treatment is required if the search regions for two emission energies overlap. It is not uncommon that the more dominant emission line will be identified for both emission energies. In this case, the emission energy closest to the measured position is assumed to be correct. The search region of the other line is shifted further away until a unique peak is found or the search region has been pushed too far from the

calibration energy.

Improving the peak identification algorithm is another key step in automating the process. For each source the user can specify a minimum number of counts to consider a feature a true peak. Without such a requirement a peak will always be found regardless of whether or not it is present. Smoothing the data with a smoothing interval tailored to the expected width of the peak helps discriminate the true peak from other features when identifying the local maximum in the search region. After the peak position is estimated a Gaussian fit is performed on the raw data to estimate its FWHM and peaks with unexpected FWHM values are discarded.

Even with all the changes described in the previous paragraphs, there are still some features that are incorrectly identified as photopeaks. An example is confusing a sharp feature near the lower level cutoff of the system with the 60 keV line from Am-241. In order to eliminate these unexpected features, the validity of each fit is verified. If the average departure between the peak positions and functional fit is beyond some threshold then each point in the fit is inspected. A point is tested by removing it from the fit and recalculating. The point that caused the biggest improvement in fit quality is eliminated permanently. This process is repeated until the fit goes below the intervention threshold. This is a significant improvement over the prior technique, which involved manual inspection of each pixel to validate the fit quality.

If a peak position is not found or discarded then the data from an overall fit from all pixels is used. This preserves the correction of the first order nonlinearity behavior, which is the same for all pixels. However, the response of each channel is different, so when the overall data is used the energy resolution will degrade.

After implementing all of the changes described in this section it is possible to calibrate the nonlinearity of the entire system in an automated and repeatable fashion.

8.3 Measured Data Using the GMI ASIC

The results of calibrating the nonlinearity of an eighteen detector array are presented in this section. The data for each source was taken for all eighteen detectors simultaneously with the cathode trigger disabled. This was done to ensure that no detector could generate cathode noise triggers that would increase the dead time of the array. Measurements were taken with Am-241 and Co-57, Ba-133, Na-22, Cs-137, Co-60, and Na-24. Na-24 is a useful source for calibrating the high energy response, as it has only two probable gamma emissions at 1369 and 2754 keV that are emitted in more than 99.9% of decays. Samples were created by Prof. Mike Hartman at the Neutron Science Laboratory at the University of Michigan.

8.3.1 Pixel-by-Pixel Variation in Linearity

The first data to examine are the responses of each pixel within a single crystal to determine the uniformity of the linearity. If all pixels demonstrated very similar behavior an overall nonlinearity could be applied to the entire detector and far fewer counts would be required. Figure 8.1 shows the difference between the known gamma-ray energy and the measured photopeak centroid for all the photopeak positions found for each pixel prior to the nonlinearity correction. All pixels have similar trends, but there is significant variation in the relative photopeak positions at each source energy. This indicates that a single fit type should be applicable to all pixels, but the fit parameters will vary on a pixel-by-pixel basis.

It is clear from Figure 8.1 that the peak-hold drop correction has an impact on the nonlinearity of the system. The nonlinearity is more extreme at higher energies after correction. However, the goal of the peak-hold drop correction is not to eliminate the system nonlinearity altogether, but to eliminate the depth dependent nonlinearity introduced by one component of the system. With the data shown thus far, the advantage is not yet obvious.

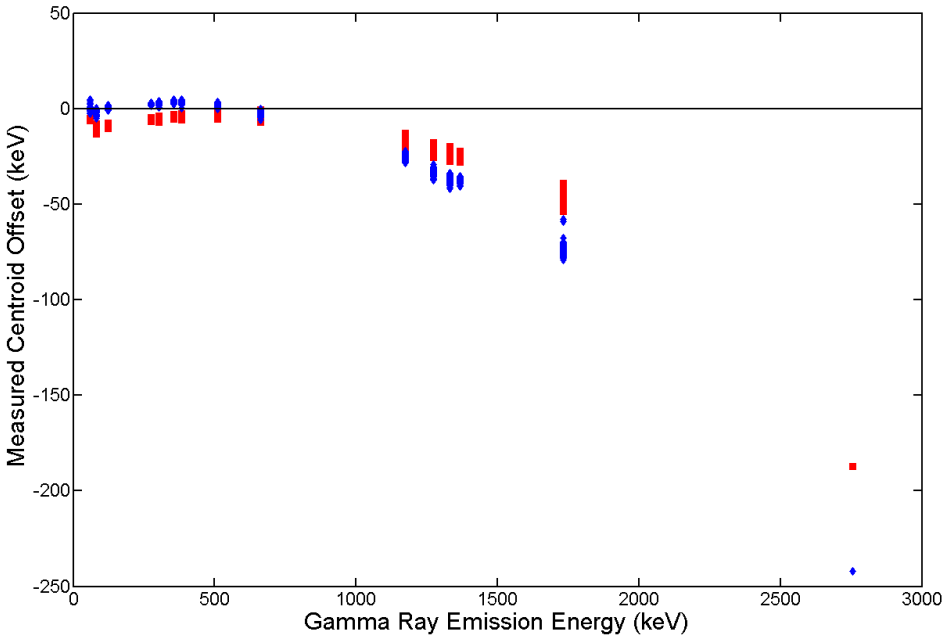

Figure 8.1: Offset between the measured photopeak centroid and the known emission energy for several calibration sources. The red squares show the values before peak-hold drop correction and the blue diamonds show the values after peak-hold drop correction. Negative values indicates that the measured value is smaller than the emission energy. The centroids are plotted for each of the 121 pixels.

8.3.2 Detector-by-Detector Variation in Linearity

Understanding the trend in nonlinear behavior between detectors is useful for developing a calibration algorithm that is well suited for any combination of GMI ASIC and Redlen detector crystal. The data from all pixels are combined for each detector and an overall response is obtained. The results are shown in Figure 8.2 for 16 of the 18 detectors in an array system. Data is only shown for 16 detectors such that the results could be displayed on a 4×4 grid, and the positions of the plots are not directly correlated with position in the array. The single escape peak from Na-24 is difficult to observe amongst single-pixel events, as this event sequence requires two interactions. Thus, few detectors contain data between 1700 keV and 2700 keV.

All of the detectors demonstrate the same behavior discussed in section 8.3.1. The peak-hold drop correction consistently results in greater nonlinearity at higher energies. The overall shape of the nonlinearity, both before and after peak-hold drop correction, is similar between detectors.

8.3.3 Impact of Electronics on Linearity

The system nonlinearity is very similar between different detectors or different pixels of the same detector. In order to take the proper approach to calibration it is important to understand whether this is due to systematic effects in the crystal or the electronics. A review of scientific literature on detector nonlinearity, performed at Pacific Northwest National Lab in 2007, reports that scintillators tend to have show significant nonlinearity in light output while the well known semiconductors, HPGe and silicon, have a near-linear response (46). Work on understanding the true nonlinearity of the CdZnTe material itself has been fairly limited.

A novel coincident measurement using a CdZnTe crystal and a HPGe detector was performed at Kansas State University in order to study the nonlinearity of the CdZnTe material with continuous energy values, and some nonlinearity was reported

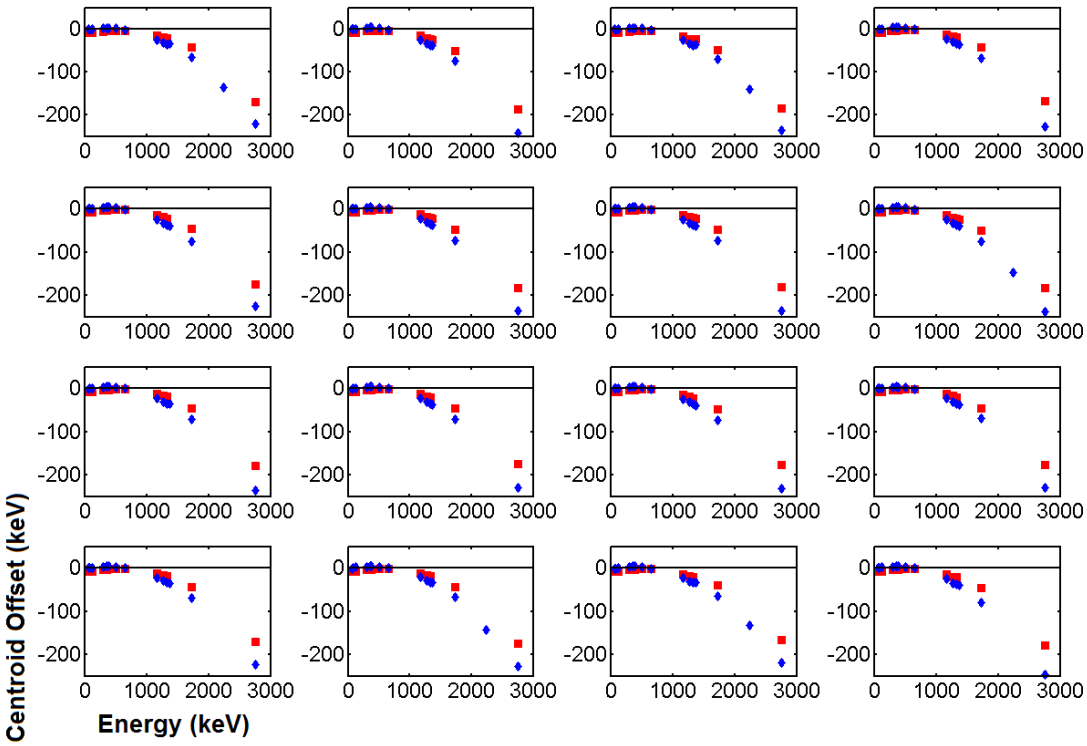

Figure 8.2: Offset of the measured photopeak centroid for 16 detectors in an 18 detector array. The red squares show the values before peak-hold drop correction and the blue diamonds show the values after peak-hold drop correction. Negative values indicate that the measured value is smaller than the emission energy. The data from all pixels are combined to find the overall centroid for each detector.

(47). However, these results should not be directly applied to pixelated detectors, as they were obtained on a Frisch collar device. The use of a Frisch collar results in spatial variation in charge induction that is more severe than the nearly nonexistent spatial resolution. Therefore, it is difficult understand the underlying nonlinearity of a crystal because the spatial distribution of interactions inevitably changes as a function of energy. This is true both for the incident energy, which is typically the case when measuring nonlinearity, and for the escaping energy, in the case of the Kansas State experiment. It is not clear how one could separate the effect of varying charge induction as a function of energy due to the electrode configuration and true nonlinearity in the signal carrier generation, transport, or collection.

In the absence of analogous results from literature, experimental methods are the only option to answer this question. A test pulse can be used to isolate the nonlinearity due to the electronics. In addition to the noise issues with the internal test pulse described in section 7.2.1, it is difficult to know the true pulse amplitude for comparison to the ASIC measurement. These issues can be resolved by splitting the output of an external test pulse generator and simultaneously measuring the pulse height on an oscilloscope and with an ASIC. The results of such an experiment are shown in Figure 8.3, using one channel of one ASIC. Overall the test pulse is well matched with the gamma-ray data, especially for the large photopeak offsets at high energies. Some of the low energy behavior is not exactly matched, so it is possible that some nonlinearity is due to the crystal itself. Regardless, the most important contributor to the system nonlinearity is the electronics.

These results provide critical guidance on how the nonlinearity correction should be performed. The nonlinearity of the preamp should depend only on the amplitude of the preamp signal. Therefore, the calibration algorithm should correct the amplitude as a function of the raw amplitude signal, not the estimated energy after depth correction. In Redlen CdZnTe this is a minor distinction, but in a detector with

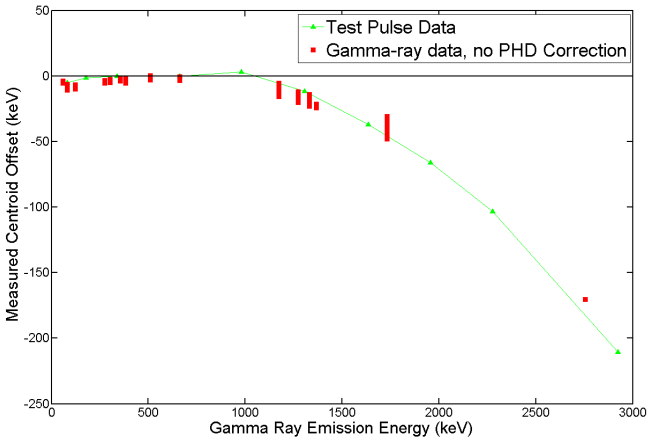

Figure 8.3: Comparison between nonlinearity determined using an external test pulse and nonlinearity determined from gamma-ray data before peak-hold drop correction. The centroids are plotted for each pixel of one detector in an eighteen detector array. The test pulse was injected into a different ASIC then the gamma-ray data. The true test pulse amplitude is measured using an oscilloscope.

severe trapping this would require a fundamental change in the approach, as a single energy value can result from a wide range of preamplifier values.

8.3.4 Functional Fit to Nonlinearity Data

A series of discrete photopeak positions must be converted into a continuous description of the system nonlinearity in order to reconstruct an arbitrary event. Dr. Feng Zhang had spliced together a pixel-by-pixel low energy fit with an overall high energy fit prior to the implementation of a peak-hold drop correction. After implementing peak-hold drop correction it is shown that this technique can be simplified to a single fit across all energies for each pixel.

The results of fitting a fourth order polynomial to the nonlinearity data for each detector is shown in Figure 8.4. Both curves do a good job of capturing the nonlinearity at high energies. Figure 8.5 shows the same data as 8.4, but the plot region is focused on the response below 1 MeV. By studying the detectors that can properly identify the 60 keV line, it is observed that the fitting curve can only correctly capture

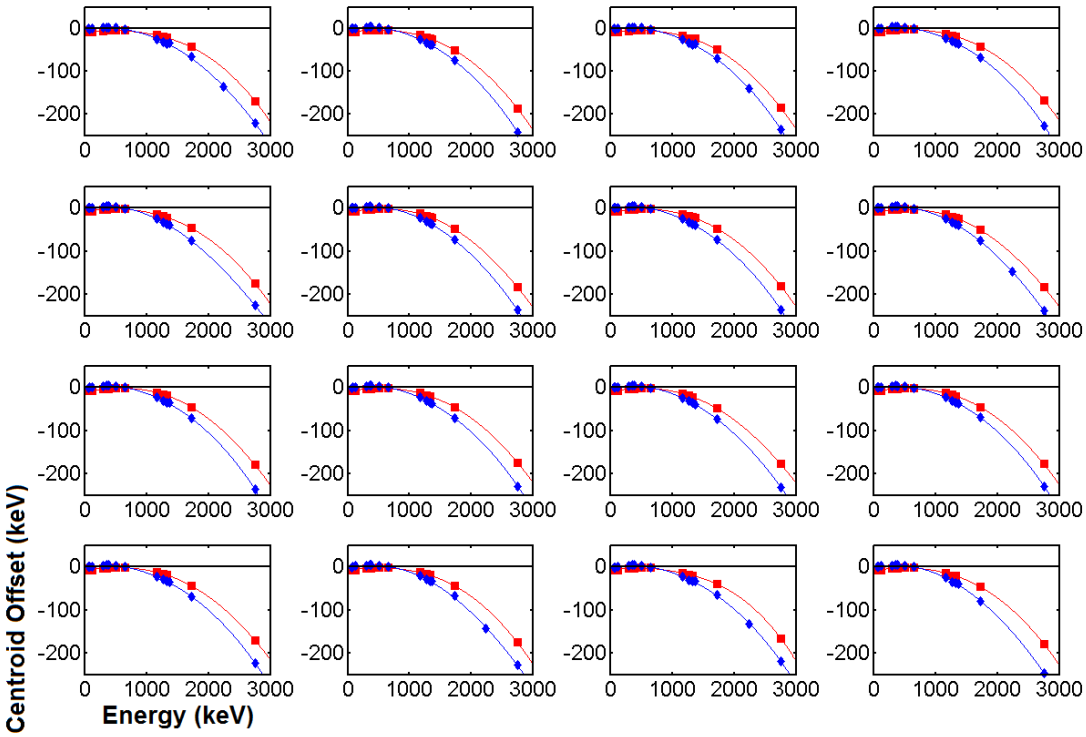

Figure 8.4: The correction curve fit to the nonlinearity data of 16 detectors in an 18 detector array. The red line shows the fit to the data before peak-hold drop correction and the blue line shows the fit to the data after peak-hold drop correction.

the system behavior in that region when the peak-hold drop correction is used. This is because the low energy nonlinearity is much simpler, with respect to the number of changes in the sign of the slope, after peak-hold drop correction. Changing the order of the polynomial fit does not result in significantly better agreement for the data without peak-hold drop correction.

Prior to peak-hold drop correction the nonlinearity is influenced by both the preamplifier response and the peak hold, and the fitting curve must simultaneously capture both behaviors. At the high energies this is not challenging because the peak-hold drop offsets the effect of the preamplifier. However, below 200 keV the response of the peak-hold drop circuit changes rapidly, evident from the information presented in section 7.4.2. This ultimately results in a system response function that is more challenging to calibrate.

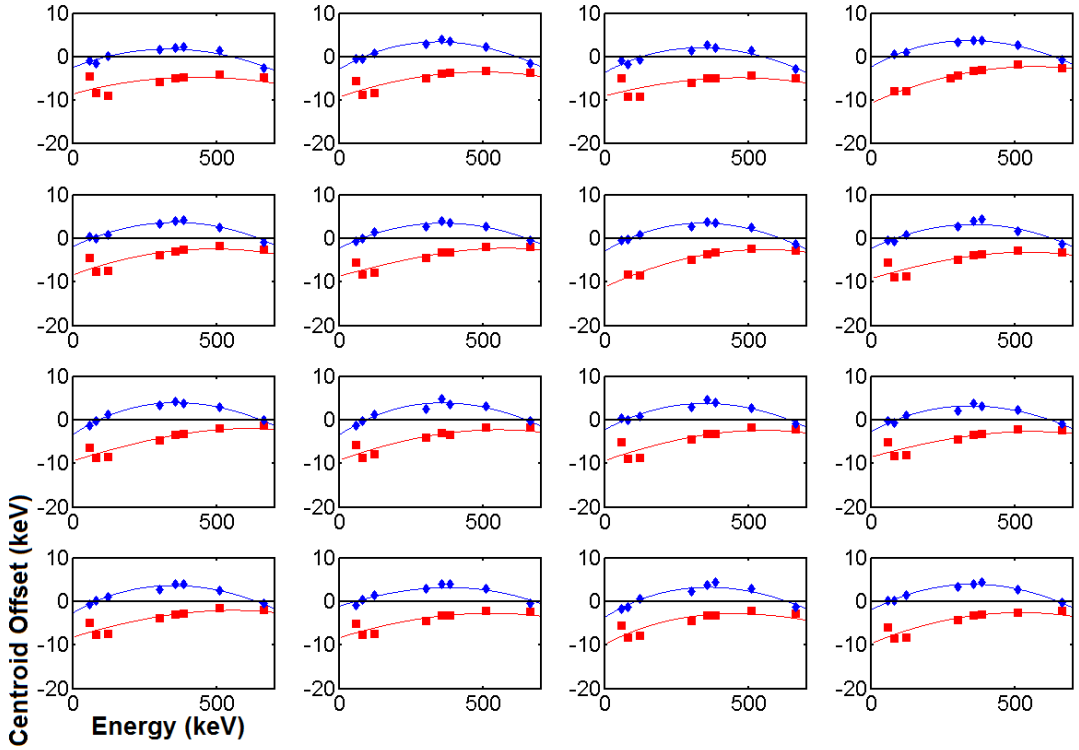

Figure 8.5: The low energy region of the correction curve fit to the nonlinearity data of 16 detectors in an 18 detector array. The red line shows the fit to the data before peak-hold drop correction and the blue line shows the fit to the data after peak-hold drop correction. The correction curve cannot capture the true low energy nonlinearity for the data before peak-hold drop correction.

8.3.5 Nonlinearity in the Total Energy of Multiple-Pixel Events

The nonlinearity results shown thus far are all obtained using data from single-pixel events. In principle, applying the single-pixel correction parameters to each individual energy deposition in a multiple-pixel event should eliminate the nonlinearity. To assess the validity of this statement the photopeak centroid was measured at each calibration energy for the total energy deposited in multiple-pixel events. The results are shown for 2, 3, and 4 pixel events in Figs 8.6, 8.7, and 8.8, respectively.

There are several important trends in the data. The multiple-pixel nonlinearity is reduced after peak-hold drop correction. This is because the single-pixel nonlinearity correction does not completely eliminate the system nonlinearity because the fit is inadequate at low energies and because the depth dependent nonlinear behavior is not corrected at all. Another trend is that the departure from ideal behavior becomes more substantial as the number of pixels summed increases. This is because in a four pixel event the single-pixel nonlinearity correction is applied four times, and if there is some problem, the effects will be summed. If the amplitude and polarity of the departure from linearity is random the effects will sum in quadrature for multiple-pixel events.

After peak-hold drop correction the nonlinearity of multiple-pixel events is greatly reduced. Some detectors do not show any statistically significant departure from linearity for multiple-pixel events. However, there are some detectors that still show significant nonlinearity even after peak-hold drop correction. The trend is always toward smaller-then-expected amplitudes at higher energies. This could be caused by a variety of factors, such as the undercorrection of the weighting potential crosstalk or a systematic bias toward depths closer to the anode due to the uncorrected nonlinearity of the cathode signal. The most likely candidate is the same explanation as for the data before peak-hold drop correction: incomplete correction of the single-pixel nonlinearity. If the peak-hold drop correction algorithm does not work exactly as

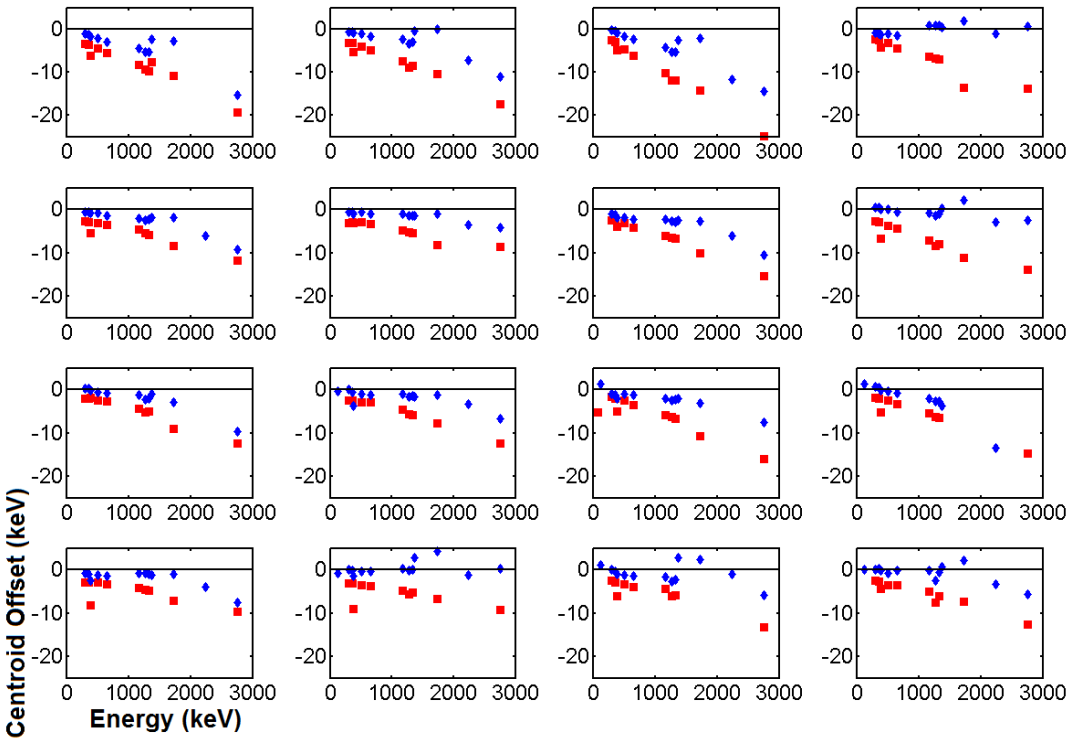

Figure 8.6: Nonlinearity of the total energy of two-pixel events. The red squares show the values before peak-hold drop correction and the blue diamonds show the values after peak-hold drop correction.

expected or if the polynomial expansion does not perfectly capture the true behavior of the system then some nonlinearity will remain uncorrected. If the data for the 60, 81, and 122 keV lines in Figure 8.5 are carefully examined, it is seen that the detectors with the worst multiple-pixel nonlinearity also show low energy single-pixel nonlinearity similar in shape to the results before peak-hold drop correction. This indicates that the peak-hold drop effect is not completely eliminated for these detectors and the residual effect becomes apparent in multiple-interaction events. It is also noteworthy that the detectors with the worse multiple-pixel nonlinearity also tend to have a weak field in the central region that can cause problems in the depth reconstruction from drift time.

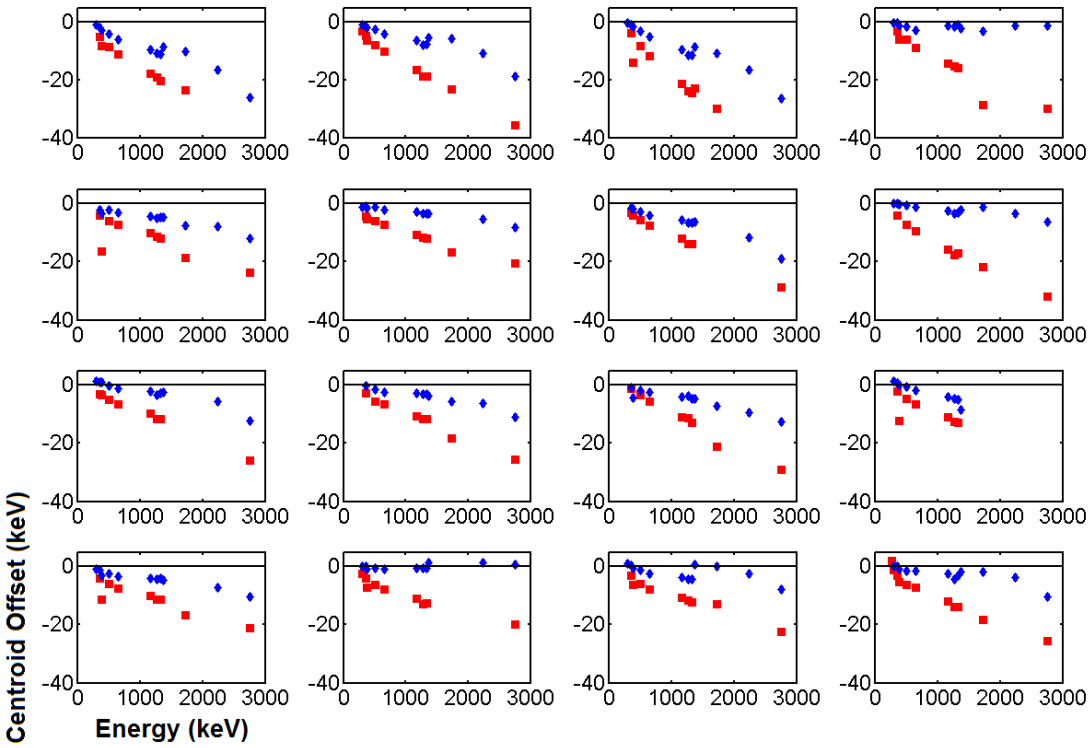

Figure 8.7: Nonlinearity of the total energy of three-pixel events. The red squares show the values before peak-hold drop correction and the blue diamonds show the values after peak-hold drop correction.

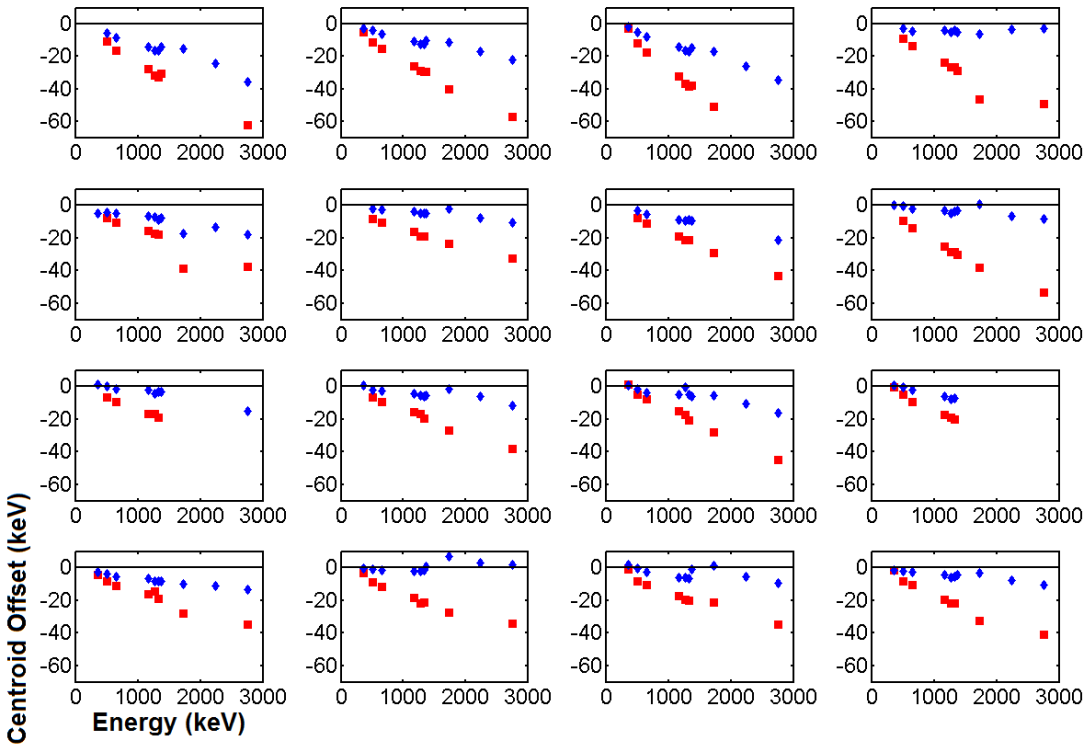

Figure 8.8: Nonlinearity of the total energy of four-pixel events. The red squares show the values before peak-hold drop correction and the blue diamonds show the values after peak-hold drop correction.

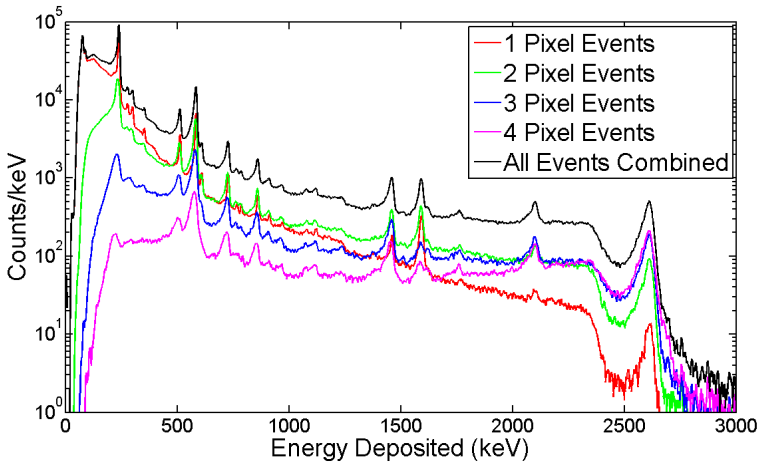

Figure 8.9: Th-228 spectrum measured by an 18 detector array.

8.3.6 Response of an 18 Detector Array to Th-228

A Th-228 source is a useful tool for checking the accuracy of the nonlinearity correction. The energy resolution at 2614 keV will depend on the calibration of the system nonlinearity. Prior to nonlinearity correction it is often difficult to observe a peak at 2614 when combining all events from all detectors. After calibration the spectra shown in Figure 8.9 is generated. All of the photopeak positions are well aligned for all event types. This shows the device has excellent spectroscopic capability across the full dynamic range, but only after effective calibration of the system nonlinearity.

The 2614 keV peak has a high energy tail, which is pronounced when the number of pixels that collect charge increases. This is likely due to an event that induces a large transient signal in a side-neighbor pixel. The signal on the neighbor pixel will initially be positive and will become negative when the charge is collected. The peak-hold circuit can pick off the positive component, resulting in an overestimate of the total energy deposited. A system such as the digital ASIC can overcome this problem analyzing the preamplifier waveform.

8.4 Measured Data Using the BNL ASIC

The H3D ASIC from BNL provides an excellent opportunity to verify the conclusions drawn from GMI ASIC data, namely that the nonlinearity is electronic and that the multiple-pixel event nonlinearity correction is needed due to residual nonlinearity that was not corrected by the one pixel data. My work is the data processing and analysis. All BNL ASIC data presented in this chapter was acquired by Dr. Feng Zhang using a 6 cm^3 detector from eV Products. Data was taken with Am-241, Co-57, Ba-133, Na-22, Cs-137, Eu-152, Co-60, and Th-228 sources.

8.4.1 Single-Pixel Nonlinearity Comparison

The photopeak positions measured from single-pixel events for all sources are shown in Figure 8.10 for data from the BNL and GMI ASICs. The most remarkable difference is that the sign of the nonlinearity is reversed for the BNL ASIC, such that photopeak positions above 1 MeV are consistently overestimated. This is further proof that the dominant factor in device nonlinearity is the electronics.

The magnitude of the nonlinearity is smaller in the BNL ASIC, approximately by a factor of five at energies above 2 MeV. Another important feature of the BNL ASIC data is the pixel-by-pixel determination of the 2614 keV photopeak position. This is possible because more counts are available than for the GMI data and because the energy reconstruction is better, providing a narrower peak to identify in each channel. Another reason why the BNL ASIC can get more single-pixel counts is because it can discriminate more effectively against false transients in the neighbor pixels, which reduce the fraction of single-pixel events. Ultimately, the benefit of performing a pixel-by-pixel nonlinearity correction at the 2614 keV line is remarkable. Figure 8.11 shows that energy resolution below 0.4% at 2614 keV is possible for single-pixel events. The energy resolution was greater than 0.8% when measured from the same data without a pixel-by-pixel correction at high energies (44).

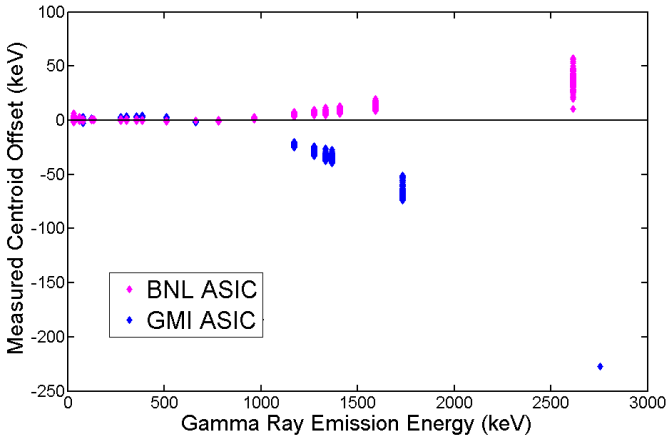

Figure 8.10: Comparison between the nonlinearity of each channel of a detector read out with a BNL ASIC, shown in pink, and for a detector read out with a GMI ASIC, shown in blue. The GMI data is shown after peak-hold drop correction.

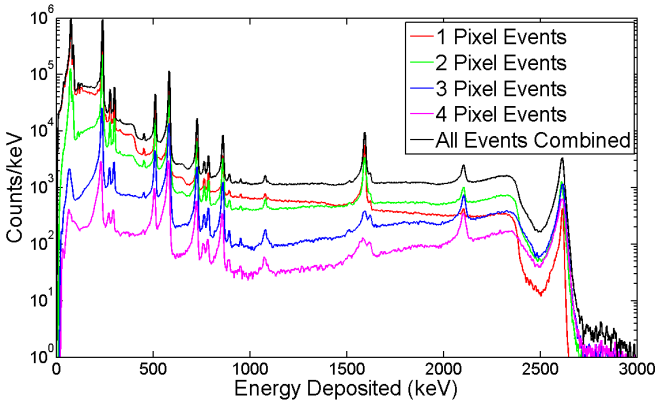

Figure 8.11: Th-228 spectrum measured using the BNL ASIC. The energy resolution is 0.36% at 2614 keV for single-pixel events.

8.4.2 Multiple-Pixel Nonlinearity Correction

The nonlinearity of the BNL ASIC for multiple-pixel events is much smaller than for the GMI ASIC. Figure 8.12 shows the photopeak positions for 2, 3, and 4 pixel events. While all photopeaks for any number of pixels triggered are within 10 keV of expectation, a definite trend is apparent. Larger gamma-ray energies have a more significant departure from the expected energy, with the effect becoming more severe as the number of pixels triggered increases. However, the photopeaks are, once again, measured at a value greater than expected for the BNL ASIC while the GMI ASIC measured them to be too small. This eliminates any cause for the observed behavior that cannot explain a shift in either direction, such as undercorrection by the weighting potential crosstalk algorithm. The incomplete correction of the single-pixel nonlinearity is still a strong argument to explain the residual nonlinearity observed in the multiple-pixel events.

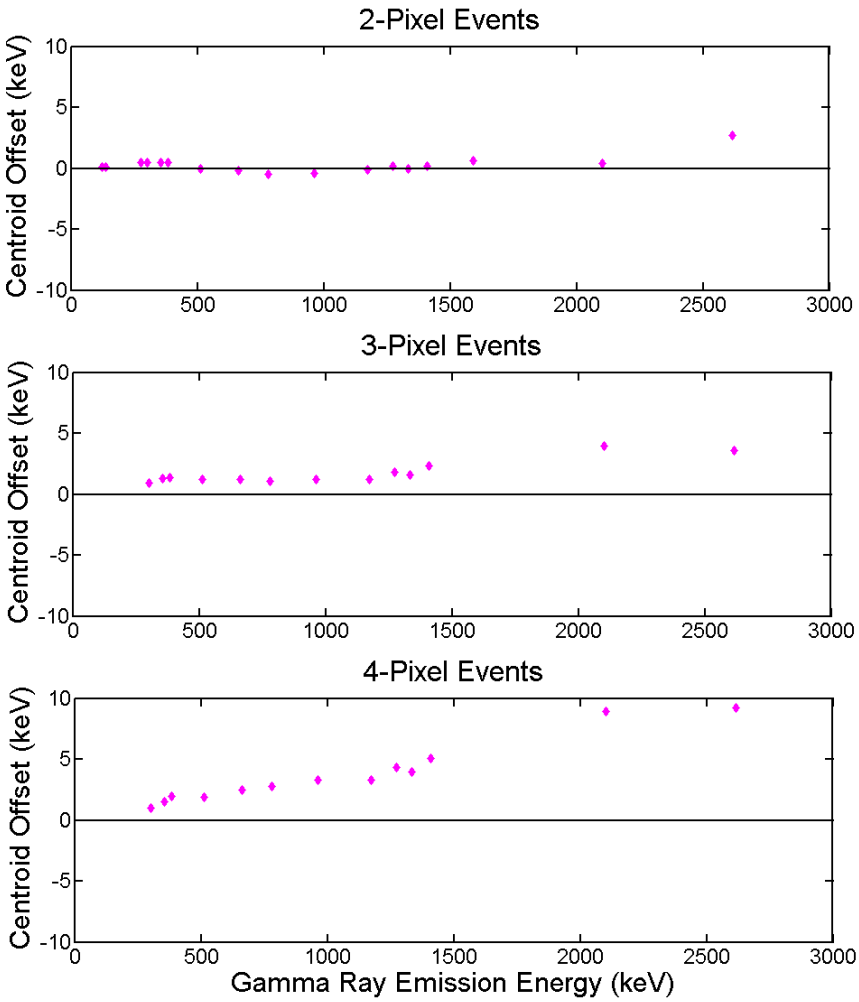

Figure 8.12: Nonlinearity of the total energy of multiple-pixel events in the BNL ASIC. 2-pixel events are shown on top, 3-pixel events in the middle, and 4-pixel events on the bottom.

CHAPTER IX

Common Detector Problems

9.1 Summary of Material and Detector Evaluation Methods

Since the discovery of CdZnTe as a gamma-ray detector (4), significant effort has been spent identifying possible problems and limitations of the material. Early on, effort was focused on characterizing the defects in CdZnTe and understanding their impact. Techniques such as deep level transient spectroscopy and photo-induced current transient spectroscopy examine the signal from the device as it is heated from below 100 K to beyond room temperature to determine the concentration and energy levels of carrier traps in the semiconductor (48). Electron paramagnetic resonance is also used to characterize the impurities that cause the shallow and deep levels (49). Cathodoluminescence is used to map out defects by striking a region of the semiconductor with electrons and measuring the resulting photon emissions (50).

There are many other aspects of detector fabrication to analyze besides the concentration and nature of the defect levels. Contact fabrication has also been identified as an important consideration in CdZnTe detectors and efforts have been made to minimize the leakage current by surface passivation (51). CdZnTe detectors are known to have non-uniform electric field in some samples when measured with the Pockels electro-optic effect (52). During the growth process, it is typical to form small pockets of pure tellurium, known as tellurium inclusions, which can be identified by

measuring the transmission of infrared light through the material (53).

Ultimately, the most important factor that effects the performance of a gamma-ray detector based on single polarity charge sensing is the uniformity of electron transport through the bulk of the material. Efforts have been made to correlate the presence of material defects, especially tellurium inclusions, to the charge transport properties. One technique is to irradiate the cathode surface with a finely collimated alpha beam to determine the spatial dependence of the charge transport properties, which are compared to the infrared transmission data (54). A similar measurement has been performed using an even more finely collimated beam (10μm $\times$ 10μm) of 30-85 keV photons generated by the National Synchrotron Light Source, which provided much finer spatial resolution (55).

Ideally the electrons will drift in a straight line from the cathode to the anode, but studies at Brookhaven National Laboratory have shown this is not always the case (56). These studies were conducted by irradiating the cathode surface of a device with a pixelated anode using a finely collimated X-ray beam. It was found that some pixels could collect charge even when the free electrons were created in a different lateral position. This effect will degrade the imaging performance of a device.

The purpose of the work presented in this chapter is to study the operational considerations of a fully fabricated pixelated device. For example, the stability of the system response with respect to time and temperature will be discussed along with the generation of false system triggers due to detector fabrication issues. Ultimately, the material analysis techniques described in this section may explain the underlying causes of these problems. However, the focus of this chapter will be practical techniques for overcoming these issues.

9.2 Cathode Noise Triggers

The cathode timing circuit will often trigger erroneously. This is typically due to one of two causes; instability of the cathode electrode when high voltage is applied or electromagnetic intereference from an external source. Some detectors from Redlen Technologies, Orbotech, Yinnel Tech, and eV Products have been found to be unstable at high bias and the degree of the problem varies on a detector-by-detector basis. The susceptibility to interference is completely independent of the detector; it is a function of the electronics and the quality of the grounding and shielding of the metallic box that houses the detectors. Minimizing the electrical resistance between all sides of the detector box is found to improve the resitance to interference. The cathode is more susceptible to interference than the pixels due to the greater surface area of the electrode.

Ideally, detectors can be selected that do not generate erroneous cathode triggers and the detector system can be built to resist interference. However, in some circumstances these triggers are unavoidable. For these situations a means of overcoming these erroneous triggers is necessary.

The BNL ASIC is much more resistant to this problem by design then the GMI ASIC. A cathode trigger will always initialize readout of the GMI ASIC while the BNL ASIC will only read out when an anode pixel triggers. If the cathode triggers in the BNL ASIC the system will wait for an anode trigger, if it does not come within a few microseconds the cathode timing circuit will reset and the system is ready for the next event. When the erroneous trigger frequency is sufficiently large, near the order of megahertz, then most of the true radiation interactions will coincide with a false cathode trigger and the cathode timing information will be useless. This is still a significant improvement over the GMI ASIC which becomes paralyzed by false cathode triggers occurring at kilohertz frequencies.

When the erroneous cathode trigger rate becomes too high in the GMI ASIC

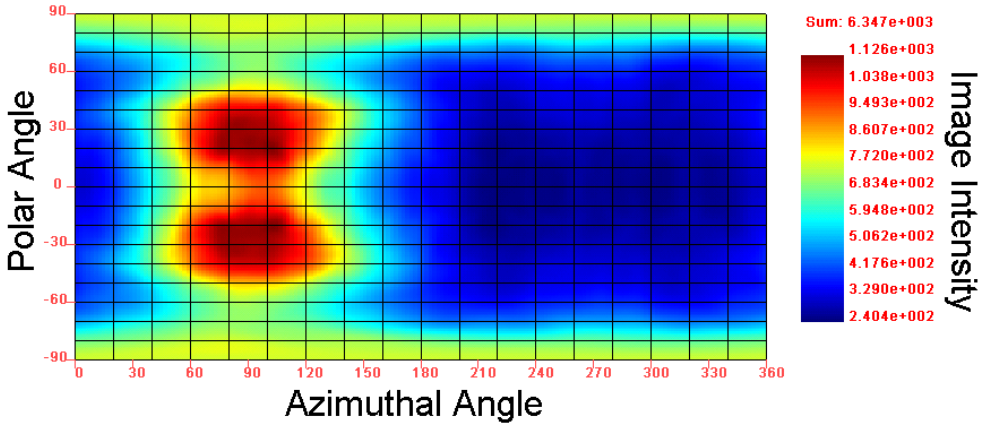

Figure 9.1: The Compton image from 662 keV photopeak events from a Cs-137 source using the GMI ASIC with the cathode trigger disabled. The original depth reconstruction technique is used. Figure provided by Dr. Weiyi Wang.

the cathode timing circuit must be disabled to prevent the readout system from becoming paralyzed. The depth of interaction can still be properly reconstructed for multiple-pixel events without cathode timing information. Given the relative time difference between anode timing triggers and the overall ratio of cathode to anode amplitude signals the expected cathode trigger time can be reconstructed. Collimator measurements, similar to those described in Chapter VI are used to successfully validate the depth reconstruction without the cathode timing trigger. Furthermore, interaction energy and position data are passed to an image reconstruction before and after implementing the disabled cathode trigger correction technique. Dr. Weiyi Wang created the Compton image for both scenarios, with results shown in Figure 9.1 and Figure 9.2.

When the cathode timing circuit must be disabled, in the case of the GMI ASIC, or becomes unreliable, in the case of the BNL ASIC, some information is inevitably lost. The cathode timing information can be used to reject chance coincidence events, as there will be disagreement between the average depth reconstructed from drift time and the overall cathode-to-anode ratio. Without cathode timing information it is difficult to discriminate against chance coincidence, limiting the utility of the device

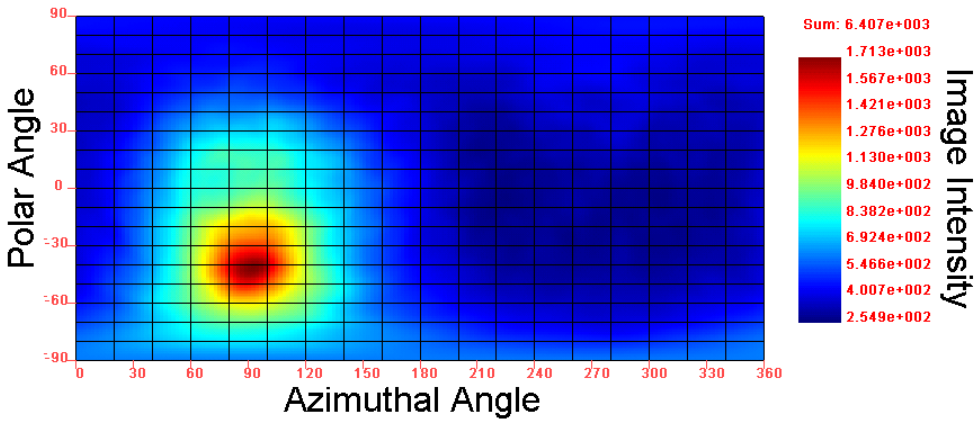

Figure 9.2: The Compton image from 662 keV photopeak events from a Cs-137 source using the GMI ASIC with the cathode trigger disabled. The new depth reconstruction technique based on estimating the cathode trigger time from the cathode amplitude signal is used. Figure provided by Dr. Weiyi Wang.

at very high count rates.

In the case when the cathode signal has consistent large magnitude fluctuations at a frequency capable of interfering with both the timing circuit, which typically uses a 100 ns shaping time, and the amplitude signal, which typically a 1μs shaping time, then depth reconstruction becomes impossible with any readout scheme or ASIC.

9.3 Anode Noise Triggers

The anode pixels are also capable of generating erroneous triggers. In general they are much less susceptible to external interference then the cathode. However, due to their close proximity to the negatively biased steering grid (see Figure 2.1), the stability of each anode signal is highly dependent on the anode fabrication process. In a worst case scenario there is insufficient resistance between the grid and one or more pixels, making it impossible to apply bias to the grid while keeping the pixels near the electrical ground. These pixels cannot be used and must be disconnected from the readout electronics.

A more common occurrence is that one or more pixels in a detector will generate a

significant number of erroneous system triggers even though the grid-pixel resistance is high enough to supply the proper grid bias. Some pixels will be unstable without any bias applied, a few will become unstable when the cathode bias is applied, and many become unstable when the grid bias is applied. Regardless of the nature and cause of the instability, the trigger signal from these pixels must be disabled in order to operate the system, resulting in a loss of detector efficiency.

In laboratory situations, especially for single detector systems, it is practical to manually disable these bad pixels on an individual basis once they begin generating erroneous triggers. However, whether or not a pixel generates false triggers can vary with temperature and time. Thus, in the case of an eighteen detector array system, which has more than two thousand independent pixels, the process of disabling bad pixels must be done in an automated fashion.

An algorithm to identify and disable pixels that generate false triggers has been developed. If a pixel is responsible for a large number of triggers, representing an unreasonable fraction of the overall number of triggers across multiple readout cycles it is identified as bad and disabled. This technique is able to identify a bad pixel within a few seconds. There is currently no method to automatically re-enable a pixel that stabilizes, but the user can reset all pixels and the system will quickly disable only the pixels that are actively generating false triggers. In the most recent array system there are typically fewer than ten out of 2178 pixels disabled in this fashion, even after weeks of operation.

9.4 Drift Velocity Uniformity

Ideally a detector will have a uniform electric field throughout the bulk such that electrons will drift at a constant velocity. Fortunately, as discussed in section 3.3, a non-uniform drift velocity through the bulk can be corrected by proper calibration. Nevertheless these calibration techniques do have their limitations, which will be

discussed in this section.

When a system trigger occurs there is a limited time window until the system must read out. Extending this window increases the probability of chance coincidence and places a greater demand on the hold delay circuitry. The time between the first system trigger and readout is called the hold-delay time. If the drift time from cathode to anode is longer than the hold-delay time then timing information will inevitably be lost. Given a fixed applied voltage the shortest possible drift time from cathode to anode will occur if the drift velocity is uniform. Severe nonuniformity of the electric field or drift velocity will push the maximum drift time beyond the hold-delay time.

Figure 9.3 shows the relationship between the drift time and CAR for each pixel in one detector. The pixels with the most severe nonuniformity, shown in the bottom left corner, do not generate valid timing data for the depths near the cathode. This is due to drift times that are longer than the hold-delay time.

Another possible complication due to nonuniform drift velocity is the loss of a unique relationship between drift time and depth. This can manifest itself in one of two ways. The most severe scenario occurs when the nonuniformity of the drift velocity varies on a scale finer than the lateral position resolution of the device, typically limited by the pixel pitch. In this case sub-pixel position information is required to correctly reconstruct the depth from drift time. The second scenario is inevitable: the regions of the device that have a lower drift velocity will have a greater timing jitter. This is because the cathode signal rises more slowly in these low drift velocity regions. At lower energies the timing circuit will not trigger until the charge reaches a higher drift velocity region, which causes multiple depths to report the same timing value.

Figure 9.4 shows the timing uncertainty as a function of depth for each pixel in the same detector shown in Figure 9.3. The timing uncertainty is systematically larger in the central depths, which is well correlated with the regions of the smallest

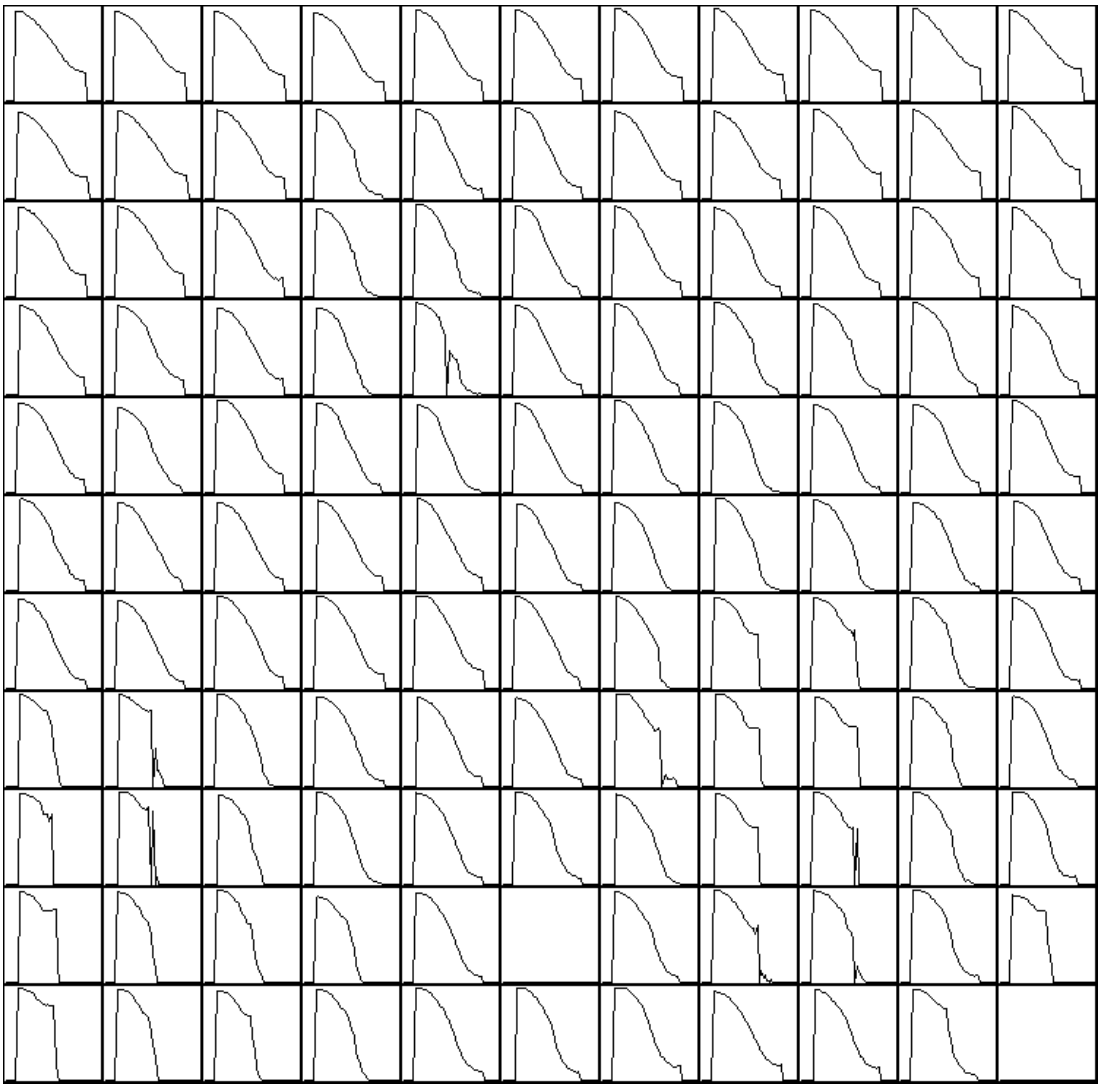

Figure 9.3: The ASIC timing value (vertical axis, longer drift times are associated with smaller ASIC timing values) versus the CAR (horizontal axis, the anode is on the left and cathode is on the right) for each pixel in detector 4R36. Two anode pixels had to be disabled, as discussed in section 9.3.

drift velocity. The pixels in the upper right corner that have the most uniform drift velocity also have the smallest timing uncertainty.

9.5 Gain Deficit

An unexpected variation in the uncorrected photopeak position between each pixel has been observed in many detectors. We use the term gain deficit to describe this phenomenon. In principle, the photopeak position should be determined primarily by the electronic gain of each channel and, of course, the energy of the source. Electron trapping will result in a broad peak prior to depth correction, but the high energy edge should not change drastically between pixels, as this will be dominated by anode side events where trapping is minimal. However, it is often observed, especially in Redlen detectors, that the photopeak positions vary well beyond expectation. In the earlier detectors from Redlen the photopeak of some pixels could occur at half the expected amplitude, while in later detectors this deficit is observed on the order of 10% or less.

Figure 9.5 shows the photopeak position for each pixel in a detector from Redlen that has relatively minor gain deficit. This data is taken with the GMI ASIC. In this system the variation in electronic gain is known to be on the order of 1%, based on measurements with excellent detectors. Thus, the variations observed in Figure 9.5 are beyond the expectations from the electronics and are repeatable when a different ASIC chip is used. This effect can be explained by a very small capacitance between the detector surface and the anode pixel, or, by an electric field that slows the electrons when they near the pixel. It cannot be explained by bulk effects such as trapping or detrapping, as these would be expected to broaden the photopeak and demonstrate some degree depth dependence.

For the most part the effect of gain deficit is correctable: the gain of each pixel is calibrated indirectly through the depth dependent energy calibration described in

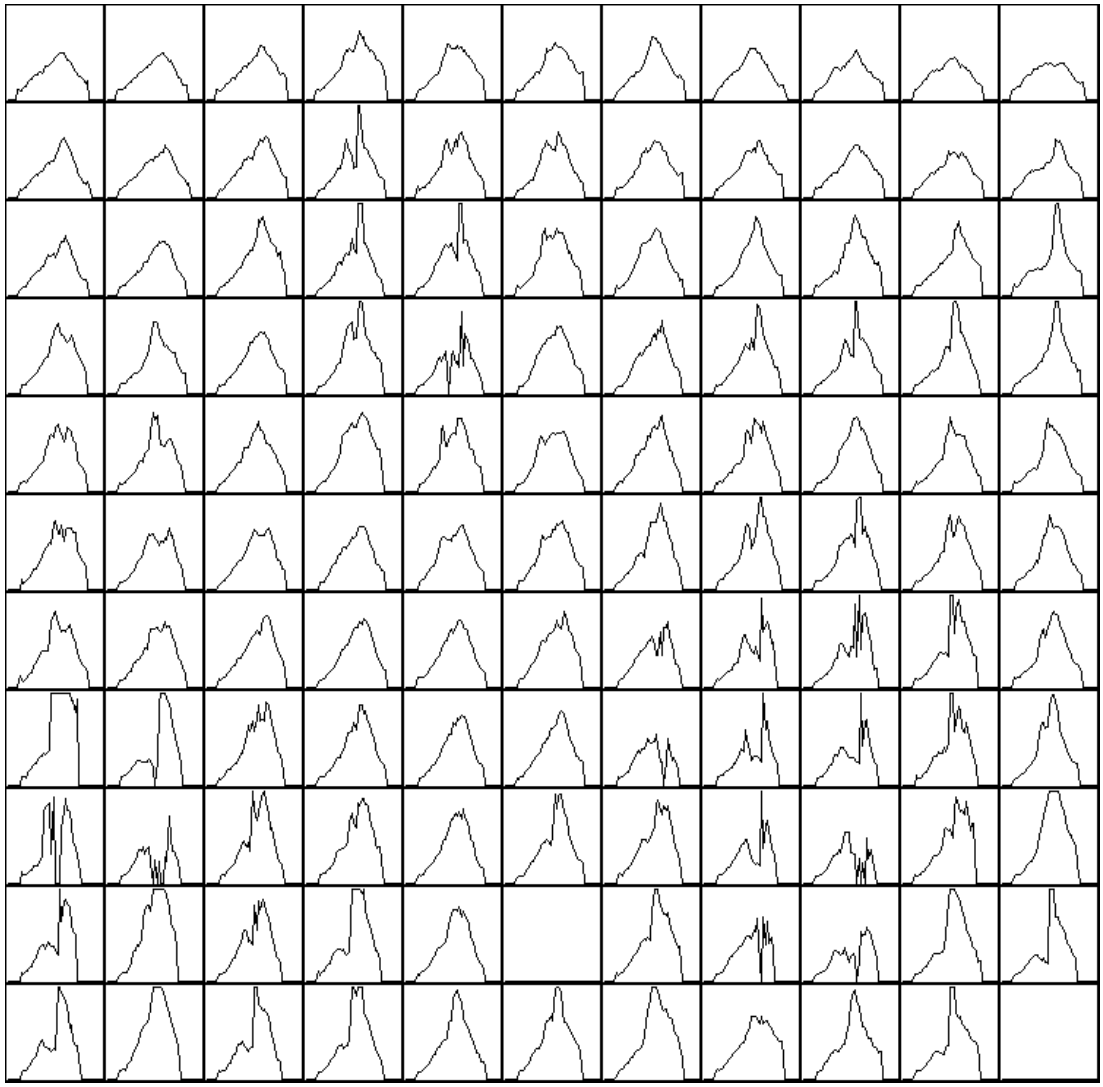

Figure 9.4: The uncertainty in the ASIC timing (vertical axis) versus the CAR (horizontal axis, the anode is on the left and cathode is on the right) for each pixel in detector 4R36. Two anode pixels had to be disabled, as discussed in section 9.3.

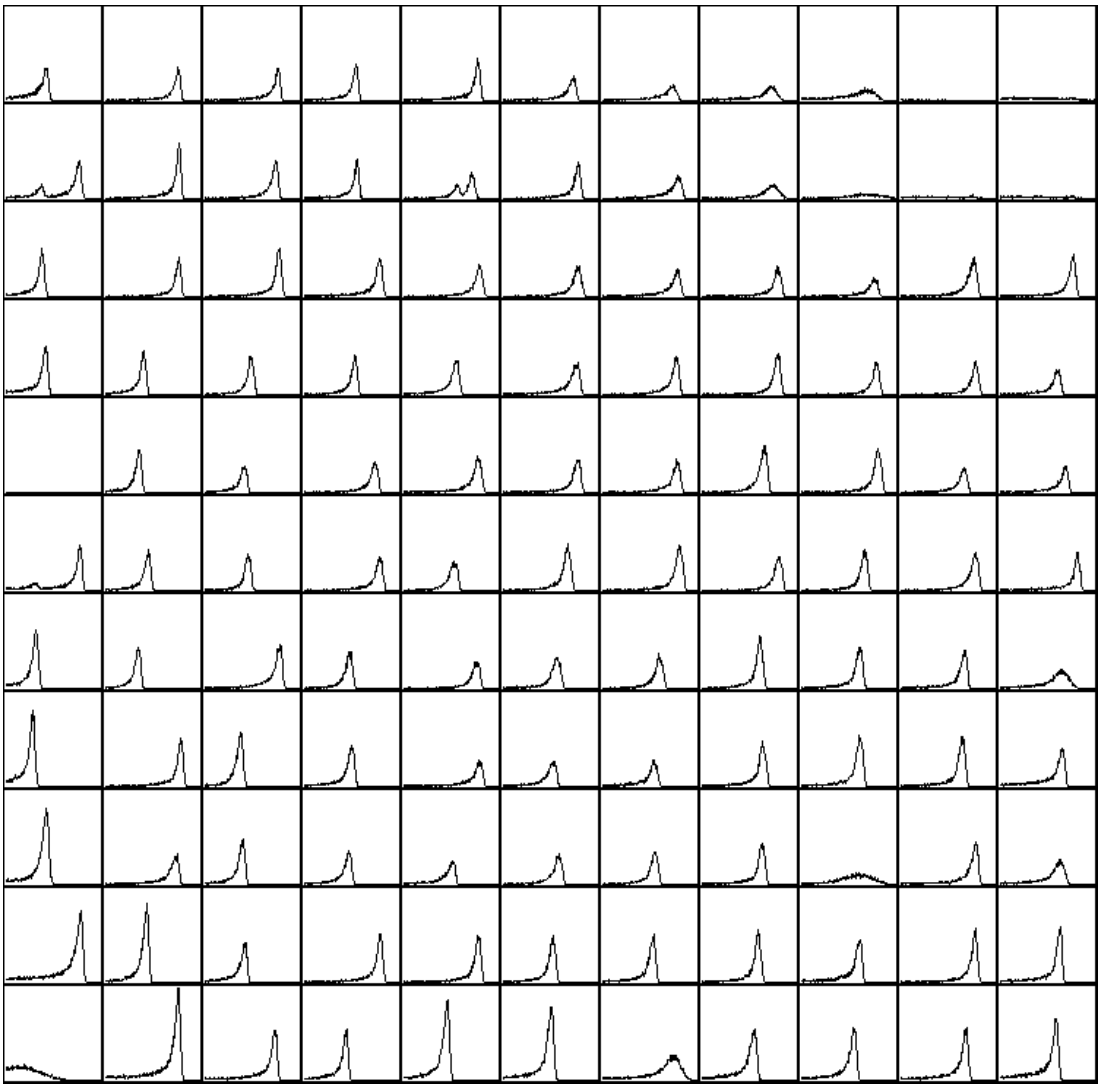

Figure 9.5: The photopeak region of the raw spectrum when a detector with gain deficit is irradiated with a Cs-137 source. The photopeak position varies significantly between each pixel.

section 3.2.2. However, gain deficit degrades the signal-to-noise ratio, as the signal is smaller while the electronic noise remains constant. Furthermore, a single anode TAW calibration cannot be applied to all pixels when they have varying degrees of gain deficit.

The most problematic complications occur when the gain deficit is not constant with respect to time. In this case the problem is uncorrectable. A double peak is observed in a few pixels in Figure 9.5, likely due to intermittent gain deficit. This problem will be discussed in greater detail in Section 9.7.

9.6 Temperature Response

The fact that semiconductor properties will change as a function of temperature is a widely accepted fact (16). In our lab we observe that our devices are highly sensitive to temperature; at one point we had inadequate air conditioning and could only acquire the best energy resolution values in the winter time. To better understand the influence of temperature a refrigerator is used. The goal is to determine how the the device will respond when exposed to the range of ambient temperatures that we would expect to experience during field operation. For this reason the entire detector system is cooled, including the readout electronics, and the experimental temperature range is less than 10 °C.

The summary of the results for seven different experiments is shown in Figure 9.6. A full system calibration is performed at each temperature to eliminate the impact of calibration bias. Three important conclusions are drawn: cooling the detectors slightly below room temperature generally improves energy resolution; the raw photopeak width decreases at lower temperatures; and the mobility increases with decreasing temperature.

The energy resolution improvement can be explained, in part, by a decrease in the electronic noise, which was found to be sensitive to system temperature. Some of this

Detector ID	4E3	4R30	4R30	4R35	4R36	4O4d	1C35
Manufacturer	eV	Redlen	Redlen	Redlen	Redlen	Orbo.	Constel.
Material	CdZnTe	CdZnTe	CdZnTe	CdZnTe	CdZnTe	CdZnTe	HgI_2
Experimental Settings	**Experimental Settings**						
ASIC	BNL V2	BNL V2	GMI 2.3	GMI 2.3	GMI 2.3	GMI 2.3	GMI 3.2
Cathode Bias (-V)	3000	3000	3000	3000	3000	2500	3000
High Ambient Temp (°F)	74	74	74	74	74	74	74
Low Ambient Temp (°F)	53	53	68	63	63	63	56
Overall Performance	**Overall Performance**						
Corrected FWHM Hot (@662keV)	0.59%	0.70%	0.91%	1.06%	1.14%	2.20%	1.37%
Corrected FWHM Cool (@662keV)	0.52%	0.62%	0.82%	1.04%	0.99%	1.61%	1.11%
Raw FWHM Hot (@662keV)	4.50%	3.82%	1.76%	2.69%	2.78%	13.38%	2.59%
Raw FWHM Cool (@662keV)	4.25%	3.54%	1.66%	2.65%	2.65%	11.21%	2.47%
Drift Time and Trapping	**Drift Time and Trapping**						
Drift Velocity Hot (cm/µs)	1.93	1.36	1.39	1.01	0.98	1.37	0.45
Drift Velocity Cool (cm/µs)	2.19	1.41	1.42	1.10	1.03	1.42	0.57

Figure 9.6: Summary of test results at different ambient temperatures.

improvement may come from decreased noise due to the grid, as the leakage current between the pixels and the grid decreases with temperature. The improvement could also be due to the change in the material properties.

The fact that the raw photopeak FWHM improves at lower temperatures is likely due to an increase in the electron mean free path or a decrease in the detrapping time. The dependence of the photopeak position on depth is found to decrease at lower temperatures, indicating that less charge is trapped or the charge that is trapped was allowed to detrap within the shaping time of the system.

The most important change is the mobility. A change in the electron mobility with temperature for CdZnTe has already been demonstrated by others across a wide temperature range (57). The fact that the mobility is so sensitive to temperature will cause problems in both the depth and the energy reconstruction of each event, degrading the energy and the imaging resolution. This effect is believed to be primarily due to a change in the material properties, not the readout electronics, as the timing value for each channel associated with the hold delay time change by less than 1% across the temperature range.

The photopeak and baseline position also change as a function of temperature. This is likely due, at least in part, to the response of the electronics. This represents a major problem with respect to the practical operation of the device.

These studies provide clear evidence that the system should be maintained at a constant temperature. A peltier device is used in the current eighteen detector array system to keep the ASICs and detectors near room temperature. Future versions of the system will include feedback from temperature sensors to keep the temperature constant by modifying the current to the peltier device. The question still remains of which temperature is the ideal operating condition. Cooling the system below the ambient temperature has the potential to improve energy resolution, but will require more power and greater effort must be taken to dry and seal the air around the detector to prevent condensation on the detector and electronics.

One important conclusion is that some detectors respond very poorly to heating above room temperature. The leakage current between the pixels and grid may increase sharply, degrading the energy resolution by a factor of two for a temperature increase of 10 °C in one sample. Furthermore, there is concern that long term operation under these conditions will cause permanent damage to the detectors. For now the target operating temperature is in the range of 20 to 25 °C in order to minimize the chance of condensation, limit the power consumption of the cooling system, and ensure the long term stability of the detectors.

9.7 Short Term Gain Variation

The most problematic situation is if the calibration parameters do not remain constant over a relatively short time period, on the order of days. In this scenario proper calibration is impossible, as the system is changing on the same time scale as the acquisition time for the calibration itself. As soon as a new calibration becomes available it would immediately become out of date.

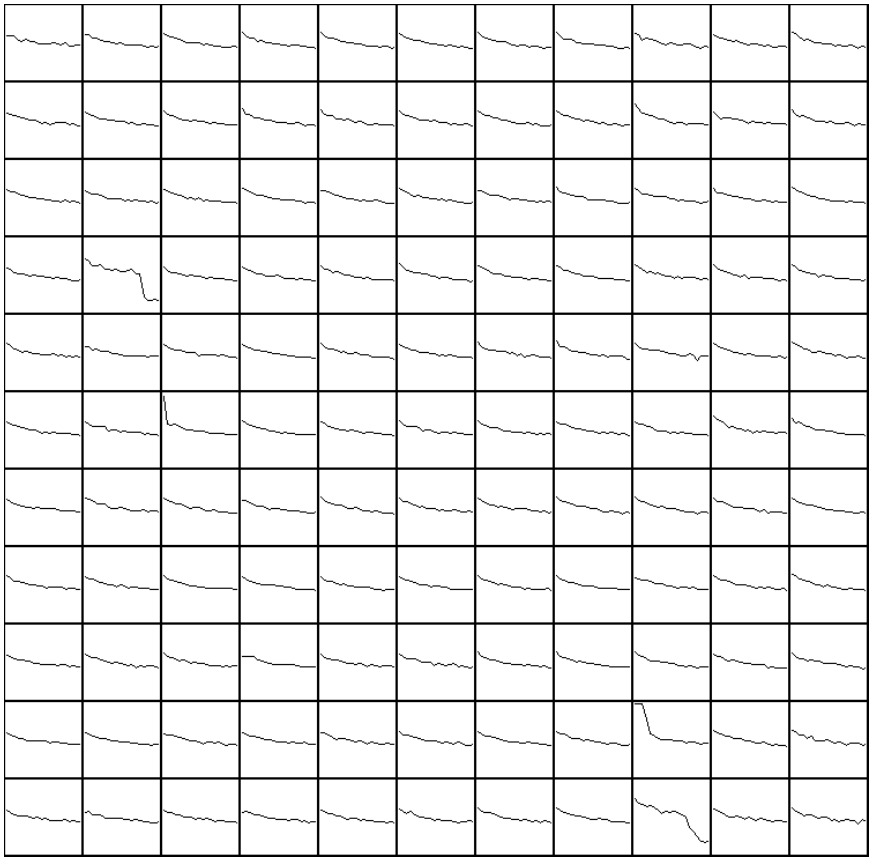

Figure 9.7: The photopeak centroid position (vertical axis, from 650 keV to 675 keV) in each pixel of detector 4R76 as a function of time (horizontal axis). The total time elapsed for this experiment was one day. The photopeak position is found to decrease over time for all pixels.

This behavior is observed in CdZnTe material. It typically manifests itself in one of two possible manners. The first possibility is a change in the bulk material or near the cathode surface such that all pixels show similar behavior. Figure 9.7 shows the centroid as a function of time for each pixel in detector 4R76 during its first day at bias. All of the pixels show a trend toward a lower centroid amplitude over time. Furthermore, the rate of change reduces over time. This behavior is observed in a fraction of the detectors tested at the University of Michigan and the centroids typically stabilize after about two days. While it is possible to calibrate to the stable behavior, when the system is powered down and back up there will likely be another transition period with poor performance.

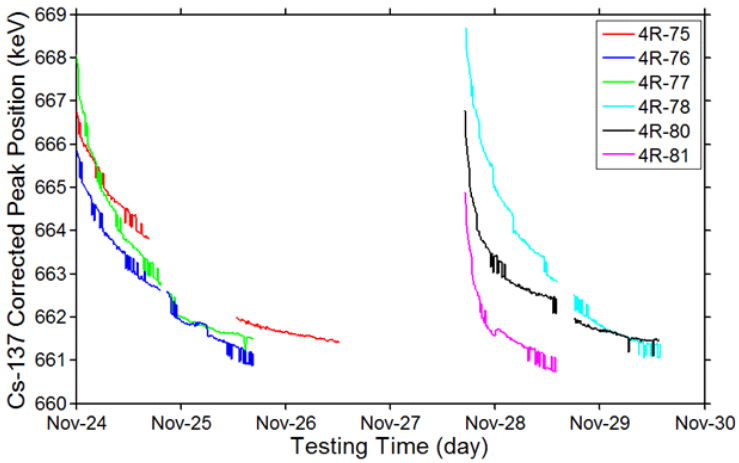

Figure 9.8: The photopeak centroid position over time for several detectors with a gain drift problem. The centroid position for each detector is calibrated to the final data, not the initial data.

It is unusual to observe systematic drift in the more recent detectors received from Redlen. However, this problem was ubiquitous in an earlier batch. The overall centroid positions for six detectors from this batch are shown in Figure 9.8.

The second major category of drift over a short time scale is a change in the properties of individual pixels. It is fairly common to observe pixels with some degree of gain deficit, as discussed in section 9.5. This gain deficit would have no effect on the calibration process if it remained constant over time. However, these pixels are often observed to experience gain deficit intermittently, resulting in random gain shifts over time between two or more discrete values. This is illustrated for detector 4R143 in Figure 9.9, which compares the photopeak positions using only the initial 10% or final 10% of the calibration data. There is no clear pattern or structure of these jumps; they occur randomly on a pixel-by-pixel basis. Such behavior is not possible to correct in real time, thus, the performance of these pixels will degrade and at times they may not contribute to the overall photopeak.

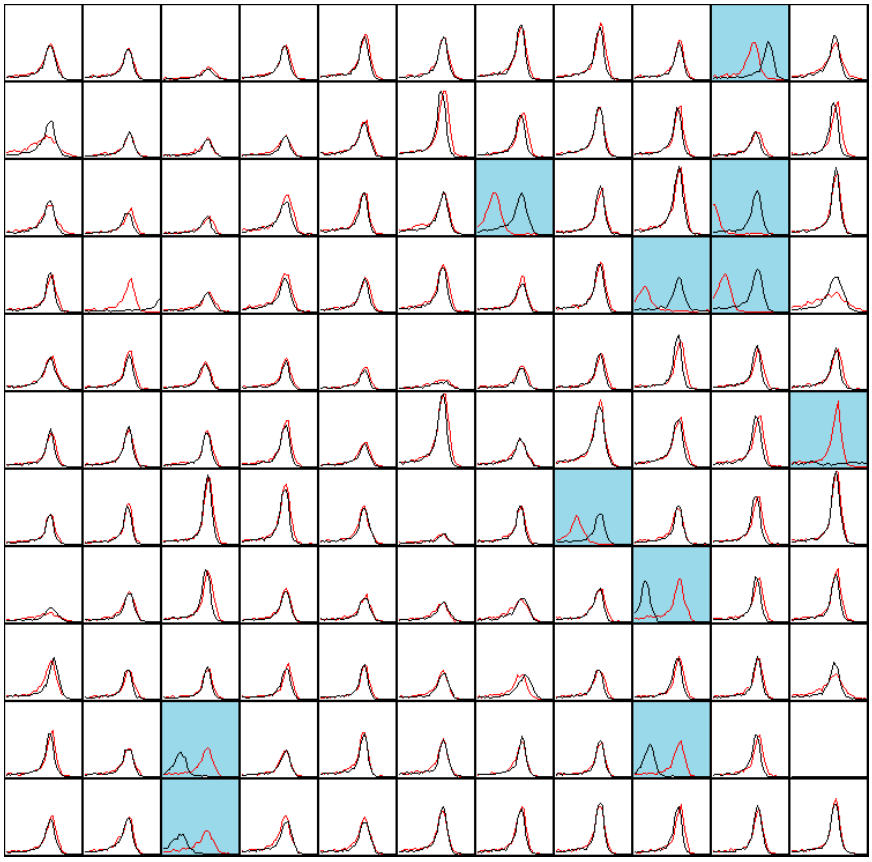

Figure 9.9: Evidence of gain variation. The red curves represent the initial two hours of data and the black curves represent the final two hours of data in a one day measurement. The photopeak region of a Cs-137 source is shown for each pixel.

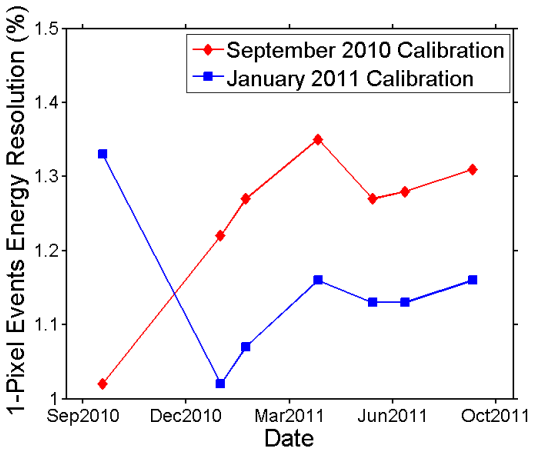

Figure 9.10: The photopeak position over time from single-pixel events in an 18 detector array. Measurements that occur close in time to the calibration measurement tend to yield the best results.

9.8 Long Term Calibration Stability

Understanding the long term stability of the calibration factors allows us to predict how often a CdZnTe system will need to be recalibrated. Such data was not available for a large number of crystals as it was atypical for us to keep a detector system assembled for more than a month. However, the first eighteen detector array of CdZnTe has been preserved in its original configuration for more than a year, for the purpose of studying the long term stability of the device.

The overall energy resolution of the device is shown over time in Figure 9.10 for one pixel events. The system was calibrated twice: once in September of 2010 and again in January of 2011. The energy resolution does not change between the September 2010 data and the January 2011 data if the appropriate calibration is used. This means the initial performance of the device can be reproduced four months later by recalibration. In other words, the performance does not degrade irreversibly over time. However, the energy resolution does steadily degrade over time when a single set of calibration factors is used. Both the 1-pixel and the all-events-combined energy resolutions increased by 0.3% in one year.

This study of long term stability helps bound the expected degradation of the calibration factors over time. If the best possible energy resolution is required then the system should be calibrated immediately before the experiment. Otherwise, the system can operate for at least a year and still achieve better than 1.5% energy resolution at 662 keV for single pixel events. If this device was turned into a commercial product than yearly device servicing would be recommended.

9.9 Conclusions

This chapter has shown experimental evidence of several possible complications that arise during the practical operation of an array of CdZnTe detectors. For the most part, these issues can be overcome by calibration or by rejecting the relatively small fraction of detectors that experience these problems. Bringing these issues to the attention of the crystal manufacturer allows them to improve their processes over time and ultimately results in a higher yield of excellent detectors.

The capability of the 3D position sensitive readout system is demonstrated throughout this chapter. The readout systems used allow us to measure the signal amplitude and instantaneous drift velocity in each voxel of a detector with a single measurement that takes about five hours to complete. This is a useful diagnostic tool that has enabled Redlen Technologies and the University of Michigan to collaborate on rapidly improving the quality of CdZnTe detector systems.

CHAPTER X

Conclusions

This dissertation has addressed a broad range of topics related to the operation of an array of 3D position sensitive pixelated semiconductor gamma-ray detectors. The detector configuration, readout electronics, event reconstruction algorithms, multiple pixel event performance, depth reconstruction, and complications due to readout electronics have all been discussed in detail. Significant progress was demonstrated during the course of this work, nevertheless, many limitations are yet to be overcome and these will provide challenges for future generations of students.

Optimizing and understanding the performance of multiple pixel events will continue to represent a major challenge. This work takes a significant step forward with the GMI ASIC system thanks to the peak hold circuit correction algorithms described in Chapter VII, which substantially improves the performance of events involving three or more pixels, as well as a better understanding of how the depth should be reconstructed in the case of side neighbor interactions. Furthermore, the analysis in Chapter IV provides a more complete description of the factors that degrade multiple pixel event resolution than prior work had achieved. The observation of pixel-by-pixel variation in the efficacy of the steering grid as well as the evidence that the nonlinearity, WPCT, and depth uncertainty are relatively small factors all represent important progress. However, the uncertainty in the degree of noise cor-

relation between pixels has made it challenging to prove that the theoretical limit of multiple pixel event resolution has been reached. This is an important goal for future work; to date the best we can provide is an upper bound on the noise correlation based on the results from the best detectors. An independent measurement that could provide a more accurate bound on the noise correlation would let us know how close we are to the theoretical performance limit.

The fact that pixelated CdZnTe can achieve 3D position sensitivity was known long before this dissertation. However, the collimation experiments described in chapters V and VI provide critical new information about the system. The uncertainty in the depth reconstruction is measured at multiple depths for a variety of detectors. This allows us to put a bound on the energy resolution degradation due to the depth reconstruction, for both single and multiple pixel events. Furthermore, studying the accuracy of the depth reconstruction for multiple pixel events lead to the discovery of WPCT in the timing domain as well as techniques to overcome this complication. Another key component of these experiments is the use of a precise positioning system for the collimator. A technique is developed to find the true anode and cathode position of a detector relative to the location of the collimator beam. With this information the relationship between the measured depth of interaction and true depth of interaction can be evaluated experimentally. The depth reconstruction is shown to be accurate within 1mm of the true depth throughout most of a 15mm thick CdZnTe. While the depth uncertainty is key for spectroscopy, both the uncertainty and accuracy must be considered in the formation of a Compton image.

Finally, this dissertation is written at a time when there is easy access to a large number of detectors and readout ASICs, often configured in detector arrays. This resulted in significant advances in the understanding of problems related to both detector crystals and ASICs. By examining a large number of samples many potential detector problems will be observed, such as gain deficit, gain variation, non-uniform

electric field, temperature sensitivity, and inadequate grid steering. However, some issues prove to be ubiquitous, such as the shape of the nonlinearity correction curve or the degradation in energy resolution for events that involve three or more pixels. These observations raised suspicion of ASIC problems and lead to experiments that demonstrate the impact of the electronics on the non-linearity as well as the impact of the peak-hold circuit on multiple pixel events.

It is the author's hope that the analysis and experimental observations presented in this thesis will add to the foundation of knowledge that future scientists will build on. The readout process is undergoing a major overhaul: moving from sampling an amplitude and time for each pixel to reading out the entire pre-amplifier waveform. Although this work is based on the traditional readout approach, many of the same problems will be encountered with the new systems. Hopefully this work will provide some guidance on experimental techniques to demonstrate problems with electronics, detectors, or reconstruction algorithms as well as the means to overcome them.

BIBLIOGRAPHY

BIBLIOGRAPHY

[1] W. R. Willig, "Mercury iodide as a gamma spectrometer," *Nucl. Instr. and Meth. A*, vol. 96, pp. 615–616, 1971.

[2] W. Akutagawa, K. Zanio, and J. W. Mayer, "CdTe as a gamma detector," *Nucl. Instr. and Meth. A*, vol. 55, pp. 383–385, 1967.

[3] J. E. Eberhardt, R. D. Ryan, and A. J. Tavendale, "High-resolution nuclear radiation detectors from epitaxial n-GaAs," *Applied Physics Letters*, vol. 17, no. 10, pp. 427–429, 1970.

[4] J. F. Butler, C. L. Lingren, and F. P. Doty, "$Cd_{1-x}Zn_xTe$ gamma ray detectors," *IEEE Trans. Nucl. Sci.*, vol. 39, no. 4, pp. 605–609, 1992.

[5] I. ur Rahman and R. Hofstadter, "Thallium halide radiation detectors," *Physical Review B*, vol. 29, no. 6, pp. 3500–3507, 1984.

[6] H. H. Barrett, J. D. Eskin, and H. B. Barber, "Charge transport in arrays of semiconductor gamma-ray detectors," *Phys. Rev. Lett.*, vol. 75, no. 1, pp. 156–159, 1995.

[7] P. Luke, "Unipolar charge sensing with coplanar electrodes-application to semiconductor detectors," *Nuclear Science, IEEE Transactions on*, vol. 42, no. 4, pp. 207 –213, aug 1995.

[8] D. S. McGregor, R. A. Rojeski, Z. He, D. K. Wehe, M. Driver, and M. Blakely, "Geometrically weighted semiconductor Frisch grid radiation spectrometers," *Nucl. Instr. and Meth. A*, vol. 422, pp. 164–168, 1999.

[9] Z. He, W. Li, G. F. Knoll, D. K. Wehe, J. E. Berry, and C. M. Stahle, "3-D position sensitive cdznte gamma-ray spectrometers," *Nucl. Instr. and Meth. A*, vol. 422, pp. 173–178, 1999.

[10] T. E. Schlesinger, J. E. Toney, H. Yoon, E. Y. Lee, B. A. Brunett, and L. Franks, "Cadmium zinc telluride and its use as a nuclear radiation detector material," *Materials Science and Engineering*, vol. 32, pp. 103–189, 2001.

[11] S. A. Awadalla, H. Chen, J. Mackenzie, P. Lu, K. Iniewski, P. Marthandam, R. Redden, G. Bindley, Z. He, F. Zhang, M. Groza, A. Burger, D. R. Mayo, and C. L. Sullivan, "Thickness scalability of large volume cadmium zinc telluride

high resolution radiation detectors," in *Nuclear Science Symposium Conference Record, 2008. NSS '08. IEEE*, oct. 2008, pp. 58 –62.

[12] Y. Zhu, S. E. Anderson, and Z. He, "Sub-pixel position sensing for pixelated, 3-d position sensitive, wide band-gap, semiconductor, gamma-ray detectors," *IEEE Trans. Nucl. Sci.*, vol. 58, pp. 1400–1409, 2011.

[13] H. Yang, J. C. Kim, and Z. He, "Event classification and reconstruction of single pixel multiple interaction events," in *Nuclear Science Symposium Conference Record (NSS/MIC/RTSD), 2011 IEEE*, 2011.

[14] Y. Zhu, "Digital signal processing methods for pixelated 3-D position sensitive room-temperature semiconductor detectors," Ph.D. dissertation, University of Michigan, 2012.

[15] G. F. Knoll, *Radiation Detection and Measurement*, 4th ed. John Wiley & Sons, Inc., 2010.

[16] S. M. Sze and K. K. Ng, *Physics of Semiconductor Devices*, 3rd ed. Wiley-Interscience, 2006.

[17] T. E. Schlesinger and R. B. James, Eds., *Semiconductors for Room Temperature Nuclear Detector Applications*. Academic Press, 1995.

[18] F. Zhang, "Events reconstruction in 3-D position sensitive CdZnTe gamma-ray spectrometers," Ph.D. dissertation, University of Michigan, 2005.

[19] M. Amman, J. Lee, P. Luke, H. Chen, S. Awadalla, R. Redden, and G. Bindley, "Evaluation of THM-grown CdZnTe material for large-volume gamma-ray detector applications," *Nuclear Science, IEEE Transactions on*, vol. 56, no. 3, pp. 795 –799, june 2009.

[20] Z. He, "Review of the shockley-ramo theorem and its application in semiconductor gamma-ray detectors," *Nuclear Instruments and Methods in Physics Research Section A: Accelerators,Spectrometers,Detectors and Associated Equipment*, vol. 463, no. 1-2, pp. 250 – 267, 2001. [Online]. Available: http://www.sciencedirect.com/science/article/pii/S0168900201002236

[21] C. E. Lehner, "4-pi compton imaging using a single 3-D position-sensitive CdZnTe detector," Ph.D. dissertation, University of Michigan, 2004.

[22] T. Takahashi, K. Nakazawa, T. Kamae, H. Tajima, Y. Fukazawa, M. Nomachi, and M. Kokubun, "High resolution cdte detectors for the next-generation multi-compton gamma-ray telescope," J. E. Truemper and H. D. Tananbaum, Eds., vol. 4851, no. 1. SPIE, 2003, pp. 1228–1235. [Online]. Available: http://link.aip.org/link/?PSI/4851/1228/1

[23] S. J. Kaye, W. R. Kaye, and Z. He, "4π coded aperture imaging using 3d position sensitive CdZnTe detectors," in *Nuclear Science Symposium Conference Record (NSS/MIC), 2008 IEEE*, 2008.

[24] D. McGregor, J. Lindsay, and R. Olsen, "Thermal neutron detection with cadmium$_{1-x}$ zinc$_x$ telluride semiconductor detectors," *Nucl. Instr. and Meth. A*, vol. 381, pp. 498–501, 1996.

[25] A. Zoglauer, M. Galloway, M. Amman, S. Boggs, J. Lee, P. Luke, L. Mihailescu, K. Vetter, and C. Wunderer, "First results of the High Efficiency Multi-mode Imager (HEMI)," in *Nuclear Science Symposium Conference Record (NSS/MIC), 2009 IEEE*, 24 2009-nov. 1 2009, pp. 887 –891.

[26] W. Drozdowski, P. Dorenbos, A. Bos, J. de Haas, S. Kraft, E. Maddox, A. Owens, F. Quarati, C. Dathy, and V. Ouspenski, "Effect of proton dose, crystal size, and cerium concentration on scintillation yield and energy resolution of labr3 :ce," *Nuclear Science, IEEE Transactions on*, vol. 54, no. 3, pp. 736 –740, june 2007.

[27] N. Cherepy, S. A. Payne, R. Hawrami, A. Burger, L. Boatner, E. V. Loef, and K. Shah, "Prospects for high energy resolution gamma ray spectroscopy with Europium-doped Strontium Iodide," in *MRS Proceedings*, 2009.

[28] M. Amman and P. N. Luke, "Three-dimensional position sensing and field shaping in orthogonal-strip germanium gamma-ray detectors," *Nuclear Instruments and Methods in Physics Research Section A: Accelerators, Spectrometers, Detectors and Associated Equipment*, vol. 452, no. 1-2, pp. 155 – 166, 2000. [Online]. Available: http://www.sciencedirect.com/science/article/pii/S016890020000351X

[29] J. Macri, B. Apotovsky, J. Butler, M. Cherry, B. Dann, A. Drake, F. Doty, T. Guzik, K. Larson, M. Mayer, M. McConnell, and J. Ryan, "Development of an orthogonal-stripe CdZnTe gamma radiation imaging spectrometer," *Nuclear Science, IEEE Transactions on*, vol. 43, no. 3, pp. 1458 –1462, jun 1996.

[30] D. McGregor and R. Rojeski, "Performance of CdZnTe geometrically weighted semiconductor frisch grid radiation detectors," *Nuclear Science, IEEE Transactions on*, vol. 46, no. 3, pp. 250 –259, jun 1999.

[31] G. Montemont, M. Arques, L. Verger, and J. Rustique, "A capacitive frisch grid structure for CdZnTe detectors," *Nuclear Science, IEEE Transactions on*, vol. 48, no. 3, pp. 278 –281, jun 2001.

[32] C. E. Seifert, D. S. Barnett, and M. J. Myjak, "Prospects for thermal neutron detection and imaging with the GammaTracker handheld radioisotope identifier," vol. 7079, no. 1, p. 707907, 2008.

[33] F. Zhang, W. Kaye, and Z. He, "Performance of 3-D position sensitive CdZnTe detectors for gamma-ray energies above 1 MeV," in *Nuclear Science Symposium Conference Record (NSS/MIC), 2009 IEEE*, 24 2009-nov. 1 2009, pp. 2012 –2016.

[34] S. E. Anderson, "Event classification for 3-d position sensitive semiconductor detectors," Ph.D. dissertation, University of Michigan, 2011.

[35] P. N. Luke, M. Amman, J. S. Lee, and P. F. Manfredi, "Noise in CdZnTe detectors," *IEEE Trans. Nucl. Sci.*, vol. 48, no. 3, pp. 282–286, 2001.

[36] Z. He, "Theoretical calibration of multiple pixel events in pixelated semiconductor devices," 2008, private communication.

[37] B. D. Yanoff, Y. Du, W. V. Dixon, N. K. Rao, W. Li, B. Claus, T. Topka, B. Moore, and J. S. Gordon, "GE intelligent personal radiation locator system," vol. 7306, no. 1, p. 730616, 2009. [Online]. Available: http://dx.doi.org/doi/10.1117/12.820886

[38] F. Zhang and Z. He, "New readout electronics for 3-D position sensitive CdZnTe/HgI_2 detector arrays," *IEEE Trans. Nucl. Sci.*, vol. 53, pp. 3021–3027, Oct. 2006.

[39] F. Zhang, "Spectroscopic performance of BNL H3D ASIC," 2009, private communication.

[40] G. A. Carini, A. E. Bolotnikov, G. S. Camarda, G. W. Wright, R. B. James, and L. Li, "Effect of te precipitates on the performance of cdznte detectors," *Applied Physics Letters*, vol. 88, no. 14, pp. 143 515 –143 515–3, apr 2006.

[41] J. C. Kim, S. E. Anderson, W. R. Kaye, F. Zhang, Y. Zhu, S. J. Kaye, and Z. He, "Charge sharing in common-grid pixelated cdznte detectors," *Nucl. Instr. and Meth. A*, vol. 654, pp. 233–243, 2011.

[42] F. Zhang, "Peak hold circuit in the gmi asic," 2007, private communication.

[43] D. Donnelly, H. Baer, J. Reidy, and M. Weidenbeck, "The calibration of a Ge(Li) gamma-ray spectrometer for energy and relative intensity measurements*," *Nucl. Instr. and Meth. A*, vol. 57, pp. 219–226, 1967.

[44] F. Zhang, W. Kaye, and Z. He, "Performance of 3-D position sensitive CdZnTe detectors for gamma-ray energies above 1 MeV," in *Nuclear Science Symposium Conference Record (NSS/MIC), 2009 IEEE*, 2009, pp. 2012 –2016.

[45] F. Zhang, "Correction of the system linearity using the test pulse," 2009, private communication.

[46] J. Jaffe, D. Jordan, and A. Peurrung, "Energy nonlinearity in radiation detection materials: Causes and consequences," *Nuclear Instruments and Methods in Physics Research Section A: Accelerators, Spectrometers, Detectors and Associated Equipment*, vol. 570, no. 1, pp. 72 – 83, 2007. [Online]. Available: http://www.sciencedirect.com/science/article/B6TJM-4M5WPFG-4/2/ceb20f04070dc5d52a483ddb35374207

[47] P. Ugorowski, A. Kargar, and D. McGregor, "Pulse height linearity of CdZnTe," in *Nuclear Science Symposium Conference Record (NSS/MIC), 2009 IEEE*, 2009, pp. 2023 –2031.

[48] A. Castaldini, A. Cavallini, B. Fraboni, P. Fernandez, and J. Piquerasv, "Deep energy levels in CdTe and CdZnTe," *J. Appl. Phys*, vol. 83, no. 4, pp. 2121–2126, 1998.

[49] D. Hofmann, W. Stadler, P. Christmann, and B. Meyer, "Defects in CdTe and $Cd_{1-x}Zn_xTe$," *Nucl. Instr. and Meth. A*, vol. 380, pp. 117–120, 1996.

[50] E. Rzepka, A. Lusson, A. Riviere, A. Aoudia, Y. Marfaing, and R. Triboulet, "Defects study by photoluminescence and cathodoluminescence in vanadium doped CdZnTe," *Journal of Crystal Growth*, vol. 161, pp. 286–291, 1996.

[51] H. Chen, K. Chattopadhyay, K. T. Chen, A. Burger, M. A. George, J. C. Gregory, P. K. Nag, J. J. Weimer, and R. B. James, "Passivation of CdZnTe surfaces by oxidation in low energy atomic oxygen," *J. Vac. Sci. Technol. A*, vol. 17, no. 1, pp. 97–101, 1999.

[52] H. W. Yao, R. J. M. Anderson, and R. B. James, "Optical characterization of the internal electric field distribution under bias of cdznte radiation detectors," vol. 3115, no. 1. SPIE, 1997, pp. 62–68.

[53] P. Rudolph, A. Engel, I. Schentke, and A. Grochocki, "Distribution and genesis of inclusions in cdte and (Cd,Zn)Te single crystals grown by the bridgman method and by the travelling heater method," *Journal of Crystal Growth*, vol. 147, pp. 297–304, 1995.

[54] M. Amman, J. S. Lee, and P. N. Luke, "Electron trapping nonuniformity in high-pressure-bridgman-grown CdZnTe," *J. Appl. Phys*, vol. 92, no. 6, pp. 3198–3206, 2002.

[55] G. A. Carini, A. E. Bolotnikov, G. S. Camarda, G. W. Wright, and R. B. James, "Effect of Te precipitates on the performance of CdZnTe detectors," *Applied Physics Letters*, vol. 88, pp. 143 515–143 515–3, 2006.

[56] A. E. Bolotnikov, G. S. Camarda, Y. Cui, A. Hossain, G. Yang, H. W. Yao, and R. B. James, "Internal electric-field-lines distribution in CdZnTe detectors measured using X-Ray mapping," *IEEE Trans. Nucl. Sci.*, vol. 56, no. 3, pp. 791–794, 2009.

[57] J. C. Erickson, H. W. Yao, R. B. James, H. Hermon, and M. Greaves, "Time of flight experimental studies of cdznte radiation detectors," *Journal of Electronic Materials*, vol. 29, no. 6, pp. 699–703, 2000.